MONASH University

Binary Neutron Star Remnants: the most extreme matter in the Universe

PAUL EASTER
Bachelor of Science Advanced - Research (Honours)

A thesis submitted for the degree of *Doctor of Philosophy* at
Monash University in 2021
School of Physics and Astronomy

Advisors:
Assoc. Prof. Paul Lasky
Dr. Andrew Casey

This thesis must be used only under the normal conditions of "fair dealing" under the Copyright Act. It should not be copied or closely paraphrased in whole or in part without the written consent of the author. Proper written acknowledgement should be made for any assistance obtained from this thesis. I certify that I have made all reasonable efforts to secure copyright permissions for third-party content included in this thesis and have not knowingly added copyright content to my work without the owner's permission.

© Paul Easter

Publications

- G. Ashton, M. Hübner, P. D. Lasky, C. Talbot, K. Ackley, S. Biscoveanu, Q. Chu, A. Divakarla, P. J. Easter, B. Goncharov, *et al.*, "BILBY: a user-friendly Bayesian inference library for gravitational-wave astronomy," *The Astrophysical Journal Supplement*, vol. 241, p. 27, Apr. 2019
- P. J. Easter, P. D. Lasky, A. R. Casey, L. Rezzolla, and K. Takami, "Computing fast and reliable gravitational waveforms of binary neutron star merger remnants," *Physical Review D*, vol. 100, p. 043005, Aug. 2019
- P. J. Easter, S. Ghonge, P. D. Lasky, A. R. Casey, J. A. Clark, F. Hernandez Vivanco, and K. Chatziioannou, "Detection and parameter estimation of binary neutron star merger remnants," *Physical Review D*, vol. 102, p. 043011, Aug. 2020
- E. Cuoco, J. Powell, M. Cavaglià, K. Ackley, M. Bejger, C. Chatterjee, M. Coughlin, S. Coughlin, P. J. Easter, R. Essick, *et al.*, "Enhancing gravitational-wave science with machine learning," *Machine Learning: Science and Technology*, vol. 2, p. 011002, Dec. 2020
- P. J. Easter, P. D. Lasky, and A. R. Casey, "Can we measure the collapse time of a post-merger remnant for a future GW170817-like event?," *arXiv e-prints*, June 2021

Declaration of Authorship

I hereby declare that this thesis contains no material which has been accepted for the award of any other degree or diploma at any university or equivalent institution and that, to the best of my knowledge and belief, this thesis contains no material previously published or written by another person, except where due reference is made in the text of the thesis.

This thesis includes two original papers published in peer reviewed journals and one submitted publications. The core theme of this thesis is probing the physics of binary neutron star post-merger remnants with gravitational waves. The ideas, development and writing up of all the papers in the thesis were the principal responsibility of myself, the student, working within the School of Physics and Astronomy under the supervision of Assoc. Prof. Paul Lasky and Dr. Andrew Casey.

The inclusion of co-authors reflects the fact that the work came from active collaboration between researchers and acknowledges input into team-based research.

I have renumbered sections of submitted or published papers in order to generate a consistent presentation within the thesis.

In the case of Chapters 2, 3,and 4 my contribution to the work is shown on the following page.

Student name: Paul John Easter

Student signature: Date: 8 August 2021

I hereby certify that the above declaration correctly reflects the nature and extent of the student's and co-authors' contributions to this work. In instances where I am not the responsible author I have consulted with the responsible author to agree on the respective contributions of the authors.

Main Supervisor name: Paul D Lasky

Main Supervisor signature: Date: 8 August 2021

Thesis Chapter	Publication Title	Status	Student contribution	Co-author contribution	Monash student co-author
2	Computing Fast and Reliable Gravitational Waveforms of Binary Neutron Star Merger Remnants	Published (PRD)	75% Concept, method, code development, analysis, writing	P. Lasky/A. Casey 15%-Concept, method, analysis, writing L. Rezzolla/K. Takami 10% - analysis, writing	No
3	Detection and parameter estimation of binary neutron star merger remnants	Published (PRD)	70% Concept, method, code development, analysis, writing	S. Ghonge 10%-Concept, method, code development, analysis, writing F. Hernandez Vivanco 10% - Concept, method, code development, analysis, writing P. Lasky/A. Casey 5%-Concept, method, analysis, writing J. Clarke/K. Chatziioannou 5% - Concept, analysis, writing	Yes Hernandez Vivanco
4	Can we measure the collapse time of a post-merger remnant for a future GW170817-like event?	Submitted (PRD)	75% Concept, method, code development, analysis, writing	P. Lasky/A. Casey 25%-Concept, method, analysis, writing	No

Acknowledgements

The most important person for me to acknowledge is my wife. It was only with her forbearance and encouragement that I was able to return to University, obtain my Honours in Advanced Science (Research) and continue on towards my doctorate over a total of a seven year period. I would also like to thank my daughters who have all literally grown up during this period. I look forward to spending more time with you after this submission. And of course, I am pleased to acknowledge my supervisors, Paul and Andy, who in their infinite patience encouraged me on this journey, particularly when covid-19 tried to stop the world in its tracks. My peers in PhD room 125 both present and past, have made life interesting and fun over the last three years. I'm sure you are all heading towards brilliant futures. This research was supported by the Faculty of Science Dean's Postgraduate Research Scholarship without which I would not have had the opportunity to attempt this.

Contents

Publications ii

Declaration of Authorship iii

Acknowledgements v

Contents vi

Abstract 1

1 Introduction 2
- 1.1 Gravitational waves . . . 2
- 1.2 Neutron stars . . . 4
- 1.3 Neutron star mergers . . . 6
- 1.4 Numerical relativity simulations . . . 7
- 1.5 Post-merger remnants . . . 9
- 1.6 Gravitational-wave strain and spectra . . . 11
- 1.7 Post-merger gravitational-wave models . . . 14

2 Computing Fast and Reliable Gravitational Waveforms of Binary Neutron Star Merger Remnants 16
- 2.1 Introduction . . . 16
- 2.2 Methodology . . . 17
- 2.3 Results . . . 21
- 2.4 Discussion . . . 23

3 Detection and parameter estimation of binary neutron star merger remnants 25
- 3.1 Introduction . . . 25
- 3.2 Methodology . . . 27
- 3.3 Model Validation . . . 29
- 3.4 Sensitivity . . . 30
- 3.5 Parameter estimation . . . 33
- 3.6 Discussion . . . 36
- 3.A Numerical relativity simulations . . . 39
- 3.B Priors . . . 40
- 3.C Posteriors for all numerical-relativity injections . . . 40

4 Can we measure the collapse time of a post-merger remnant for a future GW170817-like event? 45
- 4.1 Introduction . . . 45
- 4.2 Methodology . . . 47

4.3 Results 50
4.4 Discussion 51
4.5 Acknowledgments 52
4.A Priors 53
4.B Example posteriors 54

5 Conclusion **55**

Bibliography **59**

Abstract

Surviving remnants from binary neutron star mergers, remnants that have not yet collapsed to a black hole, are some of the most extreme forms of matter known in the Universe. The densities of surviving merger remnants are $\sim 10^{14} - 10^{15}\,\mathrm{g\,cm^{-3}}$ which is up to several times nuclear density. The temperature of the post-merger remnant can reach values from tens to hundreds of MeV. This combination of extreme temperatures and densities result in a state of matter that is observable only in proto-neutron stars and post-merger remnants. Although binary neutron star post-merger remnants have yet to be directly observed, they are a target for gravitational-wave detection in the near future.

A surviving post-merger remnant could potentially be detected by applying a matched filter between an incoming gravitational-wave signal and the gravitational-wave strain generated from numerical-relativity simulations. However, these simulations are performed in full general relativity and are extremely expensive. This prohibits their direct use in the detection and parameter estimation of post-merger remnant properties. Other methods are required to generate post-merger gravitational waveforms that are computationally affordable.

Here we develop two methods that can generate gravitational waveforms of post-merger remnants. In the first method, we train a hierarchical model to find a relationship between the progenitor neutron star properties and gravitational-wave spectra produced by numerical-relativity simulations. After training, we generate gravitational-wave spectra in a fraction of a second and measure cross-validated fitting-factors with a mean of 0.95 where 1.0 is a perfect fit.

For the second method, we introduce an analytical model that can successfully capture the richness of post-merger gravitational waveforms generated by numerical-relativity simulations. We measure median fitting factors between the gravitational-wave strain produced by numerical-relativity simulations and our inferred waveforms as > 0.9. With this method, we can detect surviving post-merger remnants with signal-to-noise ratios of $\geqslant 7$. We find that, at signal-to-noise ratios of 15, the dominant post-merger oscillation frequency can be constrained to $\pm^{1.4}_{1.2}\%$, and the tidal coupling constant can be constrained to $\pm^{9}_{12}\%$.

We then measure when the post-merger remnant will collapse into a black hole. We show that we need a gravitational-wave detector network of Einstein Telescope with Cosmic explorer to measure a collapse time of $\sim 10\,\mathrm{ms}$ for a GW170817-like event at $\sim 40\,\mathrm{Mpc}$. These three methods introduce additional tools that allow for the detection and parameter estimation of post-merger remnants when gravitational-wave instruments achieve sufficient sensitivity.

Chapter 1

Introduction

1.1 Gravitational waves

In 2017, the LIGO and Virgo collaborations observed the first direct gravitational waves from a binary neutron star merger, GW170817 [6]. This began the era of multi-messenger gravitational-wave observations with coincident detections in many parts of the electromagnetic spectrum [7–14].

Gravitational waves are a phenomenon predicted by general relativity which was formulated more than 100 years ago by Albert Einstein with the famous formula

$$G_{\mu\nu} = R_{\mu\nu} - \frac{1}{2}Rg_{\mu\nu} = \frac{8\pi G}{c^4}T_{\mu\nu}, \tag{1.1}$$

where $G_{\mu\nu}$ is the space-time curvature tensor and $T_{\mu\nu}$ is the stress energy tensor. The local metric tensor is $g_{\mu\nu}$, $R_{\mu\nu}$ is the Ricci tensor and R is the Ricci scalar. The gravitational constant is G and the speed of light in vacuum is c, though for remainder of this work we will use geometric units of $G = c = 1$ unless otherwise stated. Equation 1.1 demonstrates how the curvature of the space-time, $G_{\mu\nu}$, alters the dynamics of matter, $T_{\mu\nu}$, and vice-versa.

Movement of matter in space can generate gravitational waves. For simulation purposes, the movement of matter can be modelled by the Einstein field equations Eq.(1.1) and perturbations of black holes [e.g., 15–18]. This methodology allows the calculation of multipole functions of odd ($\mathcal{Q}^{\times}_{lm}$) and even ($\mathcal{Q}^{+}_{lm}$) parity, with angular indices of (l, m). These multipoles can be evaluated by numerical-relativity simulations which allow the extraction of gravitational waves. The plus, h_+, and cross, $h_\times$, polarisations of the gravitational waves are related to the multipoles as follows [15–19]:[1]

$$h_+ - ih_\times = \frac{1}{r\sqrt{2}}\sum_{l,m} {}_{-2}Y^{lm}\left(\mathcal{Q}^{+}_{lm} - i\int_{-\infty}^{t}\mathcal{Q}^{\times}_{lm}(t')dt'\right). \tag{1.2}$$

Here, r is the distance to the gravitational-wave source and ${}_{-2}Y^{lm}$ are the spin-weighted spherical harmonics with spin $s = -2$ and angular indices of (l, m). For most sources, gravitational waves are predominantly emitted in the $l = m = 2$ mode. In this case Eq.(1.2) evaluates to

$$h_+ + ih_\times = \frac{1}{2r}\sqrt{\frac{5}{2\pi}}e^{2i\phi}\cos^4\left(\frac{\theta}{2}\right)\left(\mathcal{Q}^{+}_{22} - i\int_{-\infty}^{t}\mathcal{Q}^{\times}_{22}(t')dt'\right), \tag{1.3}$$

where θ is the polar angle and ϕ is the azimuthal angle usually defined relative to orbital angular momentum vector.

[1] Please note that $\mathcal{Q}^{+}_{lm}$ and $\mathcal{Q}^{\times}_{lm}$ have different units, see Ref. [18] for more information.

The energy loss due to gravitational waves can be calculated from Eq.(1.2) as [18]

$$\frac{dE}{dt} = \frac{1}{32\pi} \sum_{l,m} \left(\left| \frac{\mathrm{d}\mathcal{Q}^{+}_{lm}}{dt} \right|^2 + \left| \mathcal{Q}^{\times}_{lm} \right|^2 \right). \tag{1.4}$$

For binary systems, this results in an incremental reduction in the orbital separation which was famously measured in the Hulse-Taylor binary neutron star, B1913+16 [20–22].

If the separation between binary compact objects is small enough, then this loss of energy can lead to a merger. This was the case for the first direct detection of a binary black hole merger, GW150914, and first neutron star merger, GW170817 [6, 23]. The decrease in the orbital separation and increase in gravitational-wave amplitude, results in a characteristic 'chirp' signal for the inspiral of binary compact objects.

Assuming a circular orbit of two point masses of mass M_1 and M_2, the Newtonian quadrupole formula can be used to calculate the evolution of the orbital separation, a, due to gravitational wave emission: [e.g., 24]

$$\frac{da}{dt} = -\frac{64}{5} \frac{\mu M^2}{a^3}, \tag{1.5}$$

where $M \equiv M_1 + M_2$ is the total mass, and $\mu \equiv M_1 M_2 / M$ is the reduced mass. The time evolution of gravitational-wave strain frequency can then be calculated as

$$\frac{df}{dt} = \frac{96}{5} \pi^{8/3} \mathcal{M}^{5/3} f^{11/3}, \tag{1.6}$$

where $\mathcal{M} \equiv \mu^{3/5} M^{2/5}$ is the chirp mass of the binary system. Using Eqs.(1.5-1.6), an expression for the frequency and the gravitational-wave strain magnitude can be calculated [e.g., 24]:

$$f \propto \mathcal{M}^{-5/8} (t_c - t)^{-3/8}, \tag{1.7}$$

$$|h(t)| \propto \frac{\mathcal{M}^{5/4}}{D} (t_c - t)^{-1/4}, \tag{1.8}$$

where t is the time, t_c is the time until coalescence, and D is the luminosity distance to the source. The combination of Eq.(1.7) and Eq.(1.8) result in the chirp waveform detected in the inspiral of compact object mergers.

The first direct gravitational-wave detection from the inspiral of a binary neutron star merger, GW170817, was observed by a detector network consisting of the LIGO detectors at Hanford, Washington and Livingston, Louisiana in the USA, and the Virgo detector in Cascina, Italy [6, 25, 26]. All three detectors consist of 'L' shaped laser interferometers with free-falling test-masses. The gravitational-wave strain is found by measuring the optical path difference between the perpendicular beam tubes.

Another binary neutron star (possibly neutron star - black hole) merger, GW190425, was detected in 2019 [27–29]. However, the luminosity distance of GW190425, 159^{+69}_{-72} Mpc, and the broad sky localisation of the source, $8284\,\mathrm{deg}^2$, precluded any coincident electromagnetic observations [27]. In comparison, the sky localisation of GW170817 was $28\,\mathrm{deg}^2$ at a distance of ~ 40 Mpc. Therefore,

to date, GW170817 is the only gravitational-wave signal that was observed with coincident electromagnetic radiation and will be discussed further in Section 1.3.

Although the LIGO and Virgo collaborations were able to detect part of the inspiral for GW170817, the sensitivity of the existing network was not sufficient to detect the gravitational-wave strain from either the late inspiral or the post-merger remnant. This is because the gravitational-wave strain emitted from these phases are at high frequencies, where the existing networks lack sensitivity. Figure 1.1 shows the amplitude spectral sensitivity at design sensitivity for LIGO Hanford in blue and Virgo in dashed orange. Funding has been secured to upgrade the LIGO network to A+ sensitivity, which will result in an improvement of $\sim 2-3$ [30, 31] and is shown with the green dotted curve.

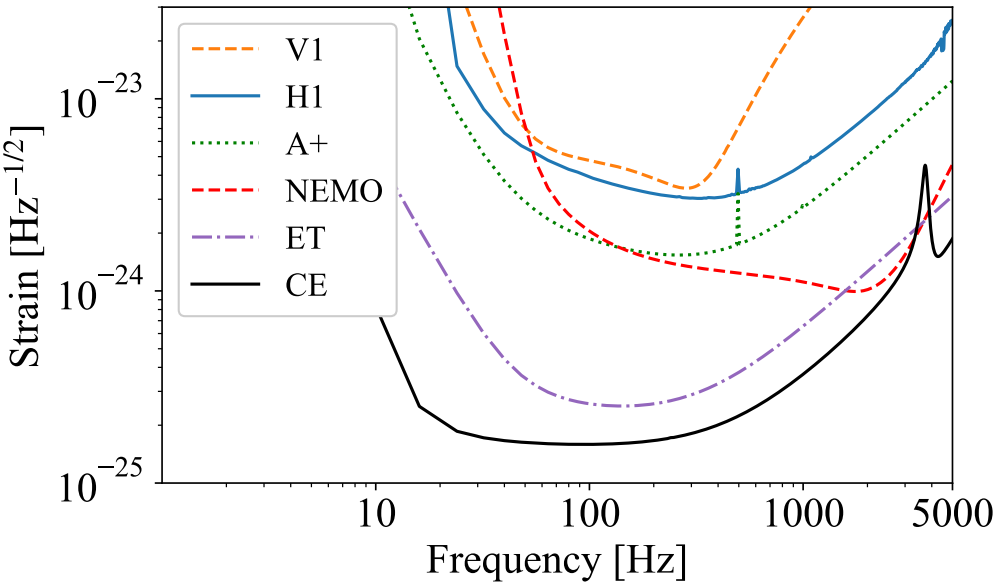

Figure 1.1: Amplitude spectral sensitivity curves in $\mathrm{Hz}^{-1/2}$ for Virgo (orange, dashed) and Hanford (blue) at advanced design sensitivity, A+ (green, dotted), NEMO (red, dashed), Einstein Telescope (purple, dash-dotted) and Cosmic Explorer (black). The NEMO detector is ~ 5 times more sensitive than A+ at $\sim 2\,\mathrm{kHz}$ frequency.

A high-frequency detector has been proposed that will focus specifically on gravitational waves from the late inspiral and the post-merger remnant [31]. This detector will be known as the Neutron star Extreme Matter Observatory (NEMO) and will serve two major goals. The first, as mentioned above, is gravitational-wave measurements of post-merger remnants and late time mergers. The second goal is to develop technology that will allow the third-generation observatories, Cosmic Explorer and Einstein Telescope, to be built [32, 33]. Figure 1.1 also shows the amplitude spectral density for NEMO (red, dashed), Einstein Telescope (Purple, dash-dot), and Cosmic Explorer (black). NEMO is ~ 5 times more sensitive than A+ at a frequency of $\sim 2\,\mathrm{kHz}$, resulting in a $\sim 10-15$ times improvement when compared to Advanced LIGO.

1.2 Neutron stars

Neutron stars are compact stellar remnants that are formed following supernovae of stars with masses of $\gtrsim 8\,\mathrm{M}_\odot$ [e.g., 34]. They can also be formed from the dynamics of binary star systems [e.g., 35–37]. Neutron stars are created when the gravitational collapse of the inner stellar core overcomes the electron

degeneracy pressure. The proto-neutron star matter is then supported against further collapse by neutron (or quark) degeneracy pressure.

Proto-neutron stars cool below the Fermi energy at nuclear density, $\mathcal{E}_F \sim 50\,\mathrm{MeV}$, in the timescale of seconds [e.g., 38–41]. Such relatively low temperatures allow regions of superconductivity and superfluidity to form within the neutron star interior. Neutron stars are extremely dense objects with a central density $\sim$ 5-10 times nuclear density with magnetic fields of $\sim 10^8$-10^{15} G [e.g., 34, 42, 43]. They consist of the most dense bulk matter in the Universe.

General-relativistic corrections to Newtonian physics are necessary to determine the relationship between the neutron star mass and radius. For non-rotating stars, this relationship calculated by [44, 45]

$$\frac{dm}{dr} = 4\pi\rho r^2, \tag{1.9}$$

$$\frac{dp}{dr} = -\frac{p+\rho}{r(r-2m)}\left(4\pi p r^3 + m\right), \tag{1.10}$$

where r is the radial distance, m is the mass enclosed up to r, p is the pressure at r, and ρ is the density at r. Equations 1.9-1.10, in combination with the equation of state, allow the the mass and radius of neutron stars to be calculated, as well as the maximum non-rotating neutron star mass, M_{TOV}, for the given equation of state.

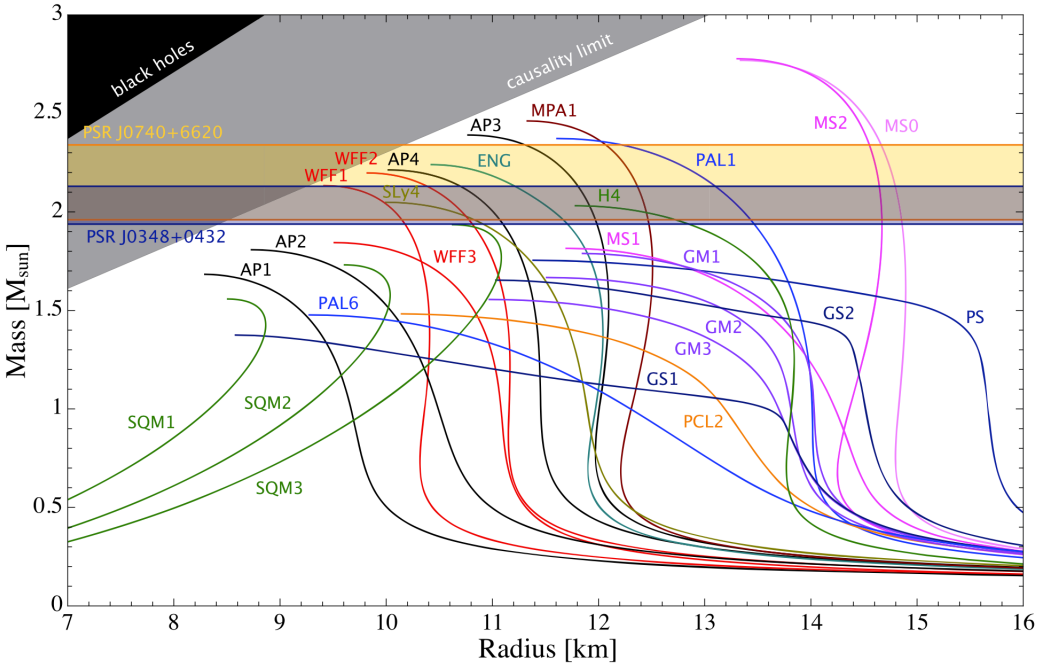

Figure 1.2: Mass-radius diagram for several different equations of state (Figure from Ref. [46]). The horizontal axis shows the radius in km and the vertical axis shows the neutron star mass in $M_\odot$. The two most massive known neutron stars, J0348+0432 [47] and J0740+6620 [48], are shown as horizontal shaded regions.

Figure 1.2 shows the mass-radius relationship for different prospective neutron star equations of state [46]. The M_{TOV} for a given equation of state is indicated by the mass value corresponding to the upper-most end of the mass-radius curve. Any additional mass accumulated beyond M_{TOV} introduces a radial instability that leads to the collapse of the neutron star into a black hole. The heaviest neutron star discovered to date is J0740+6620 with mass of

$2.14^{+0.10}_{-0.09}\,\mathrm{M}_\odot$ (Fig. 1.2, pale yellow region) [48]. Any equation of state that does not enter this region can be eliminated as non-physical.

An equation of state can further classified by its dimensionless compactness, $C \equiv GM/Rc^2$, where M and R are the neutron star mass and radius, respectively. Large values of C, corresponding to soft equations of state, are shown with curves towards the left of Fig. 1.2, whereas stiffer equations of state, with smaller C, are located towards the right of Fig. 1.2. The black region in Fig. 1.2, where $C \geqslant 0.5$, is excluded to neutron stars as the Schwarzschild radius is larger than the prospective neutron star radius.[2] The grey region is excluded by causality, where the speed of sound in the neutron star exceeds c. Given these constraints, the radius of neutron stars are $\gtrsim 10\,\mathrm{km}$ with $\mathrm{M_{TOV}} \gtrsim 2.2\,\mathrm{M}_\odot$.

1.3 Neutron star mergers

Binary neutron star mergers emit vast amounts of energy in gravitational waves. The estimated radiated energy for the GW170817 merger was $\gtrsim 5\times10^{52}$ ergs [6], equivalent to $\sim 1\%$ of the total rest mass of the two neutron stars. For a source at a distance of D from the observer, the amplitude of gravitational waves are $\propto 1/D$, whereas the amplitude of electromagnetic waves are $\propto 1/D^2$. Additionally, electromagnetic waves can be attenuated by intervening media between the source and the detector whereas gravitational waves are transparent to the intervening media. Hence gravitational waves are detectable over much larger distances in comparison to electromagnetic radiation with the same source luminosity.

Gravitational-wave strain emitted from the inspiral of binary neutron star mergers, approximated by Eqs.(1.6-1.8), can be recast in the frequency domain using the stationary phase approximation [24]

$$h_{22}(f) \equiv \frac{\mathcal{A}}{D}\mathcal{M}^{5/6} f^{-7/6} \exp(i\Psi(f)), \tag{1.11}$$

$$\Psi(f) = 2\pi f t_c - \phi_c - \frac{\pi}{4} + \frac{3}{4}\left(8\pi\mathcal{M}f\right)^{-5/3}, \tag{1.12}$$

where $h_{22}(f)$ is the Fourier transform of the $(l,m) = (2,2)$ gravitational-wave strain, and $\Psi(f)$ is the corresponding phase. Here, f is the frequency (Eq.(1.6)), ϕ_c and t_c are the phase and time of coalescence, and $\mathcal{A}$ is a factor that depends on the orientation of the system.[3] Equations (1.11)-(1.12) are valid until close to the merger time. The orbital separation, a, at the merger time can be approximated by the innermost stable circular orbit, where $a \sim 6M$. Therefore Eqns.(1.11)-(1.12) are valid for $a \gtrsim 6M$ [24]. Solving Eqs.(1.5-1.6) for $a \sim 6M$ gives $f_{max} \approx c^3(6^{3/2}\pi GM)^{-1}\,\mathrm{Hz}$.

The validity for these equations can be extended to times closer to the merger by adding relativistic corrections calculated by post-Newtonian expansion and effective-one-body dynamics [24, 49–54]. These corrections introduce

[2] The Schwarzschild radius, $Rs = 2GM/c^2$, for a non-rotating black hole corresponds to $C = 0.5$ which corresponds to a gradient on the Mass-radius diagram of $c^2/2G \approx 0.339\mathrm{M}_\odot/\mathrm{km}$.

[3] The orientation factor, $\mathcal{A}$, depends on angles intrinsic and extrinsic to the binary system. Intrinsic angles include the angles defining the relative orientation of the neutron star spins to the orbital plane. Extrinsic angles include the angles defining the relative orientation between the orbital plane and each of the detectors.

dependence on the masses, spins, and tidal deformabilities of the individual neutron stars. This allows the measurement of these system properties in addition to the chirp mass, given a gravitational-wave inspiral detection. However, the accuracy of the individual neutron star properties is significantly less than the accuracy of the chirp mass because the relativistic corrections required to measure these properties are fairly weak. This can be seen by looking at the parameters measured from GW170817.

The best measured quantities of GW170817 are the chirp mass, $\mathcal{M} = 1.186 \pm 0.001\,\mathrm{M}_\odot$, and the total mass, $M = 2.73^{+0.04}_{-0.01}\,\mathrm{M}_\odot$ [55]. The measurements that rely more on relativistic corrections are less constrained: the component masses are $M_1 = 1.48 \pm 0.12\,\mathrm{M}_\odot$ and $M_2 = 1.26 \pm 0.10\,\mathrm{M}_\odot$, at 90% credible intervals [55].[4] The mass-weighted quadrupolar tidal deformability was measured as $\tilde{\Lambda} = 300^{+420}_{-230}$ at 90% credible interval [55].

A coincident short gamma-ray burst was detected 1.7 s after the inferred merger time for the GW170817 gravitational-wave event [6, 7]. A subsequent search found an optical candidate, SSS17a/AT2017gfo, near galaxy NGC 4993 at a distance of $\simeq 40\,\mathrm{Mpc}$, within 11 hours of the merger [8]. Other searches made detections from radio to X-rays [e.g., 9–13]. The first detectable X-rays were found with the Chandra X-ray Observatory nine days after the merger, which was consistent with an off-axis short gamma-ray burst [9].

The two favoured scenarios for the launch of GRB 170817A involve a central engine of a black hole with an accretion torus [e.g., 56–58], or a central engine of a highly magnetised post-merger neutron star [e.g., 59]. Early lanthanide-poor kilonova observations from AT2017gfo suggest that the short gamma-ray burst was launched following the collapse of the post-merger remnant at $\sim 0.1 - 1\,\mathrm{s}$ after the merger [56]. Modelling the mass of the kilnova ejecta suggests that the post-merger remnant collapsed at $\sim 1\,\mathrm{s}$ [57]. Jet structure together with afterglow observations were used to conclude that the post-merger remnant collapsed at $\sim 1 - 1.7\,\mathrm{s}$ [58]. However, a stable neutron star remnant was found to be consistent with modelling of the AT2017gfo kilonova if the kilonova was powered mostly by radioactivity early on with additional energy from the neutron star remnant after $\sim 3\,\mathrm{days}$ [59].

Using gravitational waves to measure if and when the post-merger remnant of GW170817 collapsed to a black hole would greatly aid the modelling of GRB 170817A/AT2017gfo. Unfortunately, existing gravitational-wave detectors are not sensitive enough in the kHz range (see Fig. 1.1 and Sec. 1.6) and the collapse time is one of the most difficult parameters to predict with numerical-relativity simulations.

1.4 Numerical relativity simulations

Numerical-relativity simulations are required for determining the dynamics of the late inspiral of the binary neutron star and the post-merger remnant. To perform a numerical-relativity simulation, the equation of state must be defined, a set of initial conditions must be evaluated in general relativity, and then Einstein's field equations must be evolved. Each of these three requirements

[4] These posteriors assume low-spin priors that are expected from Galactic neutron star binaries. Posteriors were also taken assuming more agnostic spin priors, see Ref. [55] for further details.

make these simulations difficult. The equation of state for cold neutron stars is still unknown, and the equation of state for hot post-merger remnants is even more uncertain, after all, this is the hottest and densest bulk matter in the Universe.

The initial conditions for binary neutron star mergers in general relativity are complex and a number of methods have been developed for this task. Codes that have been used for this include `LORENE` [60] and `COCAL` [61]. The `LORENE` code used multi-domain spectral-methods to solve for the initial conditions of neutron star binaries assuming a conformally-flat approximation [60]. This was achieved by constructing quasiequilibrium configurations, which are approximations of the inspiral dynamics using exactly circular orbits. The `COCAL` code has also been used to generate quasiequilibrium initial conditions for binary neutron stars mergers. Here, the field equations are expressed in elliptic form and are solved by multipole expansion of Green's integral formula [61, 62]. Once the initial conditions have been approximated then the space-time can be evolved.

Space-time evolution methods include the following formulations: Arnowitt-Deser-Misner (ADM) [63][5], Baumgarte-Shapiro-Shibata-Nakamura-Oohara-Kojima (BSSNOK) [64–67] and Z4c [68–72]. The ADM formalism is a Hamiltonian method that splits the Einstein's field equations into separate time and space components. This is achieved by applying a gauge that consists of a shift vector and lapse function [63]. Unfortunately, as ADM numerical simulations are weakly hyperbolic in some guages, errors were found to accumulate over the simulation time [73–75]. To counter this, a number of different formulations were devised to improve this.

To aid computation convergence, the BSSNOK method extended the ADM formalism by introducing a conformal factor to the three-metric and selecting a dissipative hyperbolic driver for the shift vector [64–67, 76–78]. The Z4c formalism modified the BSSNOK method by adding a four-vector of constraints, Z_μ, to the Einstein field equations [68–72]. This resulted in a propagating Hamiltonian constraint which helps to reduce constraint-violation growth by damping all constraint violations except for constant modes [70]. The introduction of Z_μ, given an approapriate gauge, enforces hyperbolic solutions of the Einstein field equations by placing additional constraints on the system, thereby improving convergence [71, 72, 79].

General-relativisitic hydrodynamic methods include codes such as `Whisky` [80], `WhiskyTHC` [80–83], and `BAM` [84–89]. `WhiskyMHD` is a magneto-hydrodynamic extension to `Whisky` [90–92], allowing for the introduction of magnetic fields. In this work we use gravitational-wave signals extracted from general-relativisitic hydrodynamic simulations from Refs. [93–100]. Refs. [93, 96] use the `BAM` evolution code with the Z4c formulation, Refs. [95, 97–99] use the `WhiskyTHC` evolution code with the Z4c formulation, and Ref. [94] uses the `Whisky` evolution code with the BSSNOK formulation.

The aforementioned tools allow the simulation of the late-time merger and post-merger remnant. However, there are a number of caveats that need to be considered. Firstly, the simulations are expensive, for example, 32 binary neutron star simulations took $\sim 3 \times 10^6$ CPU hrs to complete [101]. Because of this, the direct use of numerical-relativity simulations in detection and parameter estimation, where we need large quantities of waveforms, is unfeasible.

[5]The original book reference for ADM formalism is out of print and the authors have listed the cited paper as an 'intentially unretouched' alternative.

Secondly, numerical-relativity simulations unavoidably include numerical viscosity. Early simulations show that numerical viscosity could alter the properties of both the neutron star core and the surface [102–105]. Numerical viscosity was found to introduce phase errors in the late-stage merger and improvements in numerical methods were subsequently introduced to minimise these errors [81]. The effects of numerical viscosity on the post-merger remnant is less clear, though it was found that numerical viscosity could alter both the neutrino luminosity [106] and the presence of one-armed spiral instability [95].

Thirdly, because of the complexity of the full general-relativity simulations, it is difficult to include all the necessary physics into simulations. Most simulations are performed with general-relativistic hydrodynamics, some also incorporate neutrino effects [e.g., 107–111], viscous effects [e.g., 97, 112–114], and magnetic fields [e.g., 91, 92, 115–121].

Finally, simulations of the remnant are dependent on the spatial resolution. Generally, increasing the spatial resolution leads to more accurate simulations at the cost of simulation time. Ref. [100] state that their post-merger simulations from the `CoRe` database are accurate enough to infer the energy and frequency content of the post-merger remnant. Additionally, a recent examination of waveform systematics found that existing waveform models, including numerical-relativity simulations, were not accurate enough to inform the equation of state at very loud SNRs ($\gtrsim 100$) expected from third-generation detectors [122]. These are important points: the uncertainty in the phase evolution and collapse time of the post-merger remnant, which is discussed further in Sec. 1.6, has had a significant impact on the design of the models developed in this thesis.

1.5 Post-merger remnants

Neutron star mergers can result in four outcomes, depending on the total mass of the post-merger remnant and the maximum non-rotating neutron star mass, $\mathrm{M_{TOV}}$. The four different merger remnants in descending mass order are: black holes, hypermassive neutron stars, supramassive neutron stars, and stable neutron stars. With a total mass of $\gtrsim 1.5\,\mathrm{M_{TOV}}$, a black hole is promptly formed [123]. A hypermassive neutron star is formed when the mass is between approximately $1.2\,\mathrm{M_{TOV}}$ and $1.5\mathrm{M_{TOV}}$ [123, 124]. A supramassive neutron star is formed if the mass is between $1.0\,\mathrm{M_{TOV}}$ and $1.2\mathrm{M_{TOV}}$, and a stable neutron star is formed when the total mass is $\leq 1.0\,\mathrm{M_{TOV}}$. A remnant that has not collapsed into a black hole is referred to as a surviving remnant.

Newly-formed post-merger remnants are differentially rotating unless they promptly collapse to a black hole within $\sim 2\,\mathrm{ms}$. The differential rotation is quenched by gravitational-wave emission, magnetic braking, viscous forces, and neutrino cooling. If the remnant is a hypermassive neutron star then it will collapse into a black hole when the differential rotation is reduced below a critical value [123] and thermal support is lost [e.g., 125, 126].

If the differentially-rotating remnant is a supramassive, or stable neutron star, then the remnant will evolve into a rigidly-rotating neutron star. A supramassive neutron star is supported against collapse by rigid rotation and will not collapse until the angular momentum drops below a critical value [124]. If the remnant has a mass corresponding to a stable neutron star, then it will remain stable for all levels of rigid rotation.

Given a post-merger remnant mass, the deciding factor that discriminates between supramassive neutron stars and hypermassive neutron stars is M_{TOV}. References [127–129] found upper limits on M_{TOV} of $\lesssim 2.2\,M_\odot$ using numerical-relativity simulations with multi-messenger observations of GW170817 [127, 128], and finite temperature modelling of matter [129]. Upper limits of $\lesssim 2.3\,M_\odot$ for M_{TOV} were found using angular momentum and energy considerations [130], and X-ray afterglow modelling [131], respectively.

Using $M_{TOV} \approx 2.3\,M_\odot$ as a fiducial value, which is also consistent with the mass range of J0740+6620 [48], sets the threshold between supramassive and hypermassive neutron stars at $\approx 2.8\,M_\odot$. This is very close to the total mass of the progenitor neutron stars for GW170817, $2.73^{+0.04}_{-0.01}\,M_\odot$ [55], which suggests that, on gravitational-wave data alone, the remnant of GW170817 could have been either a hypermassive neutron star or a supramassive neutron star.

Most binary neutron star simulations have been performed with equal-mass, or near equal-mass, progenitors. Immediately after the merger, for a surviving remnant, the two inner cores of the progenitor neutron stars collide and bounce, while the surrounding material is differentially rotating [101]. Shock heating increases the temperature of the remnant up to $\sim 100\,\mathrm{MeV}$ [41], exceeding the neutrino trapping temperature of 5-10 MeV [132]. The remnant continues to differentially rotate as the cores merge in $\sim 2-5\,\mathrm{ms}$. During the differential-rotation stage, the remnant is strongly emitting gravitational waves through f-mode oscillations (see Sec. 1.6).

One picture for the evolution of differentially-rotating remnants can be drawn from Ref. [126], where they show the influence of thermal pressure on equilibrium models for a $2.9\,M_\odot$ remnant with temperatures ranging up to 40 MeV. The authors find a maximum core density where the remnant collapses which depends on the amount of differential rotation and is independent of temperature. They also show that the remnant reaches the critical density by losing gravitational mass while approximately conserving the baryonic mass. The gravitational mass is lost by: secular evolution with constant differential rotation, reduction in the amount of differential rotation, and loss of thermal support. This additional thermal support extends the lifetime of the surviving post-merger remnant [e.g., 125].

Reference [40] estimated important timescales for the evolution of the post-merger remnant. The cooling timescale, estimated by assuming that neutrinos are trapped inside the post-merger remnant and escape by diffusion, is given by

$$t_{\rm cool} \approx 770 \left(\frac{M}{2.7\,M_\odot}\right) \left(\frac{R}{10\,\mathrm{km}}\right)^{-1} \left(\frac{E_\nu}{10\,\mathrm{MeV}}\right)^{2} \mathrm{ms}, \tag{1.13}$$

where E_ν is the typical neutrino energy. We estimate a cooling time of $\sim 7\,\mathrm{s}$ by using a typical neutrino energy of $\sim 30\,\mathrm{MeV}$, found in numerical-relativity simulations that implement neutrino trapping [133], though this is reasonably uncertain due to the scaling with E_ν^2.

The timescale that sets the loss of angular momentum due to gravitational waves is given by [40]

$$t_{\rm GW} \approx 150 \left(\frac{M}{2.7\,M_\odot}\right)^{-1} \left(\frac{R}{10\,\mathrm{km}}\right)^{-2} \left(\frac{f_2}{3.3\,\mathrm{kHz}}\right)^{-4} \left(\frac{e}{0.2}\right)^{-2} \mathrm{ms}, \tag{1.14}$$

where f_2 is the dominant post-merger oscillation frequency (see Sec. 1.6) and $e \equiv (a-b)/R$ is the ellipticity of the hypermassive neutron star. Here, a and

b are the semi-major and semi-minor axes of the neutron star, respectively, such that $R = (a + b)/2$. The reference value, $f_2 = 3.3\,\mathrm{kHz}$, was inferred from our model in Chapter 3 for numerical-relativity simulation of SLy equation of state with equal-mass $1.35\,\mathrm{M}_\odot$ neutron stars [95]. We make rough estimate for the ellipticity, $e \approx 0.2$, from the time evolution of the density profile for numerical-relativity simulation of LS220 equation of state with equal-mass $1.35\,\mathrm{M}_\odot$ neutron stars [97]. Numerical-relativity simulations have shown that the gravitational-wave timescale can range from $\mathcal{O}(20)\,\mathrm{ms}$ shortly after merger to $\gtrsim 0.5\,\mathrm{s}$ for longer lived simulations [99, 134].

Most postmerger numerical-relativity simulations last for only tens of milliseconds, though some longer simulations have been performed between 50-100 ms in length [135–138]. Although Eq.(1.14) shows an estimated emission time for gravitational waves of $\sim 150\,\mathrm{ms}$, the uncertainty in the equation of state could place f_2 as low as $\sim 2.2\,\mathrm{kHz}$ and some simulations show that the ellipticity reduces over time [101, 139]. Given these possibilities, a four-fold decrease in e together with a reduction in f_2 to 2.2 kHz would result in $t_{\mathrm{GW}} \sim 12\,\mathrm{s}$. Although the numerical-relativity simulations do not cover enough time period after the merger, they are vital for extracting the gravitational-wave strain in the early post-merger stage where the amplitude of the strain is at its loudest.

1.6 Gravitational-wave strain and spectra

Figure 1.3 shows a typical gravitational-wave strain from a numerical-relativity simulation. The left panel shows the inspiral and post-merger components of the gravitational-wave strain for the plus polarisation, and the right panel shows a zoom of the post-merger component only. The numerical-relativity simulation uses the SLy equation of state with equal-mass $1.35\,\mathrm{M}_\odot$ neutron stars [95, 100]. The gravitational-wave strain has a post-merger signal to noise ratio of 50 for a three detector network of LIGO Hanford, Livingston, and Virgo at advanced design sensitivity. The merger time is defined where $h_+(t)^2 + h_\times(t)^2$ reaches its first maximum. The inspiral gravitational wave ($t < 0$) shows a chirping sinusoid, increasing with frequency and amplitude until the neutron stars merge. The post-merger gravitational-wave strain ($t > 0$) has a much higher frequency than the inspiral component and has more structure in the frequency domain (see below). As mentioned in Sec. 1.5, the gravitational-wave strain in the first $\sim 2 - 5\,\mathrm{ms}$, is more erratic due to interactions of the two inner cores. The interactions of the inner cores settle down after this time resulting in a somewhat monotonic f-mode oscillation in the gravitational-wave strain.

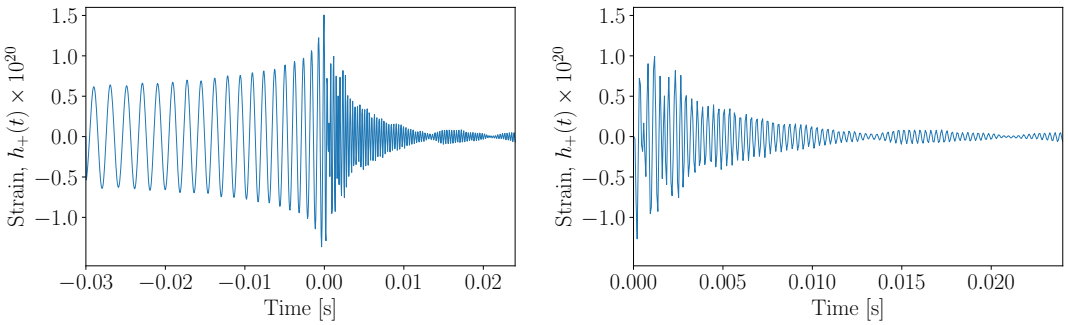

Figure 1.3: Plus polarisation of the gravitational-wave strain for inspiral and post-merger (left), and post-merger only (right). Generated from a numerical-relativity simulation using the SLy equation of state with equal-mass 1.35 $M_\odot$ neutron stars [95, 100] for a post-merger signal-to-noise ratio of 50.

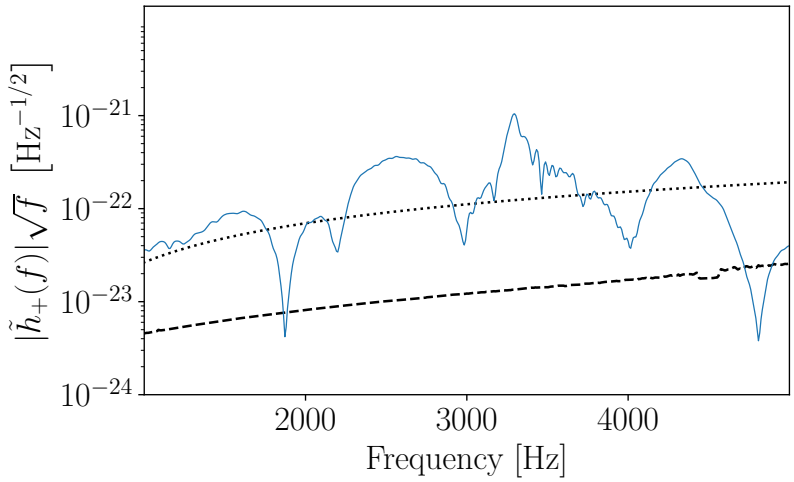

Figure 1.4: Frequency domain representation of the post-merger gravitational-wave strain shown on the right panel of Fig. 1.3. Four main spectral peaks are visible in the gravitational-wave spectrum with the dominant peak, $f_{\rm peak}$, has the largest amplitude at ~ 3300 Hz. The sensitivity curves for Advanced LIGO and Advanced Virgo are shown as dashed black, and dotted black, respectively.

The frequency response corresponding to the post-merger gravitational-wave strain in the right panel of Fig. 1.3 is shown in Fig. 1.4. The amplitude is $|\tilde{h}(f)|\sqrt{f}$, where $\tilde{h}(f)$ is the Fourier transform of the gravitational-wave strain. The post-merger gravitational-wave spectrum is dominated by primary post-merger frequency, $f_{\rm peak}$, the main f-mode oscillation of the remnant, which is ~ 3.3 kHz for this simulation [e.g., 140–142].

Two additional oscillation modes were found in simulations that were caused by the interaction between the main f-mode oscillation ($m = 2$) and the $m = 0$ radial pressure mode [142]. This results in a modulated signal that should be present in the frequency response at frequencies $f_{\rm peak} \pm f_{m=0}$, designated as f_{2-0} and f_{2+0}, respectively. The f_{2-0} peak was found to be particularly strong in spectra for high-mass mergers as long as prompt collapse does not occur [143]. Another oscillation mode, labelled $f_{\rm spiral}$, where $f_{2-0} < f_{\rm spiral} < f_{\rm peak}$ [143], was found in the spectra for low-mass mergers. This mode was generated by two antipodal bulges at the outer edge of the merger remnant that rotated at a slower frequency than $f_{\rm peak}$. The antipodal bulges were, in turn, caused by strong tidal deformation in the early post-merger stage. For higher-mass mergers that do not experience prompt collapse, the peaks associated with f_{2-0} dominate over peaks associated with $f_{\rm spiral}$ in the spectra [143]. In the mass region between

these extremes, both $f_{\rm spiral}$ and f_{2-0} can be present in the spectra of these post-merger remnants.

In a different interpretation of the post-merger spectra, the three main peaks were designated as (f_1, f_2, f_3) in ascending frequency with $f_2 = f_{\rm peak}$ [94, 101, 144]. A quasi-universal relationship was found between f_1 and a number of progenitor system properties, including the compactness C and the dimensionless quadrupolar tidal deformability Λ [101]. The spectral peak, f_1, was found to coincide with $f_{\rm spiral}$ in spectrograms for stiff equations of state but was different otherwise [94]. The power content associated with f_{2-0} was found to be extremely small in the spectrograms even though f_{2-0} can easily be measured in simulations. References [145, 146] support the interpretation of Ref. [143], citing that a larger simulation set shows that f_1 is actually a combination of $f_{\rm spiral}$ or f_{2-0} whereas a smaller simulation set, as in Refs. [94, 101, 144], is not large enough to highlight this.

Two models of the time-domain gravitational-wave strain were used for the basis for our model in Chapter 3. The first model used a third-order exponentially-damped sinusoid and successfully matched a simulation using DD2 equation of state with equal-mass $1.35\,{\rm M}_\odot$ neutron stars [147]. The second model implemented a quadratic frequency-drift term over time for $f_{\rm peak}$ and used this model to measure the neutron star radius [148]. Spectrograms from Refs. [94, 149, 150] and to a lesser extent from Ref. [151], show some frequency drifts over time in some of the frequency peaks, particularly in $f_{\rm peak}$ which lends support to the implementation of a frequency-drift term in a post-merger gravitational-wave strain model. One possible cause of frequency drift would involve the contraction or expansion of the post-merger remnant, which would increase and decrease the frequency, respectively.

With this in mind, we create a hybrid model of Refs. [147] and [148] which we use in Chapters 3 and 4. We implement a linear frequency-drift term, as opposed to the quadratic frequency-drift term used in Ref. [148]. Similarly to Ref. [147], we use an identical third-order system, to which we add the linear frequency-drift term. The model, outlined in full in Chapter 3, is $Hw_j \exp(-t/T_j) \cos\left(2\pi f_j t\left[1 + \alpha_j t\right] + \psi_j\right)$. The success of this model is indicated by fitting factors between posterior waveforms and the numerical-relativity simulation of $\gtrsim 0.92$ with most values ~ 0.95.

A number of challenges are presented by the gravitational-wave strain generated with numerical-relativity simulations. Phase errors between successive resolutions accumulate over time and it is not unusual to see phase differences of $\sim 1\,{\rm rad}$ by the time of the merger for the finest resolutions [e.g., 82]. Reference [101] examined the role of the spatial resolution on the instantaneous phase of the gravitational-wave strain and found a phase difference of $0.9\,{\rm rad}$ between the the finest resolution tests (See also Ref. [152] for a discussion on post-merger waveform robustness). This results in a loss of $\sim 40\%$ of the signal-to-noise compared to a perfectly matched signal when using a matched-filter detection.

Another challenge presented by the gravitational-wave strain generated with numerical-relativity simulations is the collapse time of the remnant. As an example, consider the following simulations from the `CoRe` gravitational-wave database using the SLy equation of state [95, 100]. These simulations are designated as THC:0036:R0x for $x \in [1-4]$ with grid sizes of $148\,{\rm m}$, $222\,{\rm m}$, $295\,{\rm m}$, and $369\,{\rm m}$, respectively [95]. The finest resolution of $148\,{\rm m}$ has a collapse time of $\sim 15\,{\rm ms}$, the remaining three simulations have collapse times of $\sim 17, \sim 24$, and

$\sim 60\,\mathrm{ms}$, respectively. Therefore, as the resolution becomes finer to reduce the phase error in the post-merger simulations, the amount of numerical-viscosity correspondingly increases, resulting in an earlier collapse of the post-merger remnant.

It may be the case that numerical-relativity simulations will not be fully calibrated to the true dynamics of post-merger remnants until we directly measure their gravitational waves. This is another motivation for simple models that are able to match the gravitational-wave strain from numerical-relativity simulations while remaining flexible to variations beyond the simulation outputs. In particular, models that can measure the collapse time of the remnant are important as numerical-relativity simulations are unable to predict this feature well.

Quasi-universal relationships have been found relating the properties of the post-merger remnant and the progenitor neutron stars. Perturbations in general relativity were used to find relationships between the frequency of neutron star f-modes and both the neutron star density and compactness [153]. The relationship between the f-mode frequency and the neutron star density was later refined using conformally-flat solutions of the Einstein field equations, and additional relationships were found between the neutron star radius and the f-mode frequency [154, 155]. Simulations of perturbed slowly-rotating neutron stars highlighted relationships between the neutron star moment of inertia, the spin-induced quadrupole moment, and the dimensionless tidal deformability [53, 156].

Relationships were then found between the progenitor neutron star ($l = 2$) dimensionless quadrupolar tidal deformability, Λ, and a number of spectral features. The maximum gravitational wave frequency at the time of merger, f_{max}, was closely related to $\Lambda^{1/5}$ for equal-mass neutron stars [157]. A linear correlation was subsequently found between $\Lambda^{1/5}$ and the dominant post-merger f-mode frequency, f_{peak}. We use this linear relationship in the model discussed in Chapter 2 to re-centre the gravitational-wave spectra after alignment.

1.7 Post-merger gravitational-wave models

In this section we briefly introduce the three main papers in Chapters 2-4 of this thesis. A common theme in all three papers is that we need methods for generating fast binary neutron star post-merger waveforms for use in the detection or parameter estimation of post-merger remnants. In Chapter 2 we use a model that is trained on both the gravitational-wave spectra and the neutron star system parameters to generate post-merger spectra. In Chapter 3 we develop a simple analytic model to generate time-domain gravitational-wave strain and test the model with Bayesian inference on numerical-relativity simulations. In Chapter 4 we develop a model to measure the collapse time of post-merger remnants and find the distance at which we can detect the post-merger collapse for different gravitational-wave detector networks.

In Chapter 2, we develop a way to generate gravitational-wave spectra in a fraction of a second. We use a hierarchical model that is trained on 35 numerical-relativity spectra from equal-mass neutron star post-merger simulations. The progenitor neutron star system is defined by the mass of the individual neutron stars, M, and the equation of state is defined by the compactness of the neutron

stars, C, and the tidal coupling constant, κ_2^T. These three parameters, together with the gravitational-wave spectra, are sufficient to train our model.

The model performance is tested with leave-one-out cross-validation and we measure noise-weighted fitting-factors of 0.95 ± 0.05 between the inferred spectra and the spectra under-test. This can be compared to 0.93 ± 0.05 which is the noise-weighted fitting-factor between the spectra of two identical neutron star systems using different numerical-relativity codes. We also show that we can use the trained model to perform parameter estimation for κ_2^T with the noise-weighted fitting-factor as a proxy likelihood.

In Chapter 3, we use a third-order exponentially-damped sinusoid with a linear frequency-drift to model the post-merger time-domain gravitational-wave strain. We perform parameter estimation with this model to generate posterior waveforms for nine post-merger numerical-relativity simulations. The noise-weighted fitting-factors between the numerical-relativity simulations and the posterior waveforms are ~ 0.95. The dominant post-merger oscillation frequency, $f_{\rm peak}$, can be constrained to $\pm^{1.4}_{1.2}\%$ for a post-merger signal-to-noise ratio of 15 and $\pm^{0.3}_{0.2}\%$ for post-merger signal-to-noise ratios of 50. We can constrain κ_2^T at a post-merger signal-to-noise ratio of 15 to $\pm^{9}_{12}\%$, and $\pm 5\%$ at post-merger signal-to-noise ratios of 50, using the hierarchical model.

In Chapter 4, we extend the model from Chapter 3 to allow the collapse of the gravitational-wave strain. We use post-merger gravitational-wave strain from numerical-relativity simulations of equal-mass $1.35\,{\rm M}_\odot$ neutron stars with LS220 and SLy equations of state. We then perform parameter estimation on the collapse time with four different gravitational-wave interferometer configurations.

We find that we need a network of Einstein Telescope with Cosmic Explorer to detect a post-merger that collapses $\sim 10\,{\rm ms}$ after the merger. Two A+ detectors at design sensitivity can measure a post-merger remnant that collapses $\sim 10\,{\rm ms}$ after the merger to a distance of $\lesssim 10\,{\rm Mpc}$. If the proposed Neutron star Extreme Matter Observatory is operational, then this distance increases to $\sim$ 18-26 Mpc thereby increasing the effective volume and hence detection rate by a factor of ~ 30.

Chapter 2

Computing Fast and Reliable Gravitational Waveforms of Binary Neutron Star Merger Remnants

Paul J. Easter
Paul D. Lasky
Andrew R. Casey
Luciano Rezzolla
Kentaro Takami

Abstract

Gravitational waves have been detected from the inspiral of a binary neutron-star, GW170817, which allowed constraints to be placed on the neutron star equation of state. The equation of state can be further constrained if gravitational waves from a post-merger remnant are detected. Post-merger waveforms are currently generated by numerical-relativity simulations, which are computationally expensive. Here we introduce a hierarchical model trained on numerical-relativity simulations, which can generate reliable post-merger spectra in a fraction of a second. Our spectra have mean fitting factors of 0.95, which compares to a fitting factor of 0.93 between different numerical-relativity codes that simulate the same physical system. This method is the first step towards generating large template banks of spectra for use in post-merger detection and parameter estimation.

2.1 Introduction

Gravitational waves have been observed from the inspiral of binary neutron star merger GW170817 [6]. This allowed limits to be placed on the neutron star tidal deformability (see e.g., [6, 55, 99, 158–160]). However, due to lack of detector sensitivity at high frequencies, the merger and post-merger signals were not detected [55, 161, 162]. Post-merger gravitational-waves from a binary neutron star merger could be detected with a signal-to-noise ratio of 5 at a distance of ∼25-40 Mpc with Advanced LIGO at design sensitivity [144]. The physics of the post-merger remnant is of particular interest as it probes the neutron star equation of state at significantly higher temperatures than the progenitor stars.

The detection and characterisation of a post-merger remnant is aided by a large bank of gravitational-wave strain waveforms. Generating such waveforms is currently computationally expensive, and there are only of order 100 in existence. In this work we make a step towards generating a large template bank of post-merger spectra by training a hierarchical model on a set of numerical-relativity spectra.

There has been significant research applied to the relationship between post-merger numerical-relativity simulations, the corresponding spectrum of the gravitational-wave strain, and the neutron star equation of state (e.g., [94, 96–98, 100, 101, 142, 144, 148, 154, 157, 163–167]). There are many degrees of freedom for each simulation, which include the neutron star system parameters, equation of state, and simulation parameters (e.g., spacetime evolution formalism [168], resolution), as well as parameters related to magnetic fields and neutrinos. We choose to use a set of numerical-relativity simulations that are homogeneous, eliminating unwanted variations between simulations with different parameters. To achieve this, we use a subset of 35 waveforms from Ref. [94] consisting of identical simulation parameters with variations in the neutron star mass and equation of state only. To obtain consistent spectra, we select waveforms that have a fixed time-step and almost identical length.

Ref. [165] showed that dimensional reduction of post-merger waveforms is possible by performing principal component analysis after aligning the maximum of each gravitational-wave strain spectra in the frequency domain (see also [148]). We use a similar method of frequency shifting in our model. We introduce a hierarchical model that trains on existing numerical-relativity post-merger simulations, and can produce new, accurate spectra in a fraction of a second. This is the first step towards making large template banks of post-merger spectra suitable for detection and parameter estimation which could compliment existing unmodelled searches for post-merger remnants [55, 169, 170].

Simulation of the post-merger phase of binary neutron star mergers is significantly more complicated than the inspiral phase due to the complex physics including shock heating and nonlinear mode coupling. Additional effects, such as neutrino cooling and magnetic fields, are not expected to yield substantial modifications to the locations of the spectral peaks (see e.g. [91, 106, 172]), while the role of viscous effects is still a matter of debate [173]. The accuracy of the resulting simulations can be limited by the trade off between computational constraints and higher resolutions [168]. This is particularly true for the phase evolution of the post-merger simulations which do not necessarily converge [100]. However, the power-spectral content is convergent for sufficiently high resolutions (e.g., [100, 101]). Our model is representative up to the validity of the numerical-relativity simulations that it is based upon. With this in mind, we wish to encourage further research into numerical-relativity simulations of post-merger remnants to increase the available number of waveforms and to enable further cross-checking between codes.

2.2 Methodology

We use 35 numerical-relativity simulations of binary neutron star mergers from Ref.[94], to which we refer to for details on the equations of state employed. Each simulation consists of non-spinning, equal-mass progenitor neutron stars, with five different equations of state across the simulations. We train our model on the amplitude of the characteristic strain spectra, $h_c(f) = |\tilde{h}(f)|\sqrt{f}$. Here, $\tilde{h}(f)$ is the Fourier transform of the plus polarisation of the post-merger gravitational-wave strain, $h_+(t > 0)$. The plus and cross polarisations of the simulated gravitational-wave strain have almost identical spectral amplitude and have a phase offset of almost exactly $\pi/2$. We gain no extra information

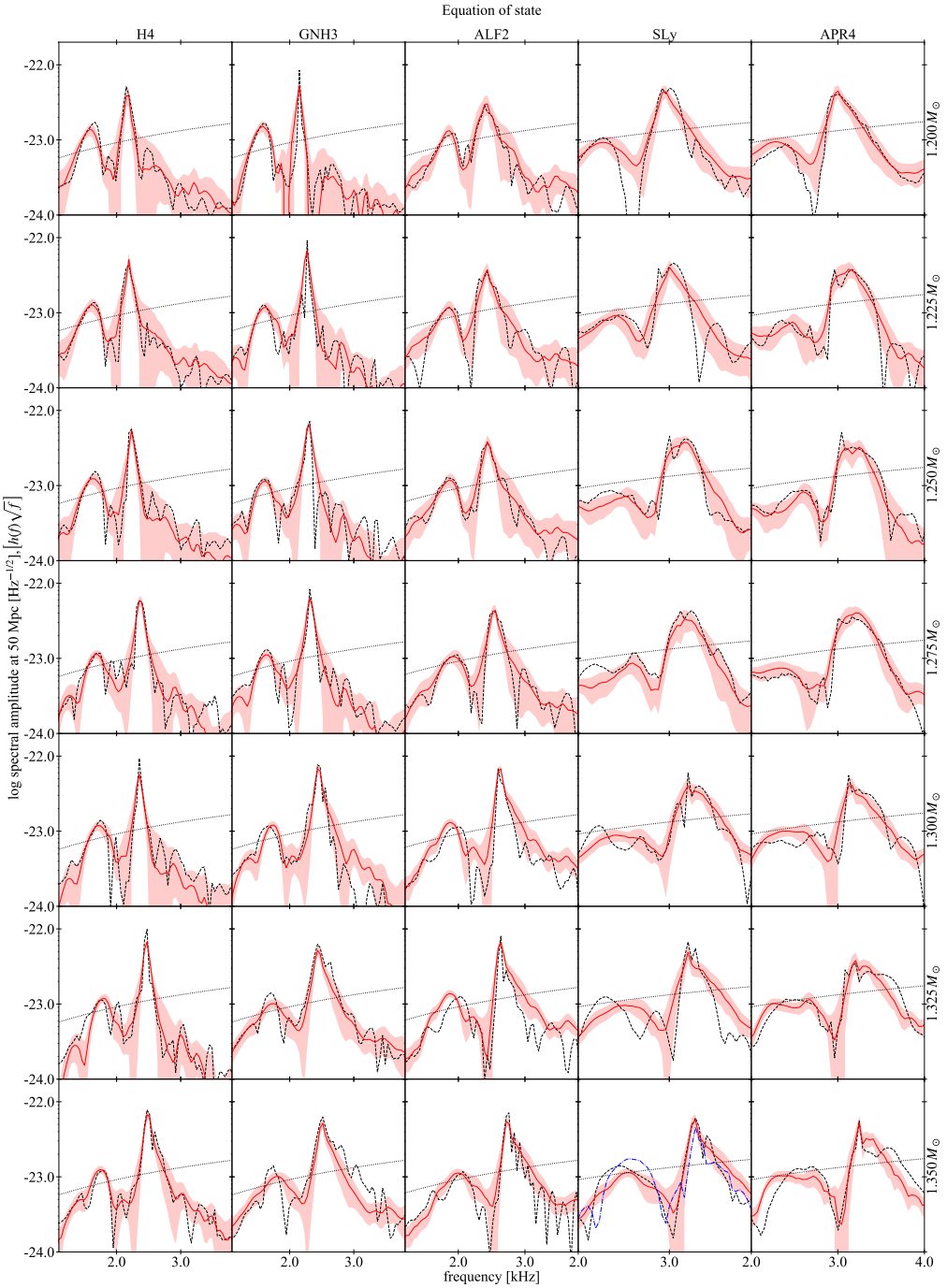

Figure 2.1: Reconstructed gravitational-wave spectra generated with leave-one-out cross-validation (solid red) and original numerical-relativity spectra [94] (dashed black), scaled to a distance of 50 Mpc. Each column represents a different equation of state and each row represents a different neutron star mass, increasing towards the bottom. The one-sigma uncertainty in the spectra is shaded in light red for each prediction. The Advanced LIGO noise amplitude spectral density (dotted black curve) [171] is shown on all subplots. A numerical-relativity spectrum generated from [100] is shown (dashed dot blue curve) in the last row (equal mass 1.35 $M_\odot$) for SLy [95] (fourth column) equation of state.

by including the cross polarisation. The merger time, $t = 0$, is defined as the time where $h_+^2(t) + h_\times^2(t)$ reaches the first maximum.

We use a hierarchical model to represent the amplitude spectra. Given a neutron star of mass M and radius R, we assume the compactness of a neutron star, $C \equiv M/R$, in the jth simulation has a power-law dependence with the mass, M, over all equations of state

$$C_j = \alpha_j M_j^{\beta_j}. \tag{2.1}$$

The validity of this model will be determined by how well we can match the numerical-relativity waveforms. The hyperparameters $\{\mathbf{a}, \mathbf{b}\}$, and the quadrupolar tidal coupling constant, κ_2^τ, determine the values of $\{\alpha, \beta\}$ as follows:

$$\alpha_j \sim \mathcal{N}(a_0 + a_1\kappa_{2,j}^\tau, \sigma_\alpha^2), \tag{2.2}$$
$$\beta_j \sim \mathcal{N}(b_0 + b_1\kappa_{2,j}^\tau, \sigma_\beta^2), \tag{2.3}$$

where $\mathcal{N}(\mu, \sigma^2)$ is a Gaussian distribution of mean μ and variance σ^2. The quadrupolar tidal coupling constant, κ_2^τ, is used due to its importance in the inspiral dynamics [94, 101, 144, 157, 164, 174] and its correlation with the location of the main frequency peak of the post-merger spectrum [101, 144, 154, 164].

All spectra in the training set, which excludes the spectrum under test when leave-one-out cross-validation is performed, are used to determine the hyperparameters $\{\mathbf{a}, \mathbf{b}\}$ by a least squares fit. The amplitudes for each spectrum are frequency shifted so that the peak frequencies are aligned in a similar way to Refs. [148, 165]. We then fit the aligned spectral amplitudes with a linear model

$$(h_c)_{i,j} = \mathbf{\Theta}_i \mathbf{X}_j + \text{noise}, \tag{2.4}$$

where the noise is modelled as intrinsic variance, s_i^2 for the ith frequency bin, $\mathbf{\Theta}_i$ is a vector of unknown coefficients, and $\mathbf{X}_j$ is a design matrix of

$$\mathbf{X}_j = [1, \widehat{C}(M_j, \kappa_{2,j}^\tau), \widehat{M}_j, \widehat{\kappa_{2,j}^\tau}]. \tag{2.5}$$

The hats indicate the whitened transformations of the neutron star parameters such that $\hat{\mathbf{x}} \sim \mathcal{N}(0, 1) = (\mathbf{x} - \mu_x)/\sigma_x$ where μ_x and σ_x^2 are the mean and variance of $\mathbf{x}$ respectively. The compactness parameter can be generated from Eqs.(2.1-2.3) after determining the values for a_0, a_1, b_0, and b_1. Spectra can then be trivially generated given any mass, quadrupolar tidal coupling constant and frequency shift. The frequency shift can be determined from the value of the quadrupolar tidal coupling constant [101, 164].

We perform leave-one-out cross-validation to test the performance of the model. We do this by excluding the spectrum under test and its associated parameters from the training set. In doing so, the spectra generated during leave-one-out cross-validation represent an extrapolation by the model and the fitting factors are therefore conservative.

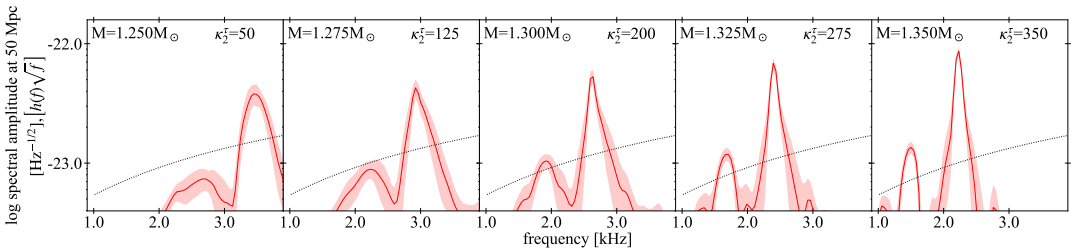

Figure 2.3: Spectra generated by the model when trained on all the numerical-relativity spectra (red). The uncertainties in the spectra are shown in light red. The Advanced LIGO noise amplitude spectral density (dotted black) is shown on all subplots.

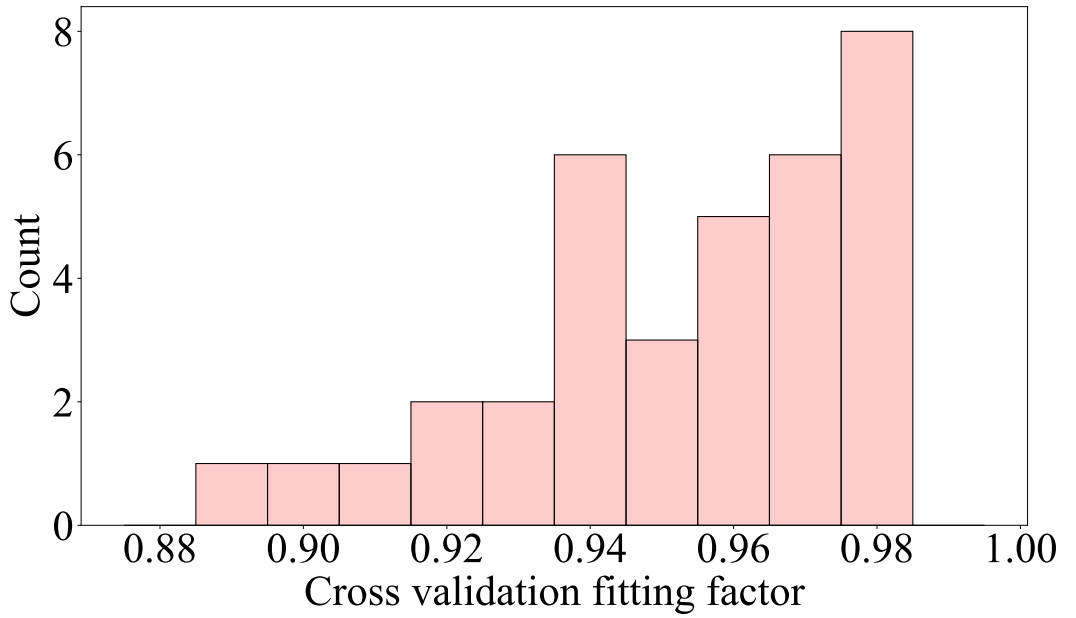

Figure 2.2: Histogram of fitting factors determined by comparing numerical-relativity spectra with spectra generated by our model using leave-one-out cross-validation.

We perform spectral comparisons using the following noise-weighted fitting factor, or overlap [175]

$$FF(h_1, h_2) \equiv \frac{\langle h_1|h_2\rangle}{\sqrt{\langle h_1|h_1\rangle \langle h_2|h_2\rangle}}. \tag{2.6}$$

Here, the inner product is defined by

$$\langle h_1|h_2\rangle \equiv 4 \int df \frac{|\tilde{h}_1(f)|\ |\tilde{h}_2(f)|}{S_h(f)}, \tag{2.7}$$

where S_h is the noise power spectral density. Throughout this article we use the `ZERO_DET_high_P` file from [171] to determine the amplitude of S_h. The resultant fitting factor is similar to the standard fitting factor except that it operates on the Fourier amplitude only. A fitting factor of one represents a perfect match. The fitting factor represents the loss incurred to the optimal signal-to-noise ratio due to mismatch in the model spectra, where the optimal signal-to-noise ratio is given by $\rho_{opt} = \sqrt{\langle h|h\rangle}$.

While it is known that smooth relationships exist between various system properties (e.g., mass, tidal parameters, etc.) and post-merger waveform spectral features [94, 101, 143, 144, 154, 164], no such relationships exist for the

phase information (see also [176]). Empirically, while we find good training fits using our model on the spectral content of the waveforms (see below), we are not able to train confidently on the full time series including both phase and amplitude as the phase evolves too quickly between adjacent simulations. We discuss this in more detail below.

2.3 Results

Following the training step, we use Eq.(2.4) to generate spectra. Figure 2.1 shows how well our generated spectra match the original numerical-relativity spectra. The original spectra are shown as dashed black curves, the cross-validation spectra are shown as red curves, and the one-sigma model uncertainty is shown in shaded light red. All spectra are scaled to a distance of 50 Mpc. The Advanced LIGO noise amplitude spectral density is shown as the dotted black curves [171]. We fit the large-scale structure of the numerical-relativity peaks well with some deviations in the small-scale structure.

Figure 2.2 shows a histogram of the noise-weighted fitting factor, Eq.(2.6), between our cross-validated model prediction and the corresponding numerical-relativity spectra for all tested waveforms. The resulting histogram has a mean of 0.95 with a standard deviation of 0.03.

To place the above results in context, we calculate the nearest neighbour fitting factor of the numerical-relativity spectra. We measure the fitting factor for the spectrum under test against all other spectra, and report the largest fitting factor. We obtain nearest neighbour fitting factors for the numerical-relativity spectra of 0.93 with a standard deviation of 0.05. The fitting factors generated by our model compare favourably with this result. Additionally, our model is capable of generating spectra given the required input parameters, whereas a nearest neighbour interpolation would not be capable of this.

As a additional baseline value for comparison, we compare fitting factors between the numerical-relativity spectra used in this paper [94], and those produced with other codes [100]. Notwithstanding the fact that post-merger waveforms can differ with resolution even when using the same code, we assume that the waveforms have similar truncation errors and compare one set of spectra using equations of state SLy [95, THC:0036:R03] for equal-mass binaries with $M = 1.35\,M_{\odot}$.

The spectrum for the comparison waveform is plotted (blue dashed dot curve) in the last row and fourth column of Fig. 2.1, corresponding to the SLy equation of state. This spectrum can be compared to the black dashed waveform from [94] in the same panel. While amplitude offsets do not change the fitting factor, differences in the frequency and the shape of the peaks do. The fitting factor between these two waveforms is 0.93. This can be attributed to the difference in the relative shapes of the two main peaks between the simulations in [94] and [95].

This comparison indicates that our fitting factors are comparable to the fitting factors between different numerical-relativity codes. We note that numerical simulations are indeed accurate enough for understanding the main structures (e.g., positions of dominant peaks) and their relationship with bulk properties of the remnant. However, our method is limited by the accuracy of the numerical-relativity simulations, which are in turn limited by computational capabilities; we discuss the implications of this below.

To evaluate how the generated spectra vary, we train on all numerical-relativity spectra and generate a grid of model spectra. We generate spectra at five equally spaced mass and quadrupolar tidal coupling constant values. The mass ranges from $M = 1.25\,M_\odot$ to $1.35\,M_\odot$, and the quadrupolar tidal coupling constant varies from $\kappa_2^\tau = 50$ to 350. The generated spectra are shown in Fig. 2.3 as the red curves, the one-sigma model uncertainty as light red shading, and the Advanced LIGO noise curve as dotted black. Each of these spectra take a fraction of a second to evaluate. We show these spectra to indicate what we can hope to achieve by implementing these models in full parameter estimation.

In Fig. 2.4 we compare the fitting factor between a spectrum generated with $M = 1.3\,M_\odot$, $\kappa_2^\tau = 100$ against spectra generated at other parameter values. We choose $\kappa_2^\tau = 100$ (for an equal-mass system this corresponds to $\Lambda = 530$) to be consistent with tidal deformability values, Λ, determined in [6, 55, 99, 158–160], under the simplified assumption that $\kappa_2^\tau \approx \frac{3}{16}\Lambda$ (noting that the equality holds for equal-mass progenitors). The location of the reference spectrum is shown with the black cross. This provides the first indication of whether this model could recover the mass and quadrupolar tidal coupling constant when trained on sufficient numerical-relativity simulations. The peak of the contour plot around the reference waveform shows that this model is selective, and may be used for parameter estimation and/or detection in the future. However, this is a task for future work and will require full Bayesian analysis with a noise implementation.

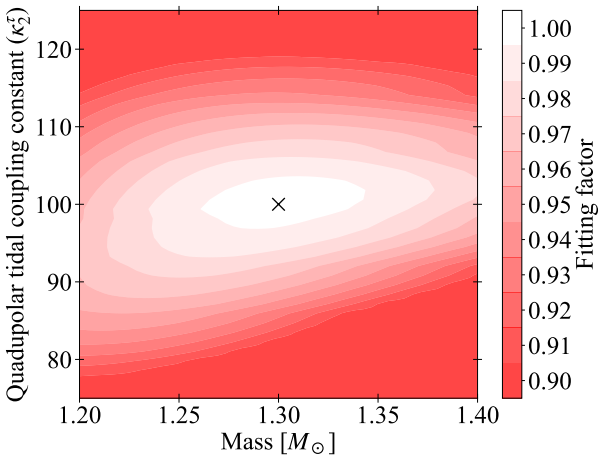

Figure 2.4: Fitting factor between spectra generated using our hierarchical model with $1.30\,M_\odot$ and κ_2^τ =100 (black cross), against a grid of mass and quadrupolar tidal coupling constant values.

It is possible that a phase transition may occur in the remnant during the post-merger phase due to an increase in density (e.g. [159, 177]). This could be detected by comparing the inferred values of the quadrupolar tidal coupling constant from the inspiral and post-merger phases. Simulations that compare hydrodynamic models with and without quark deconfinement show that the presence of quark deconfinement causes no change in the inspiral gravitational-wave signal due to the low densities involved. This is contrasted to the post-merger phase where the densities are greater, leading to a higher proportion of deconfined quarks when modelled, which in turn leads to a change in the post-merger gravitational-wave strain [178]. Phase transitions due to quark deconfinement could be detected by training our model on simulations that dis-

allow quark deconfinement. If a post-merger signal was detected that contained the signature of quark-deconfinement then this would result in an inconsistency between the tidal coupling constant inferred from the post-merger gravitational-wave spectra and the inspiral phase. We note that other mechanisms, either physical or arising from errors in the modelling, could also cause such frequency shifts. We leave the exploration of this as future work.

2.4 Discussion

In this paper, we use a hierarchical model to generate binary neutron star post-merger spectra by training on spectra generated with numerical-relativity simulations. Our trained model allows us to generate spectra in $\sim 10^{-4}$ seconds, which significantly reduces the computational effort required to populate a template bank of spectra. We obtain noise-weighted, amplitude-only fitting-factors across all tested spectra, with a mean of 0.95 and a standard deviation of 0.03. This compares favourably to a post-merger fitting factor of 0.93 between different numerical-relativity codes.

Training on the phase of the post-merger spectra will allow fitting factor comparisons with both the amplitude and phase information, as well as the generation of time-based waveforms. In addition, it will provide insight on the number of numerical-relativity simulations required to achieve a complete and accurate database. While obtaining information on the phase evolution is in principle possible, see, e.g., [148], this also requires a systematic investigation that goes well beyond the scope of this work. Without the phase information, a matched filter search is less sensitive, but it is still possible to design such a search using only the signal amplitudes.

Results based on our trained model suggest that the model is selective and could potentially be used in parameter estimation of detected events. If posteriors for the mass and tidal coupling constant are able to be determined, then it is a simple step to calculate the posteriors for the compactness, Eq.(2.1), and the radius of the neutron star. This will be confirmed in future work using a Bayesian framework. Parameter estimation of the post-merger spectra could set bounds on the post-merger quadrupolar tidal coupling constant, allowing comparison with the inspiral value. This could determine whether a phase change in the equation of state is present [177, 178].

To be valuable in search and parameter-estimation studies, our model must be extended to include individual values of mass, spins, compactness and quadrupolar tidal deformabilities for each progenitor. This paper trained on waveforms with progenitor κ_2^τ values ranging from 50 to 350, and equal-mass progenitors from 1.2 to 1.35 $\mathrm{M}_\odot$. The merger of two progenitors with the same parameters (C, M, κ_2^τ), but different equations of state could produce different output spectra, for example if one equation of state had a lower maximum, non-rotating neutron star mass. This could be a problem for the existing model and an additional input parameter may be needed to remove the degeneracy in the output spectra. This is not necessary for the numerical-relativity simulations that are used in the paper, as there is enough variation in the three parameters to define the output spectra. The model may be also expanded to include simulations with black hole progenitors. In this case the dominant post-merger frequency, corresponding to black hole ring-down, would likely be too high for detection with advanced LIGO. These changes can be introduced given

enough numerical-relativity simulations to cover the required ranges of parameter values. The placement of numerical-relativity simulations to enable this is a subject of future work. Our method may eventually provide an additional tool to aid in the detection of short-term post-merger neutron star remnants, supplementing the existing tools [169, 170].

Acknowledgments

PDL is supported through Australian Research Council (ARC) Future Fellowship FT160100112 and ARC Discovery Project DP180103155, ARC is supported in part by the Australian Research Council through Discovery Grant DP160100637. We thank James Clark and Eric Thrane for their feedback.

Chapter 3

Detection and parameter estimation of binary neutron star merger remnants

Paul J. Easter
Sudarshan Ghonge
Paul D. Lasky
Andrew R. Casey
James A. Clark
Francisco Hernandez Vivanco
Katerina Chatziioannou

Abstract

Detection and parameter estimation of binary neutron star merger remnants can shed light on the physics of hot matter at supranuclear densities. Here we develop a fast, simple model that can generate gravitational waveforms, and show it can be used for both detection and parameter estimation of post-merger remnants. The model consists of three exponentially-damped sinusoids with a linear frequency-drift term. We test the model against nine equal-mass numerical-relativity simulations selected for emission of gravitational waves for $\gtrsim 25\,\mathrm{ms}$. The median fitting factors between the model waveforms and numerical-relativity simulations exceed 0.90. We detect remnants at a post-merger signal-to-noise ratio of ≥ 7 using a Bayes-factor detection statistic with a threshold of 3000. We can constrain the primary post-merger frequency to $\pm^{1.4}_{1.2}\%$ at post-merger signal-to-noise ratios of 15 with an increase in precision to $\pm^{0.3}_{0.2}\%$ for post-merger signal-to-noise ratios of 50. The tidal coupling constant can be constrained to $\pm^{9}_{12}\%$ at post-merger signal-to-noise ratios of 15, and $\pm 5\%$ at post-merger signal-to-noise ratios of 50 using a hierarchical inference model.

3.1 Introduction

Gravitational waves have been directly detected from the inspiral of binary neutron star mergers [6, 27]. The post-merger remnant may promptly collapse into a black hole, or form a hot, differentially-rotating neutron star [102, 179], which emits gravitational waves [e.g., 180–183]. Numerical-relativity simulations of post-merger remnants show relationships between the gravitational-wave spectra and a number of progenitor properties through quasi-universal relationships [e.g., 93, 94, 101, 143, 144, 154, 155, 163, 164, 177]. Of particular interest is the relationship between the progenitor tidal coupling constant and the primary post-merger oscillation frequency for baryonic equations of state [94, 101, 152, 164], which can be used to place constraints on the tidal coupling constant.

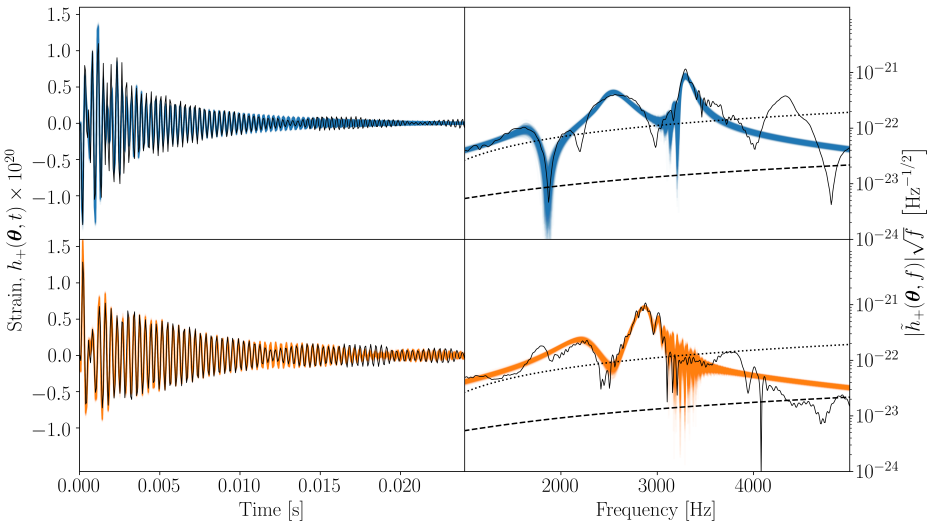

Figure 3.1: Waveform reconstruction of numerical-relativity post-merger signal injections. Top panels: time (left) and frequency (right) domain reconstructions of a numerical-relativity simulation using the SLy equation of state with equal-mass, $1.35\,\mathrm{M}_\odot$, neutron stars (waveform SLy-M1.350-Λ390). The post-merger waveform (black curve) is injected at a post-merger signal-to-noise ratio of 50. The reconstructed waveforms are shown in blue. Bottom panels: same as the top panels except the injected waveform is using the LS220 equation of state with equal mass, $1.35\,\mathrm{M}_\odot$, neutron stars (waveform LS220-M1.350-Λ684). The reconstructed waveforms are shown in orange. Noise sensitivity curves are shown for Advanced LIGO (dashed black) and Advanced Virgo (dotted black) for plots on the right.

Gravitational-wave spectra generated from numerical-relativity simulations show consistent features related to the dynamics of the surviving remnant. A dominant peak, designated as f_{peak} [184], is produced by the fundamental oscillations of the bar-mode deformed post-merger remnant [e.g., 91, 135, 154, 185, 186]. The frequencies of four possible peaks can be labelled as $(f_{2-0}, f_{\mathrm{spiral}}, f_{\mathrm{peak}}, f_{2+0})$ in ascending order [143]. The peaks at frequencies f_{2-0}, f_{2+0} may result from coupling between a quasi-radial oscillation mode and f_{peak} [142]. The peak at frequency f_{spiral} may result from the slower rotation-rate of tidally-deformed matter at the outer edges of the post-merger remnant [143]. See Refs. [101, 144] for an alternative proposed explanation of the frequency peaks.

In this paper, we develop a Bayesian detection and parameter-inference pipeline. Normally these pipelines require a large bank of waveforms. Numerical-relativity simulations cannot be used to generate these waveforms as each simulation requires $\sim \mathcal{O}(10^5)$ CPU hours to complete [101]. We develop a fast, simple model of gravitational waves for post-merger remnants that phenomenologically incorporates the main frequencies previously mentioned. Our model produces waveforms in a time-frame that is suitable for use in detection and parameter estimation of binary neutron star post-merger remnants.

We match nine equal-mass numerical-relativity waveforms with gravitational-wave emission for $\gtrsim 25\,\mathrm{ms}$ with fitting factors of 0.92-0.97. This model addresses the two restrictions that prevent matched filtering of post-merger gravitational-wave strain: computational time and poor fitting factors. Our model is derived from a hybrid of the two models outlined in Refs. [147] and [148]. Our model is agnostic to the locations of the frequency peaks and uses Bayesian statistics to determine the actual peak frequencies.

Furthermore, the addition of a frequency drift term allows for secular changes in the frequency peak locations. With post-merger signal-to-noise ratios of ≥ 15, the model can localise the primary post-merger frequency to $\pm^{1.4}_{1.2}\%$ at 95% confidence, reducing to $\pm^{0.3}_{0.2}\%$ at post-merger signal-to-noise ratio of 50. Using the hierarchical model developed in Ref. [2] we can then constrain the tidal parameters and compactness of the progenitor neutron stars. The tidal coupling constant is constrained to $\pm^{9}_{12}\%$ at post-merger signal-to-noise ratios of 15 for a 95% confidence interval. At post-merger signal-to-noise ratios of 50 this tightens to $\pm 5\%$.

In Section 3.2 we outline the model and associated methods used in this paper. In Section 3.3 we validate the model fits in the time and frequency domains and quantify the goodness of the fits. In Section 3.4 we use a Bayes factor detection statistic to determine at what post-merger signal-to-noise ratios a detection occurs and test how the model performs due to uncertainty in the inspiral coalescence time. In Section 3.5 we calculate posteriors of the dominant post-merger frequency and introduce the hierarchical model from Ref. [2] to find the equation of state parameters for the progenitors. We find constraints on both the tidal coupling constant and the compactness of the progenitors.

3.2 Methodology

We adopt a model for the post-merger gravitational-wave signal consisting of three exponentially damped sinusoids [147] with additional linear frequency drift terms [148]. The plus, $h_+(\boldsymbol{\theta}, t)$, polarisation of the gravitational-wave strain is extracted from the right circular polarisation, $h(\boldsymbol{\theta}, t)$, as follows:

$$h(\boldsymbol{\theta}, t) = h_+(\boldsymbol{\theta}, t) - \mathrm{i}\, h_\times(\boldsymbol{\theta}, t) \tag{3.1}$$

$$= \sum_{j=0}^{2} h_{j,+}(\boldsymbol{\theta}, t) - \mathrm{i}\, h_{j,\times}(\boldsymbol{\theta}, t), \tag{3.2}$$

$$h_{j,+}(\boldsymbol{\theta}, t) = H w_j \exp\left[-\frac{t}{T_j}\right] \cos\left(2\pi f_j t\left[1 + \alpha_j t\right] + \psi_j\right). \tag{3.3}$$

Here, $\boldsymbol{\theta} = \{H, w_j, T_j, f_j, \alpha_j, \psi_j : j \in [0, 2]\}$ are the model parameters where H is the amplitude scaling factor and w_j is the relative scaling factor for each mode, $j \in [0, 2]$, such that $\sum_j w_j = 1$. The initial frequency of each mode is given by f_j, T_j are the damping times, ψ_j are the initial phases, and α_j are the frequency drift terms. The time, t, is defined such that $t = 0$ corresponds to the coalescence time when the maximum of $h_+^2(\boldsymbol{\theta}, t) + h_\times^2(\boldsymbol{\theta}, t)$ occurs [e.g., 2, 94, 101, 157]. The cross polarisation of the jth mode is generated by a $\pi/2$ phase shift on $h_{j,+}(\boldsymbol{\theta}, t)$. Setting $\alpha_j = 0$ allows detection of signals corresponding to the cross-polarisation model in Ref. [147]. These equations are a subset of the plus polarisation model in Ref. [148] with the quadratic drift term set to zero and no explicit modulation of spectral peaks.

We use nine post-merger numerical-relativity simulations from Ref. [100] (see Appendix 3.A for details), selecting only simulations with equal-mass progenitors where a nascent neutron star survives for at least $\sim 25\,\mathrm{ms}$. For equal-mass systems, the tidal parameter of the neutron stars is related to the dimensionless

compactness, $C = GM/(Rc^2)$, and the second Love number, k_2, as follows:

$$\tilde{\Lambda} = \frac{2}{3} k_2 C^{-5}, \tag{3.4}$$

$$\kappa_2^{\mathrm{T}} = \frac{1}{8} k_2 C^{-5}, \tag{3.5}$$

where $\tilde{\Lambda}$ is the quadrupolar tidal deformability and κ_2^{T} is the total quadrupolar tidal coupling constant. Here, M is the neutron star mass, R is the neutron star radius, G is the gravitational constant, and c is the speed of light. The tidal properties of the progenitors can be estimated from the dominant post-merger frequency using relations found from numerical-relativity simulations with baryonic equations of state [101, 177] (although see Refs. [159, 177, 178] for the consequences of a phase transition to strange matter). We discuss this more in Section 3.5.

We inject numerical-relativity waveforms at various post-merger signal-to-noise ratios into a three-detector network (LIGO Hanford, Livingston, and Virgo) at design sensitivity for each interferometer [171, 187]. We inject the post-merger signal at a fixed time and fixed sky position, assuming that we know the coalescence time from the inspiral stage. In Section 3.4 we test this assumption by determining the uncertainty in the coalescence time for various signal-to-noise ratios. We use the Bilby package [1] with the Dynesty sampler [188] to sample posteriors, $p(\boldsymbol{\theta}|d)$, of the model parameters using the likelihood, $\mathcal{L}(d|\boldsymbol{\theta})$, as follows:

$$p(\boldsymbol{\theta}|d) = \frac{\mathcal{L}(d|\boldsymbol{\theta})\pi(\boldsymbol{\theta})}{\mathcal{Z}}, \tag{3.6}$$

$$\mathcal{Z} = \int_{\boldsymbol{\theta}} d\boldsymbol{\theta} \mathcal{L}(d|\boldsymbol{\theta})\pi(\boldsymbol{\theta}), \tag{3.7}$$

$$\mathcal{L}(d|\boldsymbol{\theta}) \propto \exp\Big[-\Big\langle d(t) - h(\boldsymbol{\theta}, t), d(t) - h(\boldsymbol{\theta}, t) \Big\rangle \Big]. \tag{3.8}$$

Here, $d(t) = s(t) + n(t)$ is the numerical-relativity waveform, $s(t)$, injected into noise, $n(t)$. We simulate ten different Gaussian noise realisations with Bilby, to examine the response of the model to variations in detector noise. We limit this to ten noise realisations to keep the computation time manageable. The priors on the model parameters are $\pi(\boldsymbol{\theta})$. The noise-weighted inner product in Eq.(3.8) is defined by:

$$\langle h_1, h_2 \rangle \equiv 4\,\mathrm{Re} \int df \frac{\tilde{h}_1(f)\tilde{h}_2^*(f)}{S_h(f)}, \tag{3.9}$$

where S_h is the detector's noise power spectral density. We use a sampling frequency of 16384 Hz to eliminate aliasing of the upper sidebands. We use constrained priors to sort the maximum amplitude for $\tilde{h}_{j,+}(\boldsymbol{\theta}, f)$, such that $|\tilde{h}_{j,+}(\boldsymbol{\theta}, f)|_{max} > |\tilde{h}_{j+1,+}(\boldsymbol{\theta}, f)|_{max}$. This ensures that the mode zero ($j = 0$) exponentially damped sinusoid corresponds to the dominant post-merger frequency. Full details on the priors are given in Appendix 3.B. The optimal post-merger signal-to-noise ratio, ρ_{opt}, is calculated from the quadrature sum of the optimal post-merger signal-to-noise ratio for each of the three detectors, $\rho_{\mathrm{opt},i}$ as follows:

$$\rho^2_{\mathrm{opt}} = \sum_{i \in \mathrm{HLV}} \rho^2_{\mathrm{opt},i} \quad , \tag{3.10}$$

for $t \geq 0$. The matched filter signal-to-noise ratio for a single detector is given by:

$$\rho_{mf} = \frac{\langle d, h(\boldsymbol{\theta})\rangle}{\langle h(\boldsymbol{\theta}), h(\boldsymbol{\theta})\rangle^{\frac{1}{2}}} \quad . \tag{3.11}$$

3.3 Model Validation

Figure 3.1 shows the posterior waveforms in the time and frequency domain for the plus polarisation of two numerical-relativity post-merger simulations. The two gravitational-wave simulations, SLy-M1.350-Λ390 (THC:0036:R03, top) and LS220-M1.350-Λ684 (THC:0019:R05, bottom) are injected at a post-merger signal-to-noise ratio of 50. These waveforms are chosen for compatibility with the inferred properties of Λ from GW170817 [6, 55, 99, 158–160]. SLy-M1.350-Λ390 is a simulation of equal progenitor mass $1.35\,M_\odot$ neutron stars with tidal deformability, $\tilde{\Lambda} = 390.1$ ($\kappa_2^{\mathrm{T}} = 73.14$) and SLy equation of state. Similarly, LS220-M1.350-Λ684 has masses of $1.35\,M_\odot$, $\tilde{\Lambda} = 683.8$ ($\kappa_2^{\mathrm{T}} = 128.2$) and LS220 equation of state.

We generate posterior waveforms by randomly drawing samples from the posterior distribution $p(\boldsymbol{\theta}|d)$. The posterior waveforms are shown as blue (top, SLy-M1.350-Λ390) and orange (bottom, LS220-M1.350-Λ684) curves in Fig. 3.1. The solid black curves show the injected numerical-relativity waveforms. As can be seen in the time-response plots (Fig. 3.1, left), the posterior samples are tightly clustered around the numerical-relativity simulations, particularly for the first $\sim$ 15 ms. The phase of waveform SLy-M1.350-Λ390 is lost after $\sim$ 15 ms (Fig. 3.1, upper left) though the majority of the spectral content is contained in the first 5 ms (see Fig. 3.4). We note that accumulated phase errors in numerical-relativity simulations increase over time.

The frequency-response plots are shown on the right side of Fig. 3.1, along with the amplitude spectral density of Advanced LIGO (dashed black curve) and Advanced Virgo (dotted black curve) at design sensitivity. The primary frequency peaks are well recovered for both reference waveforms. Two low frequency peaks of SLy-M1.350-Λ390 are resolved in preference to the upper frequency peak, whereas only one low frequency peak is resolved for LS220-M1.350-Λ684. The other two modes are located at the main frequency peak of LS220-M1.350-Λ684.

To measure the extent of the waveform mismatch, we calculate the noise-weighted fitting factor between the injected numerical-relativity waveform, $d(t)$, and the posterior waveform, $h(\boldsymbol{\theta}, t)$, [175]:

$$\mathcal{F}(d(t), h(\boldsymbol{\theta}, t)) \equiv \frac{\langle d(t)|h(\boldsymbol{\theta}, t)\rangle}{\sqrt{\langle d(t)|d(t)\rangle \, \langle h(\boldsymbol{\theta}, t)|h(\boldsymbol{\theta}, t)\rangle}}. \tag{3.12}$$

The fitting factor, calculated with noise from one detector at Advanced LIGO design sensitivity [171], quantifies the loss in signal-to-noise due to signal mismatch in relation to an optimal signal-to-noise ratio, Eq.(3.10).

The median fitting factors are 0.92 and 0.95, for SLy-M1.350-Λ390 and LS220-M1.350-Λ684, respectively. As the detection rate scales as $\mathcal{F}^3$ [175], the reduction in detection rate due to the above mismatch is 22% and 14% respectively for these two waveforms.

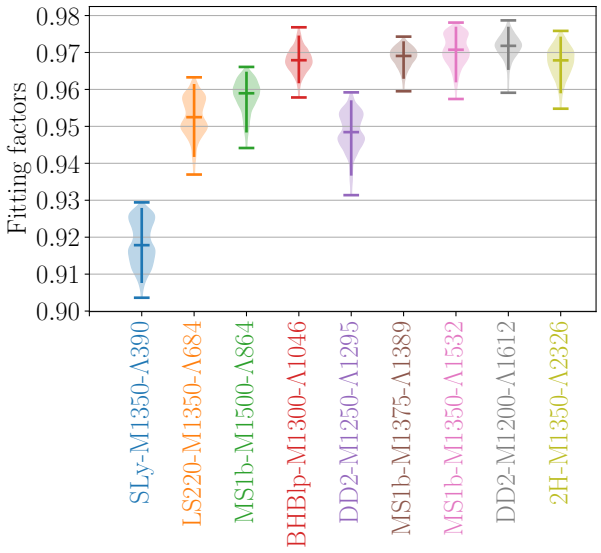

Figure 3.2: Fitting-factor distributions, $\mathcal{F}(d(t), h(\boldsymbol{\theta}, t))$, for each post-merger numerical-relativity waveform. The signal-to-noise ratio for the post-merger gravitational-wave strain for each waveform is 50. The upper and lower horizontal bars represent 99.7% confidence intervals. The central horizontal bar shows the median value. The thick vertical line shows the 95% confidence intervals. The median fitting factors range between 0.92 to 0.97 which corresponds to a reduction in detection rate from 22% down to 9% due to mismatch with the numerical-relativity injections.

The fitting factors for all nine numerical-relativity simulations are shown in Fig. 3.2, with each simulation represented by a different colour. Ten different Gaussian noise realisations are used for each numerical-relativity simulation. The 99.7% confidence intervals for the fitting factors are shown by the upper and lower horizontal bars. The median value is shown by the central horizontal bar, and 95% confidence intervals are indicated by thick vertical bars. Finally, the distribution of the fitting factors are shown by the width of the shaded areas. The lowest fitting factors, for simulation, SLy-M1.350-Λ390, have an average match of 0.92. Other numerical-relativity injections have fitting factors of $0.95 - 0.97$. The injection with the softest equation of state under-performs the other injections. This is due to complex dynamics of the nascent neutron star in the first $\sim 2\,\mathrm{ms}$.

3.4 Sensitivity

We calculate the Bayes factor between the signal hypothesis and a noise hypothesis to evaluate the sensitivity of our model. We do this by injecting the post-merger signal SLy-M1.350-Λ390 into ten different noise realisations at various signal-to-noise ratios. The results are shown in Fig. 3.3. The distribution of the natural logarithm of the Bayes factor, $\ln(\mathcal{BF})$, is shown for each post-merger signal-to-noise ratio along with the 99.7% confidence intervals (upper and lower horizontal bars) and the median value (middle horizontal bar). We define that strong evidence for a signal hypothesis over a noise hypothesis corresponds to a Bayes factor exceeding 3000 ($\ln(\mathcal{BF}) > 8.0$) [e.g., 189]. In this case a signal hypothesis is 3000 times more likely than a noise hypothesis. This occurs with post-merger signal-to-noise ratios of $\gtrsim 10$ for all tested noise real-

isations. There are some noise realisations where the Bayes factor threshold is exceeded for post-merger signal-to-noise ratios of $\approx$ 7-9.

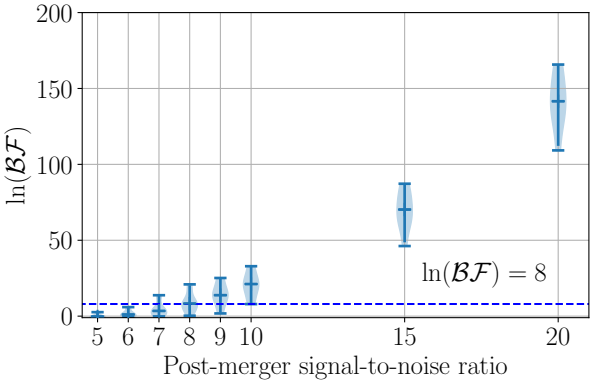

Figure 3.3: Natural logarithm of the Bayes factor comparing a signal hypothesis against a noise hypothesis plotted against the post-merger signal-to-noise ratio. The numerical-relativity waveform, SLy-M1.350-Λ390, is injected into ten different noise realisations at the specified signal-to-noise ratio. The upper and lower horizontal bars show the 99.7% confidence intervals of the log Bayes factor and the central horizontal bar shows the median value. A post-merger signal-to-noise value of $\gtrsim 10$ is required to ensure strong evidence for a signal hypothesis ($\ln(\mathcal{BF}) > 8$) across all ten noise realisations. However, there are some noise realisations where $\ln(\mathcal{BF}) > 8$ occurs for post-merger signal-to-noise ratios as low as 7.

An important consideration for our signal model is the uncertainty in the coalescence time as measured from the gravitational-wave inspiral signal. This determines how close we can get to the true coalescence time for the binary neutron star merger. In Fig. 3.4 we investigate the model performance to uncertainties in the coalescence time. We show how the fitting factor and matched-filter signal-to-noise ratio change when starting the adopted model at various times after the coalescence time. We multiply the numerical-relativity injection, $d(t)$, by the Heaviside step function, $\mathcal{H}(t - t_{delay})$, and evaluate the model, $h(\boldsymbol{\theta}, t - t_{delay})$, for $t \geq t_{delay}$. The matched filter signal-to-noise ratio is calculated using Eq.(3.11) with a single detector at Advanced LIGO sensitivity. We use numerical-relativity injection, SLy-M1.350-Λ390, selected due to compatibility with the tidal parameters inferred from GW170817. A delay time of zero includes the entire post-merger waveform, whereas a delay time of 2 ms excludes the first 2 ms of the injection after the coalescence time. The fitting factor is lower (~ 0.91) for small delay times and increases to $\sim$ 0.96 at 2 ms. The fitting factor is lower in the first 2 ms due to complex dynamics of the nascent neutron star. In Fig. 3.4, the matched-filter signal-to-noise ratio is almost monotonically decreasing as expected. Even though the fitting factors are lower at zero delay time, the matched-filter signal-to-noise ratio is at maximum. Therefore, from a sensitivity perspective, a minimum delay time is preferred.

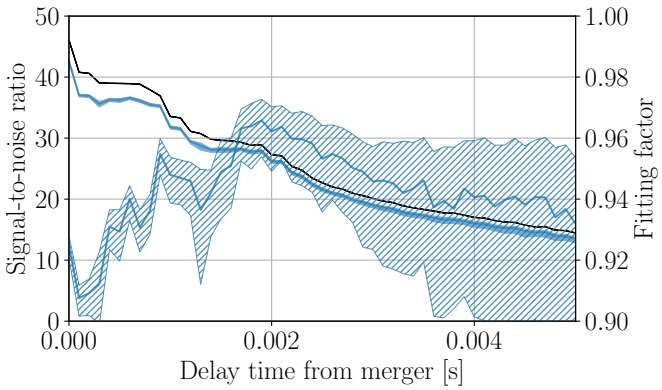

Figure 3.4: Variation of fitting factor (hatched blue) and matched filter signal-to-noise ratio (solid blue) for differing values of the delay time after the time of coalescence. The shaded regions show 95% confidence intervals. The optimal signal-to-noise ratio is also shown (solid black). Although the fitting factor is lower when the entire post-merger signal is used, the matched filter signal-to-noise ratio is largest. The fitting factor is lower for smaller delay-times due to the complex dynamics of the nascent neutron-star.

To estimate the uncertainties of the time of coalescence of the inspiral signal as a function of the signal-to-noise ratio of the inspiral signal, we use a Fisher matrix approximation. We assume that the signal parameters $\boldsymbol{\vartheta}$ follow a Gaussian distribution:

$$p\left(\Delta\boldsymbol{\vartheta}\right) \propto \exp\left[-\frac{1}{2}\Gamma_{ij}\Delta\vartheta^{i}\Delta\vartheta^{j}\right]. \tag{3.13}$$

Here, $\Delta\vartheta_i = \vartheta^i - \hat{\vartheta}^i$, $\hat{\vartheta}^i$ are the best fit inspiral parameters and $\Gamma_{ij} = (\partial h/\partial\vartheta_i|\partial h/\partial\vartheta_j)$ is the expected Fisher information matrix. The estimated errors of the parameters, ϑ_i, are obtained by taking the diagonal elements of the Fisher information matrix. The relevant parameters within our approximation are $\boldsymbol{\vartheta} = (\mathcal{M}, q, \phi_c, \tilde{\Lambda}, t_c, H)$, where $\mathcal{M}$ is the chirp mass, q is the mass ratio, ϕ_c is the phase of coalescence. The average-weighted tidal deformabilty is $\tilde{\Lambda}$, t_c is the time of coalescence and H is the amplitude of the inspiral waveform. We calculate the errors on ϑ_i assuming an equal-mass $1.4\,M_\odot$ non-rotating progenitor system. The expected uncertainties for the coalescence time are shown in Fig. 3.5. The left axis shows the inspiral signal-to-noise ratio for an optimally oriented source into a two detector LIGO network at design sensitivity. We use Fig. 8 from Ref. [190] to determine the luminosity distance, D_L, from the inspiral signal-to-noise ratio. We calculate the product of $D_{L0} \approx 475\,\mathrm{Mpc}$ (at $z \approx 0.1$) with the corresponding inspiral signal-to-noise ratio, $\rho_{inspiral,0} \approx 7$. We inject the numerical-relativity post-merger waveform, SLy-M1.350-Λ390, at luminosity distance, $D_L = D_{L0}\,(\rho_{inspiral,0}/\rho_{inspiral})$, and evaluate the post-merger signal-to-noise ratio using the Advanced LIGO and Virgo detector network at design sensitivity. The right axis in Fig. 3.5 shows the corresponding post-merger signal-to-noise ratio.

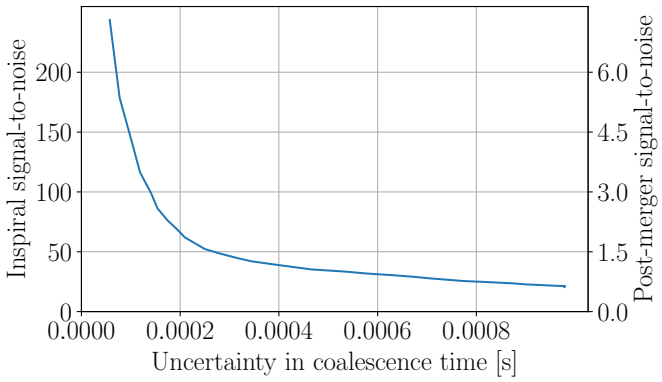

Figure 3.5: Uncertainty in coalescence time plotted with signal-to-noise ratios. The coalescence time uncertainty has been determined by a Fisher matrix approximation. The left axis is the signal-to-noise ratio for a two detector network of Advanced LIGO at design sensitivity for a binary neutron star inspiral. The right axis is the post-merger signal-to-noise ratio for a three detector network of Advanced LIGO and Advanced Virgo at design sensitivity using numerical-relativity simulation SLy-M1.350-Λ390. Post-merger signal to noise ratios above 6.0 have coalescence time uncertainties of less than 0.1 ms.

For post-merger signal-to-noise ratios larger than 6, the uncertainty in the coalescence time is less than 0.1 ms. This shows that, for post-merger signal-to-noise ratios of interest in this work, the coalescence time is similarly constrained. The uncertainty in coalescence time can be related to Fig. 3.4 to show that the resultant matched filter signal-to-noise ratio is not significantly reduced due to the uncertainty in the coalescence time.

3.5 Parameter estimation

Estimation of the primary post-merger frequency is another important indicator of the model performance. We estimate this by calculating posteriors of the peak frequency, $f_{\rm peak}$, of the dominant mode. Fig. 3.6 shows posteriors of $f_{\rm peak}$ as a function of post-merger signal-to-noise ratio. These have been calculated for an injection of SLy-M1.350-Λ390 at post-merger signal-to-noise ratios of ≥ 9. The noise realisation was kept the same for all injections. Blue shading indicates regions of 95% confidence intervals and the median values are shown as blue dots. The frequency corresponding to the maximum value of the characteristic strain spectrum of the numerical-relativity signal, $|\tilde{s}_+(f)|\sqrt{f}$, is shown as a black horizontal line. This can be thought of as an approximation of the true injected value of $f_{\rm peak}$. The $f_{\rm peak}$ frequency is constrained within 95% confidence intervals to $3310\pm^{46}_{38}$ Hz at a post-merger signal-to-noise ratio of 15 which corresponds to $\pm^{1.4}_{1.2}$%. At a post-merger signal-to-noise ratio of 50, the precision increases to $3296\pm^{11}_{8}$ Hz ($\pm^{0.3}_{0.2}$%). The posteriors for f_0, α_0, f_1 and α_1, determined for all numerical-relativity injections at a post-merger signal-to-noise ratio of 50, are shown in Figs. 3.C.1-3.C.9 in Appendix 3.C.

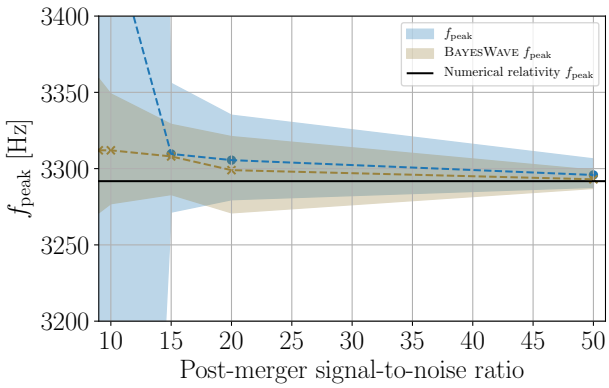

Figure 3.6: Primary post-merger frequency comparison between our model (blue) and BayesWave (brown). The posteriors are plotted against the post-merger signal-to-noise ratio for injection SLy-M1.350-Λ390. The 95% confidence intervals are shaded. The median points are shown as blue dots and brown crosses, for our model and BayesWave, respectively. The frequency corresponding to the peak of the spectral response of the injection is also shown (solid black line).

We also analyse injections of SLy-M1.350-Λ390 using BayesWave [191, 192]. BayesWave uses a variable number of Morlet-Gabor wavelets to model the signal, where both the number and the properties of the wavelets are marginalised over. This is an established method for post-merger studies [27, 55]. References [170, 193] have performed simulations using BayesWave to infer the post-merger properties of binary neutron star mergers. We compute the posteriors of the spectral frequency peak, $f_{\rm peak}$, using BayesWave following Ref. [170]. Here, $f_{\rm peak}$, the frequency of the highest peak in the Fourier power spectrum of the signal, is determined for each sample from the BayesWave posterior. For samples that do not have a peak, $f_{\rm peak}$ is computed using random draws from its prior [170]. Figure 3.6 shows the 95% confidence intervals of $f_{\rm peak}$ for each post-merger signal-to-noise ratio in brown. The median values are shown as brown crosses. The BayesWave frequency posteriors are consistent with Refs. [170, 193].

The posteriors for $f_{\rm peak}$ are similarly constrained for both BayesWave and our model for post-merger signal-to-noise ratios of $\gtrsim 20$. BayesWave is more constrained for post-merger signal-to-noise ratios of $\sim 9-15$. Both methods are able to recover the injected dominant post-merger frequency. BayesWave can generate very high fitting factors; the fitting factors for SLy-M1.350-Λ390 at a post-merger signal-to-noise ratio of 50 are ≈ 0.99. The dimensionality of BayesWave is ~ 90 (~ 18 wavelets) at this post-merger signal-to-noise ratio. The dimensionality of our adopted model is 15 with fitting factors of ≈ 0.92 for SLy-M1.350-Λ390. Furthermore, BayesWave can generalise to any signal (e.g. glitches). In contrast, our model has been developed to suit a post-merger gravitational-wave signal. The parameters in our model are interpretable: for example, in Fig. 3.C.1, the α_0 value for SLy-M1.350-Λ390 is $-1.60^{0.50}_{0.26}$ which shows that the frequency of the dominant gravitational-wave mode is decreasing.

The hierarchical model from Ref. [2] allows a bidirectional relationship between equal-mass progenitor neutron star properties $(C, M, \kappa_2^{\rm T})$ and numerical-relativity post-merger simulations. This is achieved by a two step process. Firstly, the progenitor properties are used to solve $\bar{C}(M, \kappa_2^{\rm T}) = C$ using a power-law relationship. Secondly, the model parameters, $\boldsymbol{\Theta}$, are determined by solving $h_c = \boldsymbol{\Theta}\,\boldsymbol{X}(\bar{C}(M, \kappa_2^{\rm T}), M, \kappa_2^{\rm T})$, where h_c is the numerical-relativity amplitude spectra for the characteristic strain ($h_c(f) = |\tilde{h}(f)|\sqrt{f}$). Here,

$\boldsymbol{X}(\bar{C}(M, \kappa_2^{\rm T}), M, \kappa_2^{\rm T})$ is a design matrix derived from the progenitor properties M and $\kappa_2^{\rm T}$.

We use the posteriors from Section 3.3 to calculate the amplitude of the characteristic spectrum $|\tilde{h}_+(\boldsymbol{\theta}, f)|\sqrt{f}$ and use the trained model, $\boldsymbol{\Theta}$, to determine the hierarchical model posteriors on $\kappa_2^{\rm T}$ and C. The cross-polarisation waveforms are discarded because the hierarchical model only uses the magnitude of the spectra, and $|\tilde{h}_+(\boldsymbol{\theta}, f)| = |\tilde{h}_\times(\boldsymbol{\theta}, f)|$. The hierarchical model, $\boldsymbol{\Theta}$, was previously trained on 35 numerical-relativity simulations from Ref. [94], a distinct set of numerical-relativity simulations to those used in this paper. Therefore, this is an out-of-sample model validation.

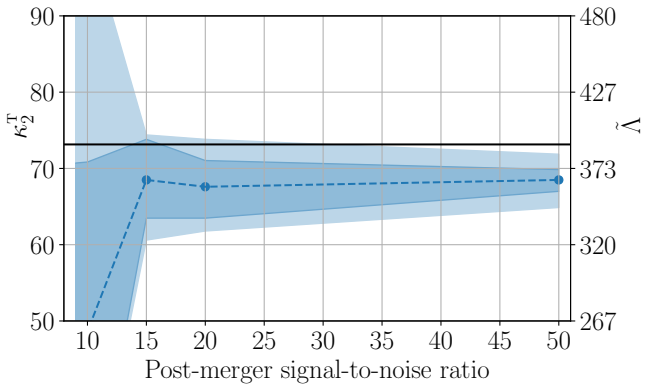

Figure 3.7: Tidal coupling constant posteriors versus post-merger signal-to-noise ratio for numerical-relativity waveform SLy-M1.350-Λ390. The tidal coupling constant is inferred from the hierarchical model [2] using the magnitude of the posterior waveforms, $|h_+(\boldsymbol{\theta}, t)|$. The 68% (dark blue) and 95% (light blue) confidence intervals are shown along with the median values (blue dots). The true value for $\kappa_2^{\rm T}$ is shown as the solid horizontal line. The corresponding tidal deformability values are shown on the secondary vertical axis.

Figure 3.7 shows the inferred posteriors for $\kappa_2^{\rm T}$ with 68% and 95% confidence intervals in dark blue and light blue respectively. The true injected value of $\kappa_2^{\rm T}$, is shown by the horizontal solid black line and the median values as blue dots. The vertical axis shows both the quadrupolar tidal coupling constant (left axis) and the quadrupolar tidal deformability (right axis). The values inferred for the tidal parameters of the progenitor neutron stars are lower than the true value of the numerical-relativity injection, though the 95% confidence interval excludes the true value only at a post-merger signal-to-noise ratio of 50. The tidal coupling constant at a post-merger signal-to-noise ratio of 15 is constrained at 95% confidence intervals to $68.5^{+5.9}_{-7.9}$, which tightens to $68.5^{+3.4}_{-3.6}$ for a post-merger signal-to-noise ratios of 50.

There are a number of factors that will impact on the performance of the hierarchical model. Firstly, the numerical-relativity spectra from Ref. [94], which were used in Ref. [2] to train the model, are a distinct set of simulations to those in use in this paper [100]. Specifically, waveform SLy-M1.350-Λ390 is available in both sets of numerical-relativity simulations (Refs. [100] and [94]), and, although the primary post-merger peak occurs at the same frequency, the spectral response for the other frequencies are different (fitting factor = 0.90). Secondly, the simulation outputs can be dependent on the spatial and temporal resolution, which can lead to waveform changes related to parameters like collapse time, primary oscillation frequency and decay time constants. To ensure the performance of the hierarchical model, the simulations used in the

training set and test set should be consistent and not contradictory. Thirdly, the hierarchical model is an approximate model, and was trained on 35 compatible waveforms; (for details, see Ref. [2]). Given the small training set, the hierarchical model results are consistent. The complexity of the model could be increased as additional consistent numerical-relativity simulations become available.

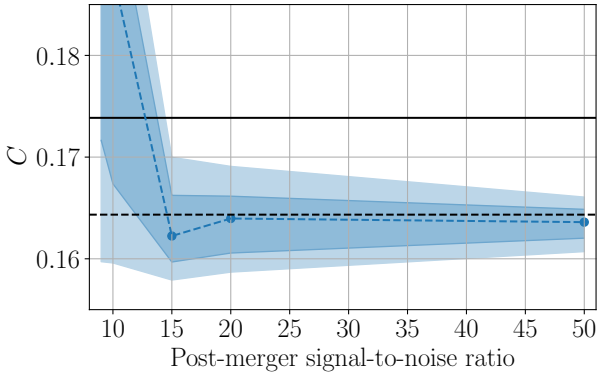

Figure 3.8: Compactness posteriors versus post-merger signal-to-noise ratio for numerical-relativity waveform SLy-M1.350-Λ390. The 68% (dark blue) and 95% (light blue) confidence regions are shown. The compactness is inferred from the hierarchical model [2]. The compactness inferred directly from the numerical-relativity waveform (dashed black line) and the compactness of the progenitor neutron stars (solid black line) are also shown. See the text for an explanation of the offset in these two values.

Hierarchical model posteriors for the compactness, C, are shown in Fig. 3.8. The 68% and 95% confidence intervals are shaded dark blue and light blue respectively, and the median values are shown with blue dots. The true value corresponding to the injected numerical-relativity simulation is shown as a horizontal solid black line. The value inferred from the numerical-relativity simulation using the hierarchical model is shown as a horizontal black dashed line. The hierarchical posteriors for C are clustered around the value inferred directly from the hierarchical model for the numerical-relativity simulation. This is expected and due to the mismatch between the numerical-relativity injection and the set of numerical-relativity simulations used to train the hierarchical model. The compactness has been constrained to $0.162^{+0.007}_{-0.004}$ at post-merger signal-to-noise ratios of 15 tightening to $0.164^{+0.002}_{-0.003}$ at signal-to-noise ratios of 50 to 95% confidence intervals. The posteriors for the compactness, C, only narrow moderately as the post-merger signal-to-noise ratio is increased.

3.6 Discussion

We use an analytical model to characterise gravitational-wave strain from nine numerical-relativity simulations selected such that the post-merger oscillations persist for ~ 25 ms. The median noise-weighted fitting factors for the posterior waveforms range between 0.92 - 0.97 for injections with post-merger signal-to-noise ratios of 50. This corresponds to a loss in detection rate of 22 - 12% when compared to a signal without mismatch. We measure the Bayes factor in favour of signal detection with numerical-relativity simulation SLy-M1.350-Λ390 and find that successful detections occur with post-merger signal-to-noise ratios of ≥ 10 with possible detections as low as post-merger signal-to-noise ratios of 7, depending on the specific noise realisation. This indicates that this model could

be used for parameter estimation and detection if a post-merger signal louder than signal-to-noise ratio of 10 was coincident with an inspiral detection. We find that this corresponds to a distance of $\sim 10\,\mathrm{Mpc}$ for an optimally oriented system using a three-detector network (LIGO Hanford, Livingston, and Virgo) at design sensitivity.

We determine that starting the model at the time of coalescence results in the maximum matched filter signal-to-noise ratio even though the fitting factors are lower in the vicinity of the merger due to the dynamics of the nascent neutron star. We find that the uncertainty in the time of coalescence for the inspiral of the progenitor neutron stars is less that 0.1 ms for a post-merger signal-to-noise ratio of ≥ 6 and show that this corresponds to a maximum matched-filter signal-to-noise ratio.

The gravitational-wave strain of the inspiral can constrain the equation of state for the cold neutron star at the high inspiral signal-to-noise ratios ($\gtrsim 200$) required for post-merger detection of the remnant (see Fig. 3.5). This can place additional constraints on the priors for the dominant post-merger frequency. However, a phase transition in the hot post-merger remnant [159, 177, 178], and uncertainty in the numerical-relativity calculations due to computational trade-offs, may result in a post-merger gravitational-wave signal that is quantitatively different than the numerical-relativity simulations. With this in mind, we assume a more general, agnostic set of priors (see Appendix 3.B).

Using numerical-relativity waveform SLy-M1.350-Λ390, selected for its compatibility with Λ values determined from GW170817 [e.g., 6, 55, 99, 158–160], we constrain the primary post-merger frequency to a range of $3310\,\mathrm{Hz}\pm^{1.4}_{1.2}\%$ for 95% confidence intervals at post-merger signal-to-noise ratios of 15. The precision increases to $3296\,\mathrm{Hz}\pm^{0.3}_{0.2}\%$ for post-merger signal-to-noise ratios of 50.

We show that our model and BayesWave similarly constrain the dominant post-merger frequency, f_{peak}, for post-merger signal-to-noise ratios of $\gtrsim 20$. For post-merger signal-to-noise ratio of $\sim 9-15$ BayesWave is better able to constrain f_{peak}. We generate fitting factors of ≈ 0.99 using BayesWave for SLy-M1.350-Λ390 at a post-merger signal-to-noise ratio of 50. The corresponding fitting factors from our model are ≈ 0.92. The dimensionality of the BayesWave posterior reconstruction is significantly larger than our analytic; ~ 90 dimensions for BayesWave cf. 15 for ours. Moreover, our adopted model is interpretable and can supply additional information about the individual modes (e.g. frequency drifts and exponential damping time constants).

We use the hierarchical model from Ref. [2], which has been trained on numerical-relativity waveforms from Ref. [94], to determine posteriors for κ_2^{T} and C. We obtain 95% confidence intervals on κ_2^{T} (and $\tilde{\Lambda}$) of $\pm^{9}_{12}\%$ at a post-merger signal-to-noise ratio of 15 with increasing precision to $\pm\,5\%$ at a post-merger signal-to-noise ratio of 50. The 95% confidence intervals on C range from $\pm^{4.3}_{2.7}\%$ at post-merger signal-to-noise ratios of 15 to $\pm^{1.5}_{1.8}\%$ at post-merger signal-to-noise ratios of 50. However, the injected value for C is outside the 95% confidence interval.

It should be noted that the inferred posteriors for C are centred around the compactness value inferred directly from the numerical-relativity simulation. This indicates that the offset in the inferred compactness values is caused by the difference in the SLy numerical-relativity simulations between Ref. [94] and Refs. [95, 96]. Contradictory training waveforms will increase uncertainties in the hierarchical model. The 35 numerical-relativity simulations used to train the

hierarchical model were homogeneous, changing only the equation of state and the progenitor masses between simulations, keeping other simulation parameters the same. It should also be emphasised that, because the numerical-relativity simulations are drawn from independent sources, the posteriors of $\kappa_2^{\rm T}(\tilde{\Lambda})$ and C are true out-of-sample estimates. We expect the estimates of C and $\kappa_2^{\rm T}$ to become more consistent with the injected value as the training set is increased in size and covers more system and progenitor properties.

In addition to the aforementioned analytical models [147, 148], other work have generated analytical post-merger gravitational-wave models. In Ref. [163], a model was generated for the time-based amplitude and phase of the complex gravitational-wave strain using a smooth piece-wise function for the amplitude. The time-based phase was fit by the combination of a polynomial and exponentially-damped sinusoid using an iterative CMA-ES (covariance matrix adaption evolution search) fitting algorithm. The maximum fitting factors were calculated in the time domain without noise weighting and are not directly comparable to the noise-weighted fitting factors calculated with Eq.(3.9). The maximum fitting factors were $\sim$0.92 - 0.98 for 95% of the 54 waveforms.

A frequency-domain model was introduced in Ref. [176] from analysing the major spectral peaks of the whitened power spectrum. The power of the dominant post-merger frequency peak was estimated by a trapezoidal structure and the model parameters were determined with a least-squares algorithm. No fitting factors were calculated in this reference, as the goal was estimating source red-shifts. This model was extended in Ref. [101] to add a Gaussian component to the fundamental post-merger frequency using a nonlinear least-squares fit. The goal of the fits in Ref. [101] were qualitative, rather than quantitative and no fitting factors were stated.

The model used in Ref. [147] consists of three exponentially damped sinusoids centred at frequencies $(f_{2-0}, f_{\rm spiral}, f_{\rm peak})$ which are described in Section 3.1. In contrast, the model introduced in Ref. [148], consists of two exponentially damped sinusoids, the first centred on f_1 which is modulated by frequency f_{1e}, and the second is centred on the dominant post-merger frequency, f_2, with a linear and quadratic frequency drift terms. This model produced fits of $\sim$ 80-94%. In Ref.[194], a frequency-domain model was developed for a single damped-sinusoid. This model was based on three or six parameters and used Bayesian inference to estimate the parameters for 120 numerical-relativity simulations. They obtained fitting factors of $\sim$0.60 - 0.98. Reference [152] parameterised the instantaneous amplitude and phase of the time-based gravitational-wave strain using 172 numerical-relativity simulations. Their model uses a rational-polynomial fit based on the progenitor properties (M_1, M_2, $\kappa_2^{\rm T}$) derived in Refs. [111, 164, 195]. They achieved fitting factors of $\sim$0.30 - 0.85 in zero noise.

The fitting factors obtained in our paper compare favourably to those listed above; our maximum fitting factors are above 0.93 for all waveforms [cf. 163] and our minimum fitting factors are above 0.90 across all waveforms [cf. 152, 194]. The fitting factor is more sensitive to deviations in the time-based phase or Fourier phase response, than it is to amplitude deviations. The fits in Ref. [152] could possibly be improved by adding in more flexibility in the phase response. Our model bypasses the phase matching difficulty by directly fitting the phase with parameters, (f_j, α_j, ψ_j), from the injected signals from all three interferometers. Although Ref. [194] does directly fit the phase, the first-order model

is too restricted to obtain higher fitting factors and better results may be obtained by increasing the order of the model. The number of numerical-relativity simulations used in Refs. [152, 163, 194] was significantly larger than the nine simulations we use here, including additional mass ratios, spin configurations and eccentricity values. We leave it for future work to expand the number of numerical-relativity simulations to test this model.

Although numerical-relativity simulations currently provide the best estimate of the post-merger gravitational-wave strain, future post-merger signals may not be consistent with these state-of-the-art simulations. With this in mind, our model matches the numerical-relativity simulations well, but it is more flexible than these simulations. This is important because this method is a middle ground between simulations of known waveforms, and more general (e.g. unmodelled excess power and BayesWave) methods. Nevertheless, numerical-relativity simulations are the primary method of investigating the dynamical physics of the post-merger region and research into these simulations is vital.

Acknowledgments

P.D.L. is supported through Australian Research Council (ARC) Future Fellowship FT160100112, ARC Discovery Project DP180103155, and ARC Centre of Excellence CE170100004. A.R.C. is supported by ARC grant DE190100656. S.G. and J.A.C. gratefully acknowledge the NSF for financial support from Grants No. PHY 1806580, PHY 1809572, and TG-PHY120016. The Flatiron Institute is supported by the Simons Foundation. This research has made use of data, software and/or web tools obtained from the Gravitational Wave Open Science Center (https://www.gw-openscience.org), a service of LIGO Laboratory, the LIGO Scientific Collaboration and the Virgo Collaboration. LIGO is funded by the U.S. National Science Foundation. Virgo is funded by the French Centre National de Recherche Scientifique (CNRS), the Italian Istituto Nazionale della Fisica Nucleare (INFN) and the Dutch Nikhef, with contributions by Polish and Hungarian institutes. The authors are grateful for computational resources provided by the LIGO Laboratory and supported by National Science Foundation Grants PHY-0757058 and PHY-0823459. This research was done using resources provided by the Open Science Grid [196, 197], which is supported by the National Science Foundation award 1148698, and the U.S. Department of Energy's Office of Science. We are grateful to Sukanta Bose for valuable comments on the manuscript.

3.A Numerical relativity simulations

We use nine simulations from the `CoRe` gravitational wave database [100] for binary neutron star mergers. The simulations are listed by their equation of state, the progenitor mass, and the quadrupolar tidal deformability. We limit our simulations to those with equal-mass prognitors for compatibility with the heirarchical model in Ref. [2]. We choose simulations with the highest resolution such that the remnant was transmitting gravitational waves for $\sim 25\,\mathrm{ms}$. In some cases increasing the resolution resulted in a reduced lifetime of the remnant. Table 3.A.1 shows the simulation designator for this paper, the name

of the waveform in the CoRe database, and the citation for the associated simulation in the metadata (if available).

Table 3.A.1: Numerical relativity simulations

Designator	Simulation name	Citations [100]
SLy-M1.350-Λ390	THC:0036:R03	[95]
LS220-M1.350-Λ684	THC:0019:R05	[97]
MS1b-M1.500-Λ864	BAM:0088:R01	-
BHBlp-M1.300-Λ1046	THC:0002:R01	[98, 99]
DD2-M1.250-Λ1295	THC:0011:R01	[98, 99]
MS1b-M1.375-Λ1389	BAM:0070:R01	[96]
MS1b-M1.350-Λ1532	BAM:0065:R03	[93]
DD2-M1.200-Λ1612	THC:0010:R01	[98, 99]
2H-M1.350-Λ2326	BAM:0002:R02	[93]

3.B Priors

The priors are listed in Eqs.(3.14-3.21) with $\mathcal{U}(a, b)$ representing a uniform prior distribution from a to b. The mode number j is limited to $\{0, 1, 2\}$ and the mode number i is restricted to $\{0, 1\}$. The priors in Eqs. 3.20-3.21 are constrained priors. These restrictions are enforced in addition to the standard priors. The prior in Eq.(3.20) ensures that the maximum spectral amplitude of each mode is decreasing. This results in f_0 converging to the loudest peak.

$$\log_{10} H \sim \mathcal{U}(-24, -19) \tag{3.14}$$
$$f_j \sim \mathcal{U}(1000, 5000) \tag{3.15}$$
$$\log_{10} T_j \sim \mathcal{U}(-4.0, 0.3) \tag{3.16}$$
$$\psi_j \sim \mathcal{U}(-\pi, \pi) \tag{3.17}$$
$$\alpha_j \sim \mathcal{U}(-6.4, 6.4) \tag{3.18}$$
$$w_i \sim \mathcal{U}(0.0, 1.0) \tag{3.19}$$
$$\log_{10}\left(\frac{\max|\tilde{h}_j(f)|_f}{\max|\tilde{h}_{j+1}(f)|_f}\right) \sim \mathcal{U}(0.0, 10.0) \tag{3.20}$$
$$w_0 + w_1 \sim \mathcal{U}(0.0, 1.0) \tag{3.21}$$

w_2 is calculated as:

$$w_2 = 1 - w_0 - w_1, \tag{3.22}$$

ensuring that $\sum_j w_j = 1$ and $w_2 \in [0, 1]$ as required.

3.C Posteriors for all numerical-relativity injections

Selected posteriors for all numerical-relativity simulations are shown in Fig. 3.C.1-3.C.9. The waveforms are injected at a post-merger signal-to-noise ratio of 50. The posteriors shown are: f_0, α_0, f_1 and α_1. The posteriors are coloured as per Fig. 3.2 and Table 3.A.1. The frequency drift term, α_0, for the dominant post-merger frequency is negative for some simulations. Most numerical-relativity simulations spectrograms show that the dominant

frequency is constant or increases slightly over time, however, many simulations do show decreasing evolution of the dominant post-merger oscillation frequency [e.g., 98, 109, 198].

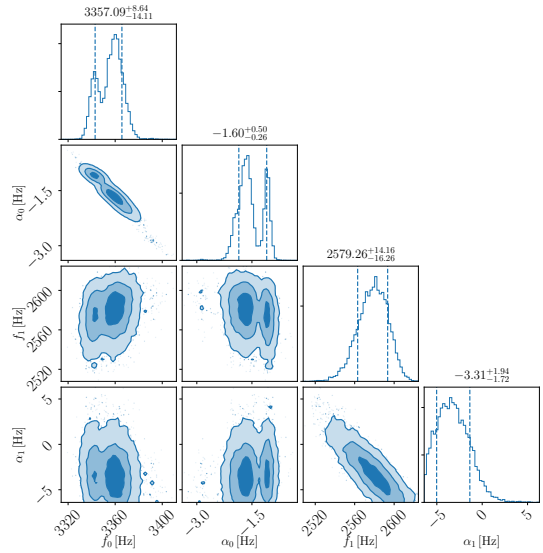

Figure 3.C.1: Selected posteriors for numerical-relativity post-merger injection using the equation of state SLy with equal mass, $1.35\,\mathrm{M}_\odot$, neutron stars (waveform SLy-M1.350-Λ390). The numerical-relativity simulation was injected at a post-merger signal-to-noise ratio of 50.

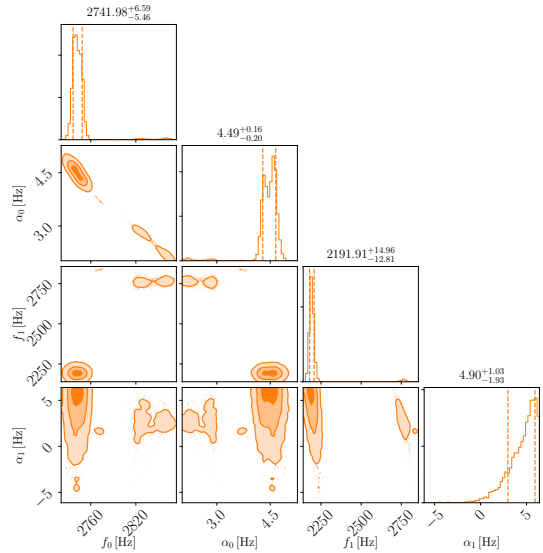

Figure 3.C.2: As per Fig. 3.C.1 using the equation of state LS220 with equal mass, $1.35\,\mathrm{M}_\odot$, neutron stars (waveform LS220-M1.350-Λ684).

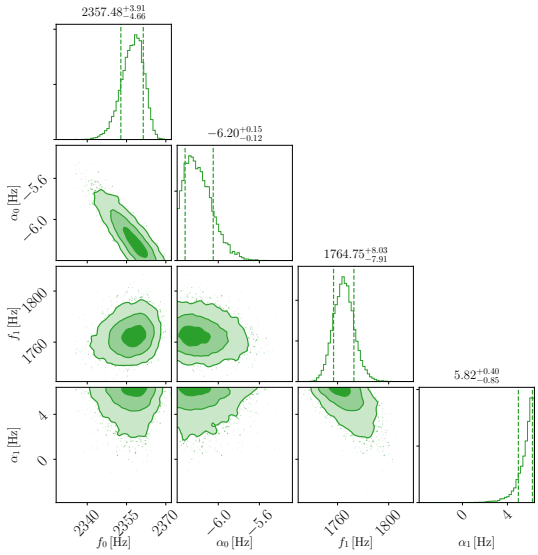

Figure 3.C.3: As per Fig. 3.C.1 using the equation of state MS1b with equal mass, 1.50 $M_\odot$, neutron stars (waveform MS1b-M1.500-Λ864).

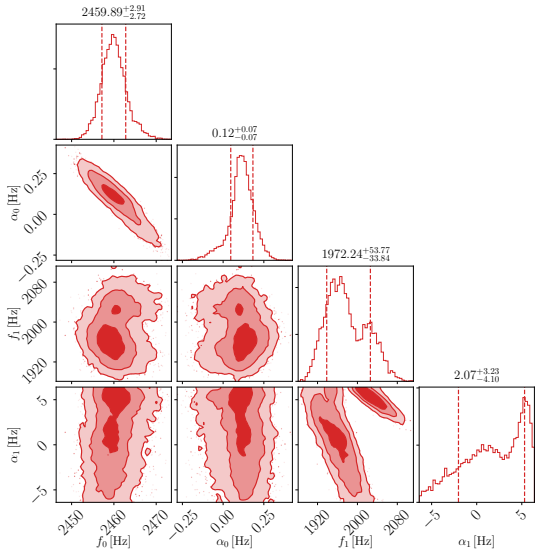

Figure 3.C.4: As per Fig. 3.C.1 using the equation of state BHBlp with equal mass, 1.30 $M_\odot$, neutron stars (waveform BHBlp-M1.300-Λ1046).

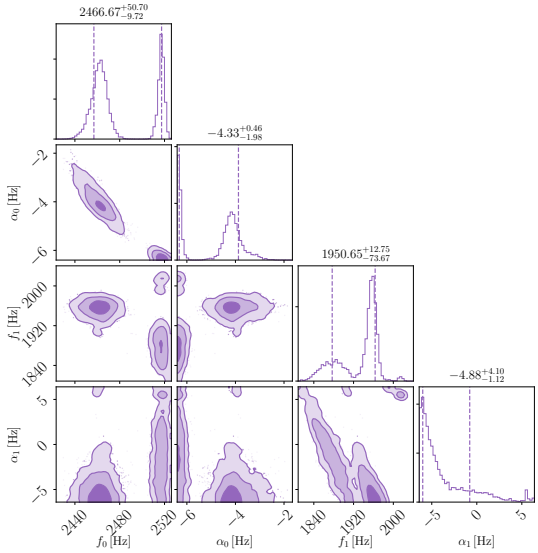

Figure 3.C.5: As per Fig. 3.C.1 using the equation of state DD2 with equal mass, 1.25 $M_\odot$, neutron stars (waveform DD2-M1.250-Λ1295).

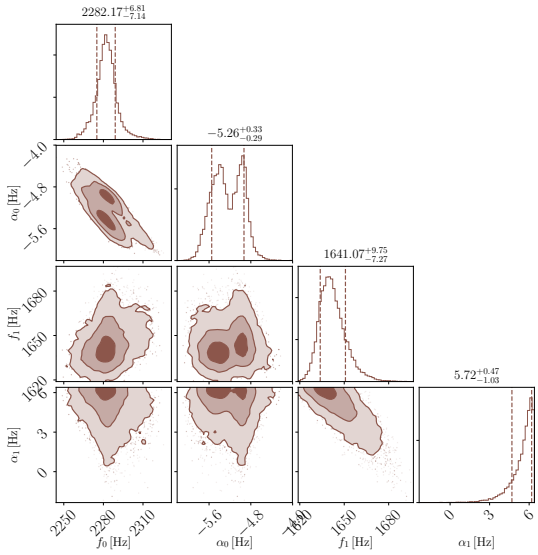

Figure 3.C.6: As per Fig. 3.C.1 using the equation of state MS1b with equal mass, 1.375 $M_\odot$, neutron stars (waveform MS1b-M1.375-Λ1389).

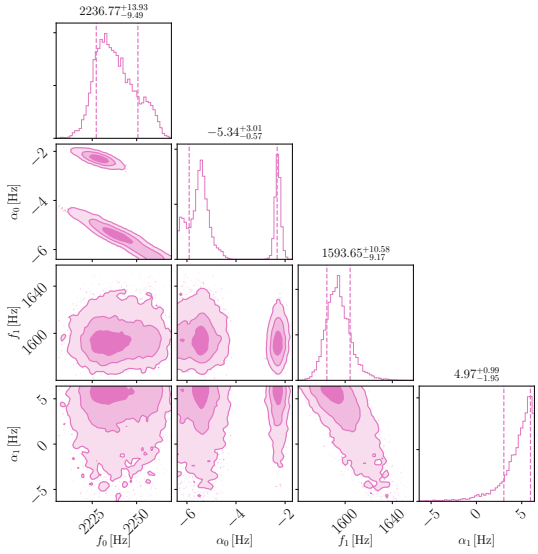

Figure 3.C.7: As per Fig. 3.C.1 using the equation of state MS1b with equal mass, 1.35 $M_\odot$, neutron stars (waveform MS1b-M1.350-Λ1532).

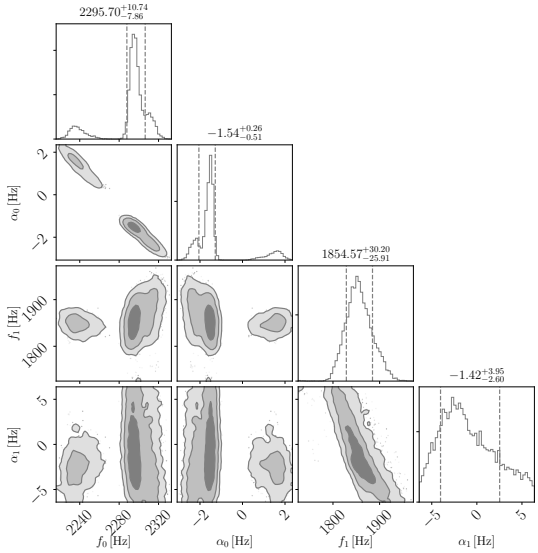

Figure 3.C.8: As per Fig. 3.C.1 using the equation of state DD2 with equal mass, 1.20 $M_\odot$, neutron stars (waveform DD2-M1.200-Λ1612).

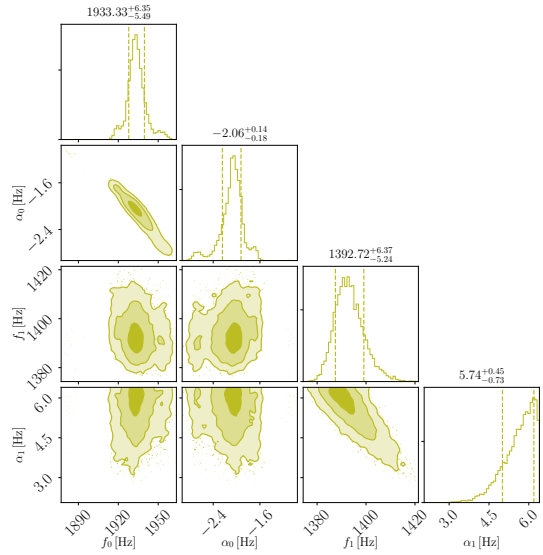

Figure 3.C.9: As per Fig. 3.C.1 using the equation of state 2H with equal mass, $1.35\,\mathrm{M}_\odot$, neutron stars (waveform 2H-M1.350-Λ2326).

Chapter 4

Can we measure the collapse time of a post-merger remnant for a future GW170817-like event?

Paul J. Easter
Paul D. Lasky
Andrew R. Casey

Abstract

Measuring the collapse time of a binary neutron star merger remnant can inform the physics of extreme matter and improve modelling of short gamma-ray bursts and associated kilonova. The lifetime of the post-merger remnant directly impacts the mechanisms available for the jet launch of short gamma-ray bursts. We develop and test a method to measure the collapse time of post-merger remnants. We show that for a GW170817-like event at $\sim 40\,\mathrm{Mpc}$, a network of Einstein Telescope with Cosmic Explorer is required to detect collapse times of $\sim 10\,\mathrm{ms}$. For a two-detector network at A+ design sensitivity, post-merger remnants with collapse times of $\sim 10\,\mathrm{ms}$ must be $\lesssim 10\,\mathrm{Mpc}$ to be measureable. This increases to $\sim$18-26 Mpc if we include the proposed Neutron star Extreme Matter Observatory (NEMO), increasing the effective volume by a factor of $\sim$30.

4.1 Introduction

Measuring the lifetimes of binary neutron star post-merger remnants can help probe extreme matter at high temperature and densities and narrow down the physics of short gamma-ray bursts [e.g., 199, 200]. These remnants may promptly collapse into a black hole or form a hot, differentially-rotating neutron star. If the total mass of a remnant is between 1.2 and 1.5 times the maximum non-rotating neutron star mass (the Tolman-Oppenheimer-Volkov mass), then the remnant is known as a hypermassive neutron star [44, 45, 123, 124, 179], which is expected to collapse to form a black hole in a timescale from milliseconds to seconds [40]. For smaller masses, the differentially-rotating remnant will evolve into rigidly-rotating neutron star after the differential rotation is quenched. The rigidly-rotating remnant will either collapse to a black hole, or form a stable neutron star, depending on the remnant mass. See Ref. [201] for a recent review on the evolution of neutron star merger remnants.

Determining the collapse times of hypermassive remnants can help narrow down the nature of the central engine for short gamma-ray-bursts. Multi-messenger observations of binary neutron star merger GW170817 suggest that the remnant may have either collapsed to a black hole [e.g., 56–58], or formed a long-lived remnant [e.g., 59]. Measuring the collapse time of a remnant may help

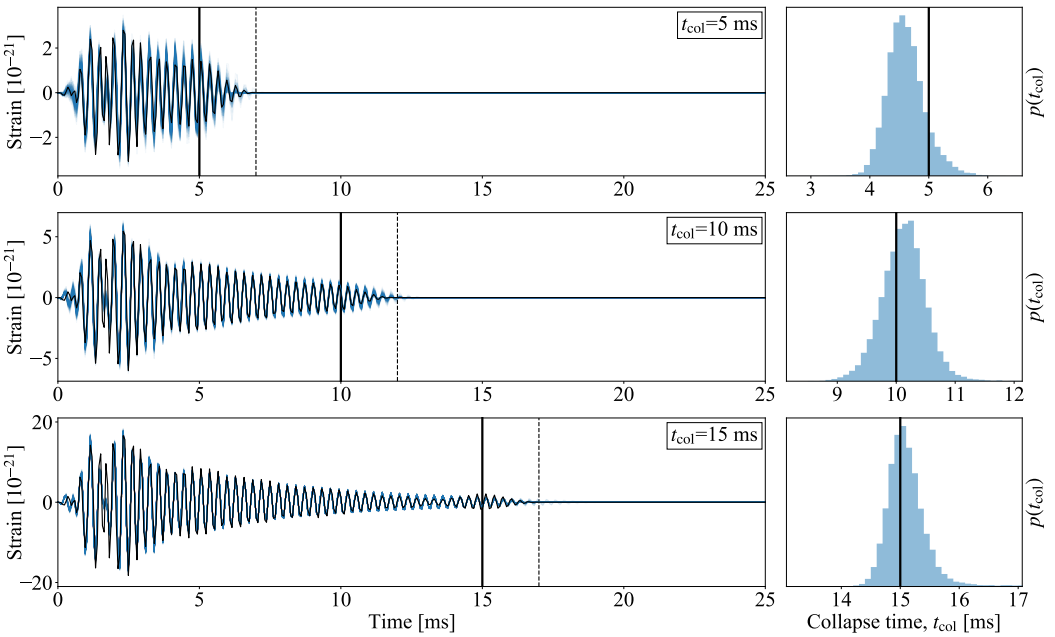

Figure 4.1: Time domain posterior waveforms for SLy equation of state with equal-mass 1.35$M_\odot$ progenitor (left panels) and measured collapse times (right panels) for injections with collapse times $t_{\rm col} = 5\,$ms (top), $t_{\rm col} = 10\,$ms (centre), and $t_{\rm col} = 15\,$ms (bottom) injected into 2A+ detector network. Left panels show the numerical-relativity injections that have been forced to collapse (black curves) with the posterior waveforms (shaded blue curves). The right panels show the collapse-time posterior distributions for each numerical-relativity injection. The solid vertical lines on all panels shows $t_{\rm col}$ for the injected waveform. The dashed vertical lines shows $t_{\rm col} + t_{\rm w}$ where the injected signal drops to zero due to the induced collapse. Here we show three loud injections from our injection study where $t_{\rm col}$ are clearly recovered. The injected distances are 5.93 Mpc, 3.04 Mpc, and 1.00 Mpc, for 5 ms, 10 ms, and 15 ms respectively. The full posteriors for the $t_{\rm col} = 10\,$ms collapse time injection are shown in the appendix (Fig 4.B.1).

determine the characteristic timescales associated with short gamma-ray-bursts, aiding the selection of the central engine (for a review see [199]). Furthermore, measuring the collapse time of the post-merger remnant may help constrain the quenching mechanism and physics of the differential rotation, which may reveal indicators towards the relative contribution of radiative (gravitational waves and neutrino) and dissipative (viscous, resistive and magnetic braking) processes within the remnant.

The direct detection of gravitational waves from future neutron star merger remnants presents a great opportunity to constrain the collapse time. Numerical-relativity simulations of merger remnants show gravitational waves predominantly emitted from the fundamental f-mode oscillation of the remnant [141, 142]. Gravitational waves emitted from this mode occur at $\sim$ 1.8-4 kHz [101, 164]. No post-merger remnant was detected for GW170817 by the LIGO and Virgo collaboration due to lack of sensitivity of the detectors at these frequencies. However, increased sensitivity of gravitational-wave instruments and targeted high-frequency detectors may enable future detections of post-merger remnants [e.g., 31, 190].

In this paper, we assess how well future networks of gravitational-wave detectors can measure the collapse time of a post-merger remnant. We extend a waveform model developed in Ref. [3] which was derived from Refs. [147, 148], to allow the measurement of the collapse time of the post-merger remnant. Using Bayesian inference, we inject numerical-relativity gravitational waveforms that are forced to collapse into different interferometer configurations to measure the maximum distance at which we can recover the collapse time.

This paper is laid out as follows. In Section 4.2 we outline the extended waveform model along with the method of gravitational-wave injections. The results are outlined in Section 4.3 and their implications in Section 4.4.

4.2 Methodology

We use numerical-relativity waveforms with two different equations of state that we inject into Gaussian noise realisations determined by the gravitational-wave interferometer configuration. We modify the numerical-relativity waveforms to collapse at a given collapse time. We then use an analytic model to perform detection and parameter estimation to determine distributions of the model parameters. This model, based on two models in Refs. [147, 148], is outlined in Ref. [3]. See also Refs. [152, 194] for alternative models of the post-merger gravitational-wave strain.

The gravitational waves from the post-merger remnant are modelled as a third-order, exponentially-damped sinusoid with a linear frequency-drift term. The plus polarisation of the gravitational-wave strain, $h_+(\boldsymbol{\theta}, t)$, is given by:

$$\begin{aligned} h_+(\boldsymbol{\theta}, t) &= \sum_j h_{j,+}(\boldsymbol{\theta}, t), \\ h_{j,+}(\boldsymbol{\theta}, t) &= H w_j \exp\left[-\frac{t}{T_j}\right] \cos\left(2\pi f_j t \left[1 + \alpha_j t\right] + \psi_j\right), \\ \boldsymbol{\theta} &= \{H, w_j, T_j, f_j, \alpha_j, \psi_j : j \in [0, 2]\}, \end{aligned} \tag{4.1}$$

where $\boldsymbol{\theta}$ are the model parameters and $\sum_j w_j = 1$. Here, H is an overall amplitude scaling factor, w_j is the relative amplitude of the jth mode, T_j is the corresponding exponential damping time constant, and f_j is the corresponding frequency. The linear frequency-drift term is α_j and the initial phase is ψ_j. The time, t, is defined, such that $\max\left[h_+^2(\boldsymbol{\theta}, t) + h_\times^2(\boldsymbol{\theta}, t)\right]$ occurs when $t = 0$. The cross polarisation for Eq.(4.1) is found by applying a $\pi/2$ phase shift to ψ_j. More details on this model can be found in Ref. [3].

We extend this model by introducing a collapse in the gravitational-wave strain using the falling edge of a Tukey window. The falling edge starts at the collapse time, $t_{\rm col}$, and by the time $t = t_{\rm col} + t_{\rm w}$ the gravitational-wave strain drops to zero (see Fig. 4.1). Here $t_{\rm w}$ is the time taken for the gravitational-wave signal to completely decay. We have chosen $t_{\rm w} = 2\,{\rm ms}$ from examining numerical-relativity simulations with collapsing remnants (e.g., simulation labels: `BAM:0109:R01`, `BAM:0110:R01`, `BAM:0111:R02` [100], `BAM:0044:R02`, `BAM:0045:R01` [150], `BAM:0124:R01` [96]). This model captures the reduction in amplitude of the post-merger gravitational-wave signal as the remnant collapses. The full gravitational-wave strain including the collapse of the remnant,

$h_{\varphi,\mathrm{c}}(\tilde{\boldsymbol{\theta}}, t)$, is given by:

$$h_{\varphi,\mathrm{c}}(\tilde{\boldsymbol{\theta}}, t) = h_{\varphi}(\boldsymbol{\theta}, t)\mathcal{T}\left(t, t_{\mathrm{col}}, t_{\mathrm{w}}\right), \tag{4.2}$$

$$\mathcal{T}(t, t_{\mathrm{col}}, t_{\mathrm{w}}) = \begin{cases} 1 & \text{if } t \leqslant t_{\mathrm{col}} \\ \frac{1}{2}\left(\cos\left(\frac{\pi(t-t_{\mathrm{col}})}{t_{\mathrm{w}}}\right)+1\right) & \text{if } t_{\mathrm{col}} < t \leqslant t_{\mathrm{col}} + t_{\mathrm{w}} \\ 0 & \text{if } t > t_{\mathrm{col}} + t_{\mathrm{w}} \end{cases}. \tag{4.3}$$

Here, $\varphi \in \{+, \times\}$ are the plus and cross gravitational-wave polarisations, and $\tilde{\boldsymbol{\theta}} = \boldsymbol{\theta} \cup \{t_{\mathrm{col}}, t_{\mathrm{w}}\}$.

To generate the collapsing gravitational-wave signal injection, $s_{\varphi,\mathrm{c}}(t)$, we apply the Tukey collapse window to the numerical-relativity simulation, $h_{\mathrm{NR},\varphi}(t)$, as follows:

$$s_{\varphi,\mathrm{c}}(t) = h_{\mathrm{NR},\varphi}(t)\mathcal{T}\left(t, t_{\mathrm{col}}, t_{\mathrm{w}}\right). \tag{4.4}$$

To ensure that $s_{\varphi,\mathrm{c}}(t)$ has the required collapse time, $h_{\mathrm{NR},\varphi}(t)$ must emit post-merger gravitational waves for $t > t_{\mathrm{col}} + t_{\mathrm{w}}$. In this paper we use two numerical-relativity simulations of binary neutron star mergers with equal-mass $1.35\,\mathrm{M}_{\odot}$ progenitors that emit gravitational waves for $\sim$ 25 ms and sample collapse times of 5, 10, and 15 ms. The two simulations use the SLy equation of state [202] (simulation label `THC:0036:R03` from Refs. [95, 100]) and LS220 equation of state [203] (simulation label `THC:0019:R05` from Refs. [97, 100]). The dimensionless tidal-deformabilities of the progenitor neutron stars for the two simulations are 390 and 684 respectively, which are consistent with tidal deformabilities inferred from GW170817 [55]. The SLy equation of state is the softer of the two equations of state, with a lower tidal deformability, more compact remnant structure, and higher dominant oscillation frequency.

We use four different detector networks in this injection study. Firstly, a two detector network at A+ design sensitivity (2A+) located at existing LIGO sites: Hanford, Washington; and Livingston, Louisiana [204, 205]. Secondly, we add the proposed Neutron star Extreme Matter Observatory (NEMO), located at Gingin, Western Australia to the first network [31]. Thirdly, we use the Einstein Telescope (ET) [33, 206–208]. And finally, the Einstein Telescope with an additional interferometer, located at Hanford, Washington, with a Cosmic Explorer (CE) power spectral density [32, 209, 210]. We use fixed random seeds for Gaussian noise generation for each interferometer and inject numerical-relativity simulations at a sky position corresponding to a mean sky signal-to-noise ratio.

We use Bilby, a Bayesian inference package [1], to obtain posteriors, $p(\tilde{\boldsymbol{\theta}} \mid s_{\varphi,\mathrm{c}}(t))$ from a numerical relativity injection with enforced collapse starting at $t = t_{\mathrm{col}}$ with width $t_{\mathrm{w}} = 2\,\mathrm{ms}$. Posteriors are calculated using waveforms detailed in Eqs.(4.1-4.3). See Ref. [3] for further details of the gravitational-wave likelihood, and Appendix 4.A for additional information on the priors.

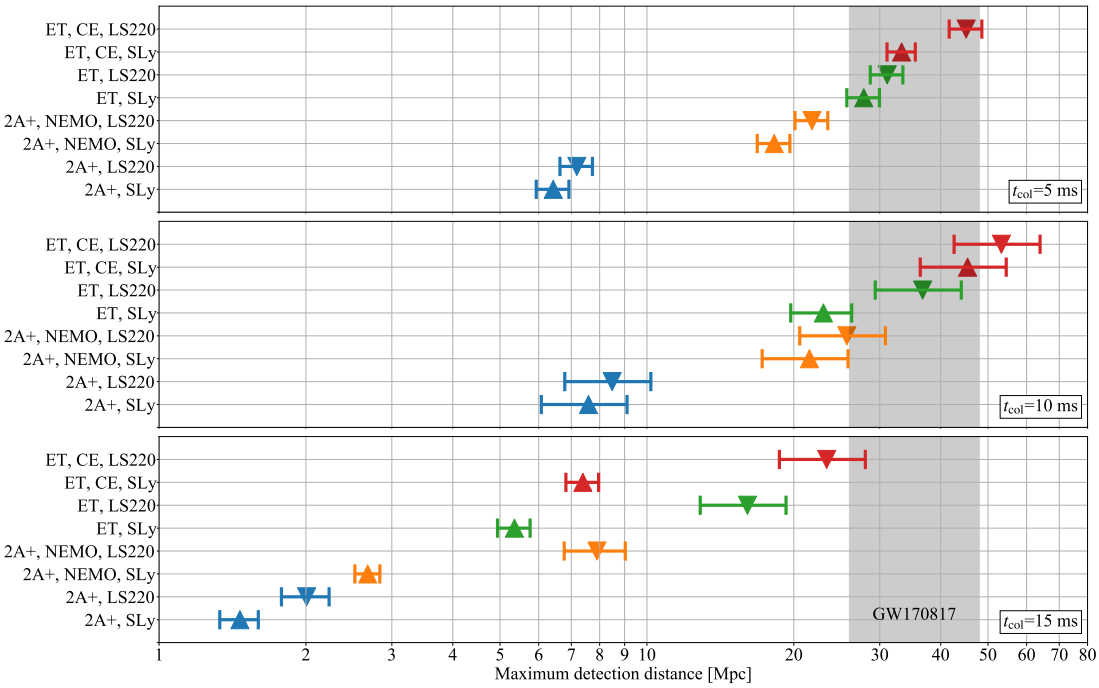

Figure 4.2: Maximum distances for which the collapse time can be measured for different interferometer networks and equations of state. The vertical axis shows different equations of state and interferometer configurations, and the maximum detection distance is shown on the horizontal axis. The numerical-relativity simulations are injected with equations of state SLy (upward pointing triangle) and LS220 (downward pointing triangle). The interferometer configurations are 2A+ (blue), 2A+ with the proposed Neutron star Extreme Matter Observatory (orange), Einstein Telescope (green), and Einstein Telescope with Cosmic Explorer (red). The top panel shows collapse times of 5 ms, the centre panel 10 ms and the lower panel 15 ms collapse times. The luminosity distance for GW170817 (gravitational-wave only) is shown in shaded grey for comparison [14].

To deem the collapse time as successfully recovered, we demand the following to hold:

$$t_{\mathrm{col},-1\sigma} - 2\,\mathrm{ms} \leqslant t_{\mathrm{col}} \leqslant t_{\mathrm{col},+1\sigma} + 2\,\mathrm{ms}, \tag{4.5}$$

$$t_{\mathrm{col},+1\sigma} - t_{\mathrm{col},-1\sigma} \leqslant 5\,\mathrm{ms}, \tag{4.6}$$

where t_{col} is the injected value. Here $t_{\mathrm{col},+1\sigma}$ and $t_{\mathrm{col},-1\sigma}$ are the upper and lower 68 percentile credible intervals on the posterior, $p(t_{\mathrm{col}})$. Finally, the Bayes Factor for the ratio of evidence for signal against evidence for noise must be $\gg 1$. The minimum successful Bayes Factor in favour of a signal over noise in this paper is ~ 500. These requirements ensure that successfully recovered t_{col} are within a few milliseconds of the injected values. Although this method is somewhat arbitrary, it successfully identifies injections where the collapse time is recovered. Furthermore, as the results are pessimistic, with detections not expected until Cosmic Explorer and Einstein Telescope are online, changing this selection criterion will not substantially change these results.

We perform numerical-relativity injections with the full waveform, Eq.(4.4), at a grid of distances and apply the above rules to determine whether we successfully recover t_{col}.

4.3 Results

We inject post-merger numerical-relativity waveforms modified to collapse at $t = t_{\rm col}$ and sample posteriors for $\tilde{\boldsymbol{\theta}}$. We then calculate posterior waveforms, $h_{\varphi,c}(\tilde{\boldsymbol{\theta}}, t)$, from Eqs.(4.2-4.3). Fig. 4.1 shows example posterior waveforms for the plus polarisation (left panels) and collapse-time posterior distributions (right panels) for numerical-relativity injections using an SLy equation of state with equal-mass $1.35\,{\rm M}_\odot$ progenitor neutron stars. The three panels have $t_{\rm col} = 5\,{\rm ms}$ (upper panels), $t_{\rm col} = 10\,{\rm ms}$ (centre panels), and $t_{\rm col} = 15\,{\rm ms}$ (lower panels). The left panels show the numerical-relativity injection (plus polarisation) in black and the posterior waveforms in blue. The vertical black lines show the beginning, $t = t_{\rm col}$ (solid), and the end, $t = t_{\rm col} + t_{\rm w}$ (dashed), of the collapse for the injected signal. We perform injections into the 2A+ detector network at a grid of distances and from these injections we select three distances where we can clearly recover the collapse time (see Sec. 4.2). The injection distances are 5.93 Mpc for 5 ms, 3.04 Mpc for 10 ms, and 1.00 Mpc for 15 ms. The right panels show posteriors, $p(t_{\rm col})$, in shaded blue, along with the true injected value, $t_{\rm col}$, as solid vertical black lines. The model successfully recovers both the collapse time and the complex nature of the numerical-relativity injection, for all three injections. For reference, the full posteriors for $t_{\rm col} = 10\,{\rm ms}$ are shown in the appendix (Fig. 4.B.1).

In Fig. 4.2, we show the maximum distance for which we can recover the collapse time for the post-merger remnant. The numerical-relativity injections are performed for SLy (upward triangles) and LS220 (downward triangles) equations of state. We inject into the following interferometers described in Sec. 4.2: 1) 2A+ (blue), 2) 2A+ and the proposed NEMO (orange), 3) Einstein Telescope (green), and 4) Einstein Telescope with Cosmic Explorer (red). We calculate the signal-to-noise ratio at a fixed distance over the entire sky for each detector network. We then choose a sky position with a signal-to-noise ratio close to the mean all-sky signal-to-noise ratio, and perform all injections at this sky position for this detector network. The lower error bars show the largest distance where the collapse times are recovered, the upper error bars show the smallest distance where the collapse time recoveries fail, and the marker is placed in the midpoint between these distances. If a post-merger collapse event occurs at a sky location near the antenna pattern maximum then the maximum distance where we can measure $t_{\rm col}$ will increase by a factor of ~ 0.6.

Detecting the collapse time of a GW170817-like event at a luminosity distance of 40^{+8}_{-14} Mpc [14] (Fig. 4.2, shaded region, gravitational wave only) would require the combination of ET with CE for $t_{\rm col} \sim 10\,{\rm ms}$, or ET with $t_{\rm col} \sim 5\,{\rm ms}$. The detection distance for 2A+ with $t_{\rm col} \sim 10\,{\rm ms}$ is $\sim$ 6-8 Mpc. This reduces to $\sim$ 1.5-2.0 Mpc for $t_{\rm col} \sim 15\,{\rm ms}$. Adding the NEMO high frequency detector increases the detection distance to $\sim$ 17-31 Mpc for $t_{\rm col} \sim 10\,{\rm ms}$. The detection distances for $t_{\rm col} \sim 15\,{\rm ms}$ with 2A+ and NEMO interferometers are $\sim 3\,{\rm Mpc}$ and $\sim 8\,{\rm Mpc}$, for SLy and LS220 injections, respectively.

For most collapse times and interferometer configurations, the ratio of the detection distance for LS220 to SLy injections is around $\sim 1.2 \approx f_0({\rm SLy})/f_0({\rm LS220})$ (f_0 is the dominant post-merger oscillation frequency) which is consistent with SLy being softer and more compact than the LS220 equation of state. For $t_{\rm col} \sim 15\,{\rm ms}$ injections into either 2A+ with NEMO, ET, or ET with CE, interferometer networks, the ratio of the LS220 to SLy detection distance

increases to ~ 3. Specifically, for $t_{\rm col} \sim 15\,{\rm ms}$ injections, detection distances of $\sim 8, 16, 23\,{\rm Mpc}$ are found for LS220 equation of state with interferometers 2A+ with NEMO, ET, and, ET with CE, respectively. The corresponding detection distances for SLy injections are $\sim 3, 5, 7\,{\rm Mpc}$.

For injections where we can recover the collapse time, the dominant post-merger frequency is well constrained at $f_0 \lesssim 2\%$, $f_0 \lesssim 1\%$, and $f_0 \lesssim 0.2\%$ for injections of $t_{\rm col} = 5\,{\rm ms}$, $t_{\rm col} = 10\,{\rm ms}$ and $t_{\rm col} = 15\,{\rm ms}$, respectively. Finally, we find no significant correlations between $t_{\rm col}$ and other model parameters. We also attempt to measure the maximum detection distance where we can recover $t_{\rm col} = 20\,{\rm ms}$ and find that limitations in the third-order exponentially-damped sinusoidal model, Eq.(4.1), prevent recovery of such collapse times. For $t_{\rm col} > 15\,{\rm ms}$ signals, the analytical model cannot successfully track the time-domain phase of the gravitational-wave strain. This limitation could be overcome by increasing the complexity of the frequency evolution in Eq.(4.1), possibly introducing a quadratic frequency evolution term [148]. Additionally, unmodelled searches such as BayesWave could be modified to measure the collapse time of the remnant [170, 191–193].

4.4 Discussion

We inject post-merger gravitational-wave signals that have been modified to collapse at varying distances into four different interferometer configurations: 2A+, 2A+ with NEMO, ET and ET with CE. We perform injections with collapse times of 5, 10, and 15 ms, and recover collapse-time posteriors. The injected gravitational-wave strain is recovered with a third-order exponentially damped sinusoid with a linear frequency-drift term [3] that has been modified to collapse at $t = t_{\rm col}$.

To measure the collapse time of a post-merger remnant in a GW170817-like event (gravitational-wave only, luminosity distance of $40^{+8}_{-14}\,{\rm Mpc}$ [14]), we find that we need interferometer configurations of either ET, or ET with CE, for $t_{\rm col} \sim 10\,{\rm ms}$ with the exclusion of ET with SLy equation of state.

We show that, for each detector network, the maximum detection distance where we can measure 5 ms collapse times is similar to the maximum detection distance for 10 ms collapse times, with maximum detection distances of: $\sim$ 6-8 Mpc for 2A+, $\sim$18-26 Mpc for 2A+ with NEMO, $\sim$23-37 Mpc for ET, and $\sim$33-53 Mpc for ET with CE.

We find that the stiffer equation of state, LS220, has more energy in the post-merger gravitational wave at larger times after the merger. This leads to larger maximum detection distances for LS220 equations of state relative to SLy injections for $t_{\rm col} \sim 15\,{\rm ms}$. The maximum detection distance for each detector network for $t_{\rm col} \sim 15\,{\rm ms}$ are $\sim 1.5, 2.7, 5.4, 7.4\,{\rm Mpc}$ for SLy injections, and $\sim 2.0, 8.0, 16, 23\,{\rm Mpc}$ for LS220 injections, for 2A+, 2A+ with NEMO, ET, and ET with CE, detectors respectively. The above distances assume an injection at a sky position corresponding to an average signal-to-noise ratio over the entire sky. The detection distance would increase by a factor of ~ 0.6 near an optimal sky position.

We find that there are three predominant regions for detecting the collapse time. The first region, with small collapse times, is mainly limited by the Bayes Factor for the ratio of post-merger signal to noise. For large collapse times, waveform systematics limit detections, specifically the inability of the model to

track the phase of the gravitational-wave strain. Between these two regions the signal-to-noise ratio is the limiting factor.

Ignoring waveform systematics, Ref. [211] found that they could achieve a signal-to-noise ratio of 0.5-8.6 for a collapse time of 10 ms for a post-merger gravitational-wave signal at 50 Mpc. The model used was a single-order damped sinusoid injected into a high-frequency detector. The authors used a TM1 equation of state with two equal-mass $1.35\,\mathrm{M}_\odot$ progenitors with a dominant post-merger frequency of $\approx 2.8\,\mathrm{kHz}$ which very similar to f_0 for the LS220 equation of state in this paper. We find in this paper that we require a post-merger signal-to-noise ratio of $\gtrsim 17$ to successfully recover $t_{\rm col} \sim 10\,\mathrm{ms}$ for LS220 equation of state when waveform systematics are considered.

With an estimated binary neutron star merger rate of $320^{+490}_{-240}\,\mathrm{Gpc}^{-3}\mathrm{yr}^{-1}$ [29], it is unlikely that the collapse time of a post-merger remnant will be detected before either Cosmic Explorer or Einstein Telescope are operating at design sensitivity. When Cosmic Explorer and Einstein Telescope are both operating we may detect post-merger collapse times of $\sim 10\,\mathrm{ms}$. If only Einstein Telescope is fully operating then we may potentially measure post-merger collapse times of $\sim 10\,\mathrm{ms}$ except for soft equations of state like SLy. In the mean time we will need to rely on indirect estimates of the post-merger collapse time that depend on multi-messenger observations [e.g., 56–59]. However, if a GW170817-like event occurred near an optimal sky position there would be a 60% increase in the detection distance. In this case $t_{\rm col} \sim 10\,\mathrm{ms}$ may be detectable for ET, and ET with CE, for both equations of state. Additionally, 2A+ with NEMO would also be detectable for $t_{\rm col} \sim 10\,\mathrm{ms}$ in this situation. It may also be possible to detune the proposed NEMO high frequency detector to increase sensitivity in the post-merger frequency band. This could potentially increase the sensitivity of the NEMO detector by a factor of ~ 1.6 which would be enough to allow the NEMO detector with 2A+ to detect a GW170817-like post-merger collapse for $t_{\rm col} \sim 10\,\mathrm{ms}$.

Finally, these results are dependent on the decay characteristics of the numerical-relativity simulations used in this paper. If the amplitude of future post-merger gravitational-waves have significantly longer decay timescales than the numerical-relativity simulations used here, then it is conceivable that larger collapse times could be measured. However, in this case waveform systematics become more important and models will either need to successfully track the waveform phase, or rely on incoherent methods that are independent of the phase of the gravitational-wave strain, or use unmodelled coherent detection methods [e.g., 161, 162].

4.5 Acknowledgments

P. D. L. is supported through Australian Research Council (ARC) Future Fellowship FT160100112, ARC Discovery Project DP180103155 and ARC Centre of Excellence CE170100004. A. R. C. is supported in part by the Australian Research Council through a Discovery Early Career Researcher Award (DE190100656). Parts of this research were supported by the Australian Research Council Centre of Excellence for All Sky Astrophysics in 3 Dimensions (ASTRO 3D), through project number CE170100013. Parts of this work were performed on the OzSTAR national facility at Swinburne University of

Technology. The OzSTAR program receives funding in part from the Astronomy National Collaborative Research Infrastructure Strategy (NCRIS) allocation provided by the Australian Government. The authors wish to acknowledge the public release of the Computational Relativity data at `http://www.computational-relativity.org`. We are grateful to Tim Dietrich for valuable comments on this manuscript.

4.A Priors

The priors are listed in Eqs.(4.7-4.17) with $\mathcal{U}(a,b)$ representing a uniform prior distribution from a to b. The mode number j is limited to $\{0,1,2\}$. The priors in Eqs. 4.15-4.17 are constraining priors. These restrictions are enforced in addition to the standard priors. The priors in Eqs. 4.15-4.16 sort the maximum spectral amplitude of each mode which improves computational stability and mode identification. See Ref. [3] for more details on mode sorting. We find that correlations between $t_{\rm col}$, $t_{\rm w}$, and T_0 (the exponential decay time-constant for mode zero) make it very difficult to recover all three parameters simultaneously, even with analytic injections into zero noise. Fixing $t_{\rm w} = 2\,$ms allows recovery of all other parameters in both analytical injections with zero noise, and numerical-relativity injections with Gaussian noise.

$$\begin{aligned}
\log_{10} H &\sim \mathcal{U}(-24,-17) && (4.7)\\
f_j &\sim \mathcal{U}(1000,5000)\ [\mathrm{Hz}] && (4.8)\\
t_{\rm col} &\sim \mathcal{U}(0,100)\ [\mathrm{ms}] && (4.9)\\
t_{\rm w} &= 2\ [\mathrm{ms}] && (4.10)\\
T_j &\sim \mathcal{U}(0,100)\ [\mathrm{ms}] && (4.11)\\
\psi_j &\sim \mathcal{U}(-\pi,\pi) && (4.12)\\
\alpha_j &\sim \mathcal{U}(-6.4,6.4)\ [\mathrm{Hz}] && (4.13)\\
w_0, w_1 &\sim \mathcal{U}(0,1) && (4.14)\\
f_j &> f_{j+1} && (4.15)\\
\max|\tilde{h}_j(f)|_f &> \max|\tilde{h}_{j+1}(f)|_f && (4.16)\\
w_0 + w_1 &< 1 && (4.17)\\
w_2 &= 1 - w_0 - w_1 && (4.18)
\end{aligned}$$

4.B Example posteriors

Figure 4.B.1 shows the posteriors for a post-merger numerical-relativity injection with $t_{\rm col} = 10\,{\rm ms}$ and SLy equation of state with equal-mass $1.35\,{\rm M}_\odot$ neutron stars. The injections are performed at a distance of 3.04 Mpc into a detector network of 2A+. These posteriors correspond to the $t_{\rm col} = 10\,{\rm ms}$ time-domain signal and $p(t_{\rm col})$ in Fig. 4.1. Orange lines on the bottom panels show the injected $t_{\rm col}$. The recovered collapse time is $t_{\rm col} = 10.1^{+0.3}_{-0.4}\,{\rm ms}$. The primary post-merger oscillation frequency is $f_0 = 3317 \pm 11\,{\rm Hz}$ with an exponential decay time-constant of $T_0 = 6.2^{+0.7}_{-0.6}\,{\rm ms}$. The linear frequency-drift term for the fundamental frequency is $\alpha_0 = -0.79 \pm 0.31\,{\rm Hz}$. The frequencies corresponding to the sub-dominant modes are $f_1 = 2880^{+65}_{-56}\,{\rm Hz}$ and $f_2 = 2488^{+32}_{-35}\,{\rm Hz}$.

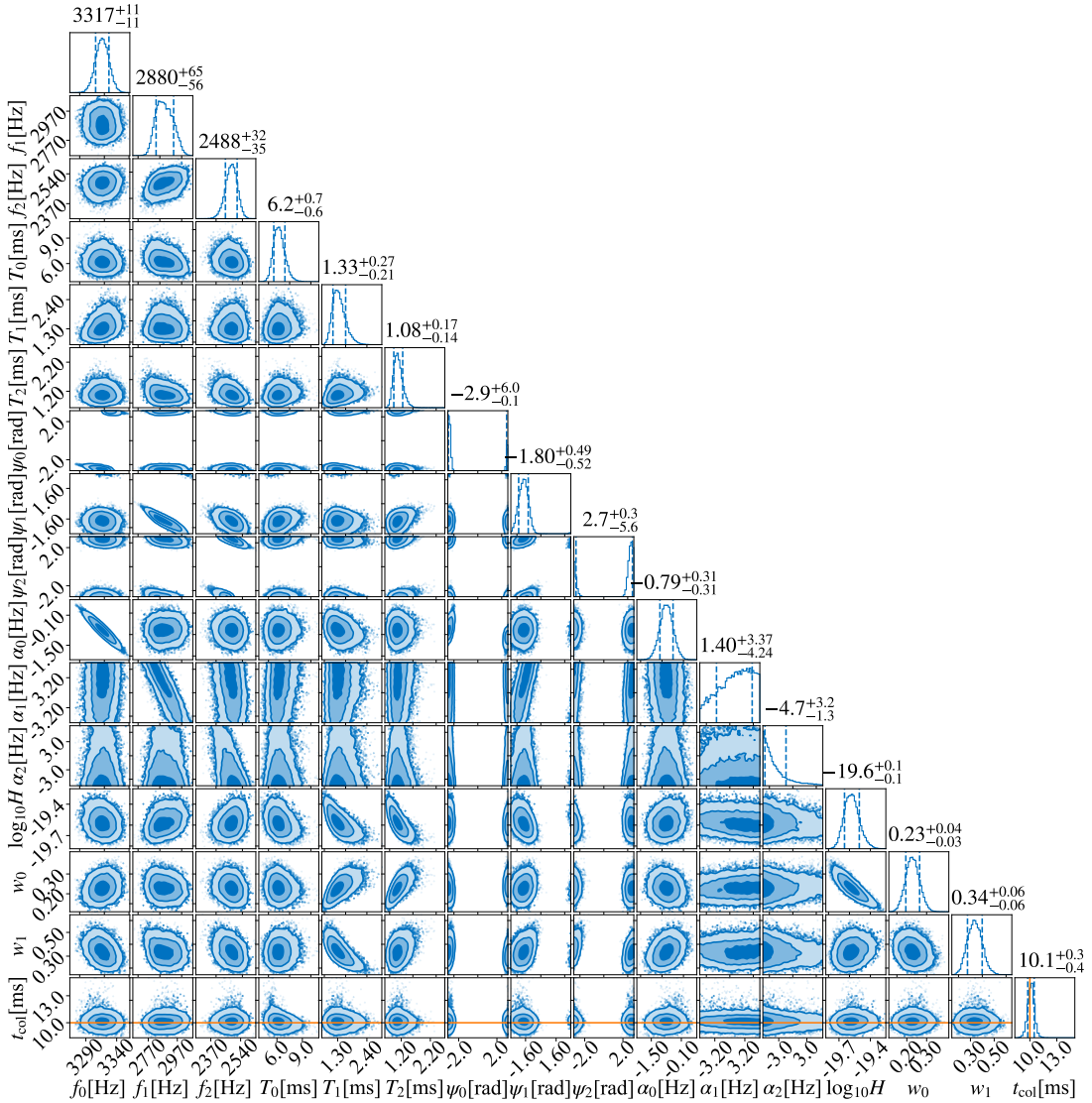

Figure 4.B.1: Full posteriors corresponding to the $t_{\rm col} = 10\,{\rm ms}$ injection shown in Fig. 4.1. The numerical-relativity simulation is injected into a 2A+ detector network at a distance of 3.04 Mpc with an SLy equation of state and equal-mass $1.35\,{\rm M}_\odot$ neutron stars. Credible intervals of 68% are shown as dashed blue lines in the one-dimensional posteriors. The injected collapse time is shown by the orange lines in the lower-most panels.

Chapter 5

Conclusion

The direct observation of gravitational waves from the binary neutron star inspiral of GW170817 and coincident detections from GRB 170817A and AT2017gfo launched the nascent field of multi-messenger gravitational-wave astronomy. Gravitational waves from the late inspiral and post-merger remnant of GW170817 were not detected because the gravitational-wave detectors lacked sensitivity in high frequencies. High frequency gravitational-wave detectors have been proposed which may allow gravitational-wave observations of the binary neutron star post-merger remnant and late inspiral in the near-future.

Observations of gravitational waves from the late inspiral will inform the equation of state for cold neutron stars, whereas gravitational wave detections from surviving post-merger remnants will inform the extremely dense, hot equation of state. It should be noted that, to date, equation of state investigations have been performed using the cold equation of state (e.g. see [152, 212] for radius constraints at $\mathrm{M_{TOV}}$). Surviving post-merger remnants are binary neutron star remnants that have not yet collapsed to a black hole. We need models of the post-merger gravitational-wave strain to enable observations of gravitational waves from post-merger remnants. Numerical-relativity simulations are the best basis for these post-merger models.

We should not expect that future observable post-merger gravitational waves will precisely match numerical-relativity simulations, as the simulations are extremely complex. Compromises must be made in spatial-resolution, incorporated physics, and convergence testing, for simulations to complete in practical time-frames. The absolute accuracy of the phase evolution and the collapse time of the post-merger remnant are uncertain due to these compromises.

With these computational limitations in mind, we need simple models that can be used for gravitational-wave detection and parameter estimation. The main purpose of this thesis was to focus on this task. We achieve this goal by developing a hierarchical model that can infer the progenitor neutron star system parameters and generate gravitational-wave spectra. We develop a simple analytical frequency-drift model which successfully matches the numerical-relativity gravitational-wave strain. We modify the frequency-drift model to allow for collapsing remnants so that we can measure when the post-merger remnant collapses to a black hole.

In Chapter 2, we train our hierarchical model on 35 numerical-relativity simulations and measure leave-one-out cross-validated fitting-factors with a mean of 0.95. We show that we can generate gravitational-wave spectra in a fraction of a second, given only the neutron star mass, M, and the tidal coupling constant, κ_2^T. We perform parameter estimation on κ_2^T by using the fitting factor as a proxy for the likelihood. The hierarchical model is particularly suited to mod-

elling numerical-relativity simulations as it is insensitive to phase uncertainties that can occur between simulations with adjacent spatial resolutions.

In Chapter 3, we implement a third-order exponentially-damped sinusoid with a frequency-drift term to successfully capture the complex gravitational-wave strain from simulations of post-merger remnants. We find that we can achieve noise-weighted fitting-factors of $\gtrsim 0.92$, with most fitting factors of $\sim 0.95 - 0.97$. We use a detection threshold with a Bayes factor of ~ 3000 and find that a post-merger signal-to-noise ratio of $\gtrsim 7$ is needed to detect the post-merger remnant. We also find that the sensitivity to the uncertainty in the coalescence time is negligible for any detectable post-merger remnant. We calculate the dominant post-merger oscillation frequency, $f_{\rm peak}$, from the model and constrain this at 95% credible intervals to $\sim 1.5\%$ for a post-merger signal-to-noise ratio of 15, and $\sim 0.3\%$ for a post-merger signal-to-noise ratio of 50. We then use the hierarchical model trained in Chapter 2 to infer the equation of state parameters κ_2^T and C. At 95% confidence intervals, we constrain κ_2^T to $\sim 12\%$ for a post-merger signal-to-noise ratio of 15, and $\sim 5\%$ for a post-merger signal-to-noise ratio of 50. Similarly, we constrain C to $\sim 5\%$ for a signal-to-noise ratio of 15, and $\sim 2\%$ for a post-merger signal-to-noise ratio of 50.

In Chapter 4, we add a collapse-time function to our frequency-drift model and measure at what distance the collapse time can be measured. We find that we need a combination of Einstein Telescope and Cosmic Explorer interferometers to detect a collapse time of 10 ms at a GW170817-like distance of ~ 40 Mpc. For a network of 2 A+ detectors, a distance of $\sim$ 10Mpc is required to detect a 10 ms collapse time. If the high-frequency NEMO detector is added to the 2 A+ network then this detection distance is increased to ~ 25 Mpc.

These three models address the requirements for future post-merger gravitational-wave detections. The post-merger models consistently achieve $\gtrsim 0.90$ fitting factors, making them suitable for matched-filter detection of gravitational-wave signals. However, a number of enhancements can be anticipated for future work.

An obvious model enhancement would allow for unequal-mass binaries. In this case, the number of available numerical-relativity simulations are significantly reduced. This does not exclude training a modified hierarchical model on the unequal-mass simulations, though careful attention should be paid to the error propagation to count for the reduced number of simulations in this part of the training set. The frequency-drift model, with or without the collapse time extension, has yet to be tested with unequal-mass mergers. This could be tested and the model updated if required.

Measurements of larger collapse times are limited by waveform systematics in the late post-merger gravitational-wave strain. The same waveform systematics are also present in the model used in Chapter 3 for post-merger signals of length $\gtrsim 15$ ms. A couple of assumptions can be reassessed for future work on the frequency-drift model to help reduce these systematics. The first is that the linear frequency-drift term may be too restrictive for longer signals and other analytic or semi-analytic methods could be considered. Secondly, the assumption of exponential damping could be reassessed, considering, for example, a power-law decay in the amplitude instead.

The lifetimes of post-merger remnants are highly uncertain with gravitational-wave timescales ranging from $0.15 - 12$ s for a range of elliptic-

ities and equations of state (Eq.(1.14)). If the above waveform systematics are successfully addressed then detection and parameter estimation studies could be performed with much longer collapse times. A successful injection study for collapse times up to $\sim 2\,\mathrm{s}$ may allow the measurement of collapse times for future GW170817-like events. This would have significantly aided model selection for the gamma-ray physics associated with GRB 170817A.

For example, measuring any collapse of the post-merger remnant would rule out proposals that rely on surviving neutron star remnants [e.g., 59]. Measuring a collapse time of $\lesssim 0.5\,\mathrm{s}$ would reduce support for scenarios in Refs. [57, 58] where collapse times of at least $\sim 1\,\mathrm{s}$ are required so that jets are launched after black hole formation.

A small collapse time of $\lesssim 0.05\,\mathrm{s}$ will rule out models that rely on the temporary survival of the post-merger remnant to account for the colour of kilonova emission [56]. This highlights a few examples of how the collapse times may influence the physics of short gamma-ray bursts.

The models developed in this thesis could be used to develop detection pipelines for post-merger remnants. Pipelines already exist that are capable of searching for post-merger remnants: `cWB`, `BayesWave`, `Viterbi`, `STAMP`, `ATrHough`, and `FreqHough` [161, 162, 169, 170, 191–193, 213–217]. A number of these tools searched for a long-lived post-merger remnant from the GW170817 merger, with searches lasting $\lesssim 500\,\mathrm{s}$ (`STAMP`, `cWB`) [161] and searches ranging from $\sim 2 - 24\,\mathrm{hours}$ (`Viterbi`, `STAMP`, `ATrHough`, and `FreqHough`) [162]. Searches were also performed over $\lesssim 1\,\mathrm{s}$ (`cWB`) [161] and `BayesWave` has characterised the post-merger remnant from binary neutron star mergers [3, 165, 170, 193].

Pipelines developed from the analytical models in Chapters 3-4 could be designed to work with signals produced from numerical-relativity simulations with lengths of $\lesssim 100\,\mathrm{ms}$, or long signals of $\lesssim 2\,\mathrm{s}$. Pipelines that searched for the long-lived post-merger remnant should be used for signals longer than this. We propose two pipelines from this work: a short pipeline with a length of $\lesssim 100\,\mathrm{ms}$ and a long pipeline with length $\lesssim 2\,\mathrm{s}$.

Pipelines that are of direct interest for comparison with the analytical model are `BayesWave` and `cWB`. We find in Chapter 3 that `BayesWave` is more sensitive when measuring the dominant post-merger frequency, f_{peak}. `BayesWave` and the analytical model constrained f_{peak} to post-merger signal-to-noise ratios of $\gtrsim 9$, and $\gtrsim 15$, respectively. The `cWB` pipeline is expected to be the least sensitive as it detects unmodelled coherent excess power, assuming waveform systematics have been addressed in the analytical model.

The proposed pipeline would use Bayesian inference for detection and parameter estimation which will find posteriors directly related to the gravitational-wave strain of the post-merger remnant. This is an advantage over both `BayesWave` and `cWB`. The Bayes factor would serve as a robust detection statistic in this situation due to the loud inspiral signal and the tight constraint expected on the coalescence time. It may be necessary to perform computational optimisation to allow the long pipeline to execute in reasonable time frames, though it may be possible to use parallel Bilby [218] to speed up this pipeline.

The hierarchical model can only be used on the short pipeline because it is trained on numerical-relativity simulations. It is likely that the model will need to be extended to account for both spins and unequal-mass neutron stars, this

will need to be assessed. The hierarchical model can be trained on as many numerical-relativity simulations as possible with careful consideration taken in selecting the spatial resolution. The hierarchical model would then be available to infer equation of state parameters from the posterior waveforms generated from the analytical pipeline.

Although we are not expecting binary neutron star post-merger detections in the immediate future, they may be possible if proposed high-frequency gravitational-wave detectors like NEMO are constructed, or failing that, when Einstein telescope and Cosmic Explorer detectors are operational. With this in mind, we must ensure that we have the tools available to fully utilise any future binary neutron star post-merger detections so that we can probe the extreme physics of these remnants.

Bibliography

[1] G. Ashton, M. Hübner, P. D. Lasky, C. Talbot, K. Ackley, S. Biscoveanu, Q. Chu, A. Divakarla, P. J. Easter, B. Goncharov, *et al.*, "BILBY: a user-friendly Bayesian inference library for gravitational-wave astronomy," *The Astrophysical Journal Supplement*, vol. 241, p. 27, Apr. 2019.

[2] P. J. Easter, P. D. Lasky, A. R. Casey, L. Rezzolla, and K. Takami, "Computing fast and reliable gravitational waveforms of binary neutron star merger remnants," *Physical Review D*, vol. 100, p. 043005, Aug. 2019.

[3] P. J. Easter, S. Ghonge, P. D. Lasky, A. R. Casey, J. A. Clark, F. Hernandez Vivanco, and K. Chatziioannou, "Detection and parameter estimation of binary neutron star merger remnants," *Physical Review D*, vol. 102, p. 043011, Aug. 2020.

[4] E. Cuoco, J. Powell, M. Cavaglià, K. Ackley, M. Bejger, C. Chatterjee, M. Coughlin, S. Coughlin, P. J. Easter, R. Essick, *et al.*, "Enhancing gravitational-wave science with machine learning," *Machine Learning: Science and Technology*, vol. 2, p. 011002, Dec. 2020.

[5] P. J. Easter, P. D. Lasky, and A. R. Casey, "Can we measure the collapse time of a post-merger remnant for a future GW170817-like event?," *arXiv e-prints*, June 2021.

[6] B. P. Abbott, R. Abbott, T. D. Abbott, F. Acernese, K. Ackley, C. Adams, T. Adams, P. Addesso, R. X. Adhikari, V. B. Adya, *et al.*, "GW170817: observation of gravitational waves from a binary neutron star inspiral," *Physical Review Letters*, vol. 119, p. 161101, Oct. 2017.

[7] A. Goldstein, P. Veres, E. Burns, M. S. Briggs, R. Hamburg, D. Kocevski, C. A. Wilson-Hodge, R. D. Preece, S. Poolakkil, O. J. Roberts, *et al.*, "An Ordinary Short Gamma-Ray Burst with Extraordinary Implications: Fermi -GBM Detection of GRB 170817A," *The Astrophysical Journal*, vol. 848, p. L14, Oct. 2017.

[8] D. A. Coulter, R. J. Foley, C. D. Kilpatrick, M. R. Drout, A. L. Piro, B. J. Shappee, M. R. Siebert, J. D. Simon, N. Ulloa, D. Kasen, *et al.*, "Swope Supernova Survey 2017a (SSS17a), the optical counterpart to a gravitational wave source," *Science*, vol. 358, pp. 1556–1558, Dec. 2017.

[9] E. Troja, L. Piro, H. van Eerten, R. T. Wollaeger, M. Im, O. D. Fox, N. R. Butler, S. B. Cenko, T. Sakamoto, C. L. Fryer, *et al.*, "The X-ray counterpart to the gravitational-wave event GW170817," *Nature*, vol. 551, pp. 71–74, Nov. 2017.

[10] M. Nicholl, E. Berger, D. Kasen, B. D. Metzger, J. Elias, C. Briceño, K. D. Alexander, P. K. Blanchard, R. Chornock, P. S. Cowperthwaite, *et al.*, "The Electromagnetic Counterpart of the Binary Neutron Star Merger LIGO/Virgo GW170817. III. Optical and UV Spectra of a Blue Kilonova from Fast Polar Ejecta," *The Astrophysical Journal*, vol. 848, no. 2, p. L18, 2017.

[11] R. Chornock, E. Berger, D. Kasen, P. S. Cowperthwaite, M. Nicholl, V. A. Villar, K. D. Alexander, P. K. Blanchard, T. Eftekhari, W. Fong, *et al.*, " The Electromagnetic Counterpart of the Binary Neutron Star Merger LIGO/Virgo GW170817. IV. Detection of Near-infrared Signatures of r -process Nucleosynthesis with Gemini-South ," *The Astrophysical Journal*, vol. 848, no. 2, p. L19, 2017.

[12] R. Margutti, E. Berger, W. Fong, C. Guidorzi, K. D. Alexander, B. D. Metzger, P. K. Blanchard, P. S. Cowperthwaite, R. Chornock, T. Eftekhari, *et al.*, "The Electromagnetic Counterpart of the Binary Neutron Star Merger LIGO/Virgo GW170817. V. Rising X-Ray Emission from an Off-axis Jet," *The Astrophysical Journal*, vol. 848, no. 2, p. L20, 2017.

[13] K. D. Alexander, E. Berger, W. Fong, P. K. G. Williams, C. Guidorzi, R. Margutti, B. D. Metzger, J. Annis, P. K. Blanchard, D. Brout, *et al.*, "The Electromagnetic Counterpart of the Binary Neutron Star Merger LIGO/Virgo GW170817. VI. Radio Constraints on a Relativistic Jet and Predictions for Late-time Emission from the Kilonova Ejecta," *The Astrophysical Journal*, vol. 848, no. 2, p. L21, 2017.

[14] B. P. Abbott, R. Abbott, T. D. Abbott, F. Acernese, K. Ackley, C. Adams, T. Adams, P. Addesso, R. X. Adhikari, V. B. Adya, *et al.*, "Multi-messenger observations of a binary neutron star merger," *The Astrophysical Journal Letters*, vol. 848, p. L12, Oct. 2017.

[15] V. Moncrief, "Gravitational perturbations of spherically symmetric systems. I. The exterior problem," *Annals of Physics*, vol. 88, no. 2, pp. 323–342, 1974.

[16] A. M. Abrahams and R. H. Price, "Applying black hole perturbation theory to numerically generated spacetimes," *Physical Review D*, vol. 53, pp. 1963–1971, Feb. 1996.

[17] Z. Andrade and R. H. Price, "Excitation of the odd parity quasinormal modes of compact objects," *Physical Review D - Particles, Fields, Gravitation and Cosmology*, vol. 60, no. 10, pp. 1–15, 1999.

[18] A. Nagar and L. Rezzolla, "Gauge-invariant non-spherical metric perturbations of Schwarzschild black-hole spacetimes," *Classical and Quantum Gravity*, vol. 22, pp. R167–R192, Aug. 2005.

[19] L. Baiotti, B. Giacomazzo, and L. Rezzolla, "Accurate evolutions of inspiralling neutron-star binaries: Prompt and delayed collapse to a black hole," *Physical Review D*, vol. 78, p. 084033, Oct. 2008.

[20] R. A. Hulse and J. H. Taylor, "Discovery of a pulsar in a binary system," *The Astrophysical Journal*, vol. 195, p. L51, Jan. 1975.

[21] J. H. Taylor and J. M. Weisberg, "A new test of general relativity - Gravitational radiation and the binary pulsar PSR 1913+16," *The Astrophysical Journal*, vol. 253, p. 908, Feb. 1982.

[22] J. M. Weisberg and Y. Huang, "Relativistic Measurements from Timing the Binary Pulsar PSR B1913+16," *The Astrophysical Journal*, vol. 829, p. 55, Sept. 2016.

[23] B. P. Abbott, R. Abbott, T. D. Abbott, M. R. Abernathy, F. Acernese, K. Ackley, C. Adams, T. Adams, P. Addesso, R. X. Adhikari, *et al.*, "Observation of Gravitational Waves from a Binary Black Hole Merger," *Physical Review Letters*, vol. 116, p. 61102, Feb. 2016.

[24] C. Cutler and I. E. Flanagan, "Gravitational waves from merging compact binaries: How accurately can one extract the binary's parameters from the inspiral waveform?," *Physical Review D*, vol. 49, no. 6, pp. 2658–2697, 1994.

[25] J. Aasi, B. P. Abbott, R. Abbott, T. Abbott, M. R. Abernathy, K. Ackley, C. Adams, T. Adams, P. Addesso, R. X. Adhikari, *et al.*, "Advanced LIGO," *Classical and Quantum Gravity*, vol. 32, p. 074001, Apr. 2015.

[26] F. Acernese, M. Agathos, K. Agatsuma, D. Aisa, N. Allemandou, A. Allocca, J. Amarni, P. Astone, G. Balestri, G. Ballardin, *et al.*, "Advanced Virgo: a second-generation interferometric gravitational wave detector," *Classical and Quantum Gravity*, vol. 32, p. 024001, Jan. 2015.

[27] B. P. Abbott, R. Abbott, T. D. Abbott, S. Abraham, F. Acernese, K. Ackley, C. Adams, R. X. Adhikari, V. B. Adya, C. Affeldt, *et al.*, "GW190425: Observation of a Compact Binary Coalescence with Total Mass $\sim 3.4 M_{\odot}$," *The Astrophysical Journal*, vol. 892, p. L3, Mar. 2020.

[28] R. Abbott, T. D. Abbott, S. Abraham, F. Acernese, K. Ackley, A. Adams, C. Adams, R. X. Adhikari, V. B. Adya, C. Affeldt, *et al.*, "GWTC-2: Compact Binary Coalescences Observed by LIGO and Virgo During the First Half of the Third Observing Run," *arXiv*, pp. 1–52, 2020.

[29] The LIGO Scientific Collaboration, the Virgo Collaboration, R. Abbott, T. D. Abbott, S. Abraham, F. Acernese, K. Ackley, A. Adams, C. Adams, R. X. Adhikari, *et al.*, "Population properties of compact objects from the second LIGO-Virgo gravitational-wave transient catalog," *arXiv e-prints*, Oct. 2020.

[30] J. Miller, L. Barsotti, S. Vitale, P. Fritschel, M. Evans, and D. Sigg, "Prospects for doubling the range of Advanced LIGO," *Physical Review D*, vol. 91, p. 062005, Mar. 2015.

[31] K. Ackley, V. B. Adya, P. Agrawal, P. Altin, G. Ashton, M. Bailes, E. Baltinas, A. Barbuio, D. Beniwal, C. Blair, *et al.*, "Neutron star Extreme Matter Observatory: A kilohertz-band gravitational-wave detector in the global network," *Publications of the Astronomical Society of Australia*, vol. 37, p. e047, 2020.

[32] LIGO Scientific Collaboration, "Exploring the sensitivity of next generation gravitational wave detectors," 2016. https://dcc.ligo.org/LIGO-P1600143/public, curve_data.txt.

[33] M. Punturo, M. Abernathy, F. Acernese, B. Allen, N. Andersson, K. Arun, F. Barone, B. Barr, M. Barsuglia, M. Beker, *et al.*, "The third generation of gravitational wave observatories and their science reach," *Classical and Quantum Gravity*, vol. 27, p. 084007, Apr. 2010.

[34] J. M. M. Lattimer and M. Prakash, "The Physics of Neutron Stars," *Science*, vol. 304, pp. 536–542, May 2004.

[35] A. J. Ruiter, L. Ferrario, K. Belczynski, I. R. Seitenzahl, R. M. Crocker, and A. I. Karakas, "On the formation of neutron stars via accretion-induced collapse in binaries," *Monthly Notices of the Royal Astronomical Society*, vol. 484, pp. 698–711, Mar. 2019.

[36] X. Liu, "The Remnant of Neutron Star-White Dwarf Merger and the Repeating Fast Radio Bursts," *International Journal of Astronomy and Astrophysics*, vol. 10, pp. 28–38, Feb. 2020.

[37] D. Liu and B. Wang, "The formation of single neutron stars from double white-dwarf mergers via accretion-induced collapse," *Monthly Notices of the Royal Astronomical Society*, vol. 494, pp. 3422–3431, May 2020.

[38] J. A. Pons, S. Reddy, M. Prakash, J. M. Lattimer, and J. A. Miralles, "Evolution of Proto–Neutron Stars," *The Astrophysical Journal*, vol. 513, pp. 780–804, Mar. 1999.

[39] D. Yakovlev, "Neutrino emission from neutron stars," *Physics Reports*, vol. 354, pp. 1–155, Nov. 2001.

[40] V. Paschalidis, Z. B. Etienne, and S. L. Shapiro, "Importance of cooling in triggering the collapse of hypermassive neutron stars," *Physical Review D*, vol. 86, p. 064032, Aug. 2012.

[41] A. Perego, S. Bernuzzi, and D. Radice, "Thermodynamics conditions of matter in neutron star mergers," *The European Physical Journal A*, vol. 55, p. 124, Aug. 2019.

[42] A. Reisenegger, "Magnetic Fields of Neutron Stars: an Overview," in *Magnetic Fields Across the Hertzsprung-Russell Diagram* (G. Mathys, S. Solanki, and D. Wickramasinghe, eds.), vol. 248 of *Astronomical Society of the Pacific Conference Series*, p. 469, Jan. 2001.

[43] R. N. Manchester, "Observational Properties of Pulsars," *Science*, vol. 304, pp. 542–546, Apr. 2004.

[44] R. C. Tolman, "Static solutions of einstein's field equations for spheres of fluid," *Physical Review*, vol. 55, no. 4, pp. 364–373, 1939.

[45] J. R. Oppenheimer and G. M. Volkoff, "On massive neutron cores," *Physical Review*, vol. 55, no. 4, pp. 374–381, 1939.

[46] H. Hu, M. Kramer, N. Wex, D. J. Champion, and M. S. Kehl, "Constraining the dense matter equation-of-state with radio pulsars," *Monthly Notices of the Royal Astronomical Society*, vol. 497, no. 3, pp. 3118–3130, 2020.

[47] J. Antoniadis, P. C. C. Freire, N. Wex, T. M. Tauris, R. S. Lynch, M. H. van Kerkwijk, M. Kramer, C. Bassa, V. S. Dhillon, T. Driebe, *et al.*, "A Massive Pulsar in a Compact Relativistic Binary," *Science*, vol. 340, pp. 1233232–1233232, Apr. 2013.

[48] H. T. Cromartie, E. Fonseca, S. M. Ransom, P. B. Demorest, Z. Arzoumanian, H. Blumer, P. R. Brook, M. E. DeCesar, T. Dolch, J. A. Ellis, *et al.*, "Relativistic Shapiro delay measurements of an extremely massive millisecond pulsar," *Nature Astronomy*, vol. 4, pp. 72–76, Jan. 2020.

[49] L. Blanchet, T. Damour, B. R. Iyer, C. M. Will, and A. G. Wiseman, "Gravitational-radiation damping of compact binary systems to second post-Newtonian order," *Physical Review Letters*, vol. 74, no. 18, pp. 3515–3518, 1995.

[50] A. Buonanno and T. Damour, "Effective one-body approach to general relativistic two-body dynamics," *Physical Review D - Particles, Fields, Gravitation and Cosmology*, vol. 59, no. 8, pp. 1–24, 1999.

[51] S. Droz, D. J. Knapp, E. Poisson, and B. J. Owen, "Gravitational waves from inspiraling compact binaries: Validity of the stationary-phase approximation to the Fourier transform," *Physical Review D*, vol. 59, p. 124016, May 1999.

[52] T. Damour, A. Nagar, and L. Villain, "Measurability of the tidal polarizability of neutron stars in late-inspiral gravitational-wave signals," *Physical Review D*, vol. 85, no. 12, 2012.

[53] K. Yagi and N. Yunes, "I-Love-Q relations in neutron stars and their applications to astrophysics, gravitational waves, and fundamental physics," *Physical Review D*, vol. 88, p. 023009, July 2013.

[54] L. Blanchet, "Gravitational radiation from post-newtonian sources and inspiralling compact binaries," *Living Reviews in Relativity*, vol. 17, no. 2014, 2014.

[55] B. P. Abbott, R. Abbott, T. D. Abbott, F. Acernese, K. Ackley, C. Adams, T. Adams, P. Addesso, R. X. Adhikari, V. B. Adya, *et al.*, "Properties of the binary neutron star merger GW170817," *Physical Review X*, vol. 9, p. 011001, Jan. 2019.

[56] B. D. Metzger, T. A. Thompson, and E. Quataert, "A magnetar origin for the kilonova ejecta in GW170817," *The Astrophysical Journal*, vol. 856, no. 2, p. 101, 2018.

[57] R. Gill, A. Nathanail, and L. Rezzolla, "When did the remnant of GW170817 collapse to a black hole?," *The Astrophysical Journal*, vol. 876, p. 139, May 2019.

[58] A. Murguia-Berthier, E. Ramirez-Ruiz, F. D. Colle, A. Janiuk, S. Rosswog, and W. H. Lee, "The Fate of the Merger Remnant in GW170817 and Its Imprint on the Jet Structure," *The Astrophysical Journal*, vol. 908, p. 152, Feb. 2021.

[59] Y.-W. Yu, L.-D. Liu, and Z.-G. Dai, "A long-lived remnant neutron star after GW170817 inferred from its associated kilonova," *The Astrophysical Journal*, vol. 861, p. 114, July 2018.

[60] E. Gourgoulhon, P. Grandclément, K. Taniguchi, J.-A. Marck, and S. Bonazzola, "Quasiequilibrium sequences of synchronized and irrotational binary neutron stars in general relativity: Method and tests," *Physical Review D*, vol. 63, p. 064029, Feb. 2001.

[61] A. Tsokaros, K. Uryū, and L. Rezzolla, "New code for quasiequilibrium initial data of binary neutron stars: Corotating, irrotational, and slowly spinning systems," *Physical Review D*, vol. 91, p. 104030, May 2015.

[62] K. Uryū and A. Tsokaros, "New code for equilibriums and quasiequilibrium initial data of compact objects," *Physical Review D*, vol. 85, p. 064014, Mar. 2012.

[63] R. Arnowitt, S. Deser, and C. W. Misner, "Republication of: The dynamics of general relativity," *General Relativity and Gravitation*, vol. 40, pp. 1997–2027, Sept. 2008.

[64] T. Nakamura, K. Oohara, and Y. Kojima, "General Relativistic Collapse to Black Holes and Gravitational Waves from Black Holes," *Progress of Theoretical Physics Supplement*, vol. 90, pp. 1–218, 1987.

[65] M. Shibata and T. Nakamura, "Evolution of three-dimensional gravitational waves: Harmonic slicing case," *Physical Review D*, vol. 52, pp. 5428–5444, Nov. 1995.

[66] T. W. Baumgarte and S. L. Shapiro, "Numerical integration of Einstein's field equations," *Physical Review D*, vol. 59, p. 024007, Dec. 1998.

[67] M. Alcubierre, B. Brügmann, T. Dramlitsch, J. A. Font, P. Papadopoulos, E. Seidel, N. Stergioulas, and R. Takahashi, "Towards a stable numerical evolution of strongly gravitating systems in general relativity: The conformal treatments," *Physical Review D*, vol. 62, p. 044034, July 2000.

[68] C. Bona, T. Ledvinka, C. Palenzuela, and M. Žáček, "General-covariant evolution formalism for numerical relativity," *Physical Review D*, vol. 67, p. 104005, May 2003.

[69] C. Bona and C. Palenzuela, "Dynamical shift conditions for the Z4 and BSSN formalisms," *Physical Review D*, vol. 69, p. 104003, May 2004.

[70] C. Gundlach, G. Calabrese, I. Hinder, and J. M. Martín-García, "Constraint damping in the Z4 formulation and harmonic gauge," *Classical and Quantum Gravity*, vol. 22, no. 17, pp. 3767–3773, 2005.

[71] S. Bernuzzi and D. Hilditch, "Constraint violation in free evolution schemes: Comparing the BSSNOK formulation with a conformal decomposition of the Z4 formulation," *Physical Review D*, vol. 81, p. 084003, Apr. 2010.

[72] D. Hilditch, S. Bernuzzi, M. Thierfelder, Z. Cao, W. Tichy, and B. Brügmann, "Compact binary evolutions with the Z4c formulation," *Physical Review D*, vol. 88, p. 084057, Oct. 2013.

[73] S. Brandt, R. Correll, R. Gómez, M. Huq, P. Laguna, L. Lehner, P. Marronetti, R. A. Matzner, D. Neilsen, J. Pullin, *et al.*, "Grazing Collisions of Black Holes via the Excision of Singularities," *Physical Review Letters*, vol. 85, pp. 5496–5499, Dec. 2000.

[74] L. E. Kidder, M. A. Scheel, and S. A. Teukolsky, "Extending the lifetime of 3D black hole computations with a new hyperbolic system of evolution equations," *Physical Review D*, vol. 64, p. 064017, Aug. 2001.

[75] M. Alcubierre, W. Benger, B. Brügmann, G. Lanfermann, L. Nerger, E. Seidel, and R. Takahashi, "3D Grazing Collision of Two Black Holes," *Physical Review Letters*, vol. 87, p. 271103, Dec. 2001.

[76] T. Nakamura and K.-I. Oohara, "A Way to 3D Numerical Relativity — Coalescing Binary Neutron Stars —," *arXiv e-prints*, vol. 2, pp. 247–256, Dec. 1998.

[77] M. Shibata, "Fully General Relativistic Simulation of Merging Binary Clusters: Spatial Gauge Condition," *Progress of Theoretical Physics*, vol. 101, pp. 1199–1233, June 1999.

[78] M. Alcubierre, B. Brügmann, D. Pollney, E. Seidel, and R. Takahashi, "Black hole excision for dynamic black holes," *Physical Review D*, vol. 64, p. 061501, Aug. 2001.

[79] M. Ruiz, D. Hilditch, and S. Bernuzzi, "Constraint preserving boundary conditions for the Z4c formulation of general relativity," *Physical Review D*, vol. 83, p. 024025, Jan. 2011.

[80] L. Baiotti, I. Hawke, P. J. Montero, F. Löffler, L. Rezzolla, N. Stergioulas, J. A. Font, and E. Seidel, "Three-dimensional relativistic simulations of rotating neutron-star collapse to a Kerr black hole," *Physical Review D*, vol. 71, p. 024035, Jan. 2005.

[81] D. Radice, L. Rezzolla, and F. Galeazzi, "Beyond second-order convergence in simulations of binary neutron stars in full general relativity," *Monthly Notices of the Royal Astronomical Society: Letters*, vol. 437, pp. L46–L50, Jan. 2014.

[82] D. Radice, L. Rezzolla, and F. Galeazzi, "High-order fully general-relativistic hydrodynamics: new approaches and tests," *Classical and Quantum Gravity*, vol. 31, p. 075012, Apr. 2014.

[83] D. Radice, L. Rezzolla, and F. Galeazzi, "High-Order Numerical-Relativity Simulations of Binary Neutron Stars," *Astronomical Society of the Pacific Conference Series*, vol. 498, pp. 121–126, Feb. 2015.

[84] B. Brügmann, W. Tichy, and N. Jansen, "Numerical Simulation of Orbiting Black Holes," *Physical Review Letters*, vol. 92, p. 211101, May 2004.

[85] B. Brügmann, J. A. González, M. Hannam, S. Husa, U. Sperhake, and W. Tichy, "Calibration of moving puncture simulations," *Physical Review D*, vol. 77, p. 024027, Jan. 2008.

[86] M. Thierfelder, S. Bernuzzi, and B. Brügmann, "Numerical relativity simulations of binary neutron stars," *Physical Review D*, vol. 84, p. 044012, Aug. 2011.

[87] T. Dietrich, S. Bernuzzi, M. Ujevic, and B. Brügmann, "Numerical relativity simulations of neutron star merger remnants using conservative mesh refinement," *Physical Review D*, vol. 91, p. 124041, June 2015.

[88] S. Bernuzzi and T. Dietrich, "Gravitational waveforms from binary neutron star mergers with high-order weighted-essentially-nonoscillatory schemes in numerical relativity," *Physical Review D*, vol. 94, p. 064062, Sept. 2016.

[89] T. Dietrich, S. Ossokine, and K. Clough, "Full 3D numerical relativity simulations of neutron star–boson star collisions with BAM," *Classical and Quantum Gravity*, vol. 36, p. 025002, Jan. 2019.

[90] B. Giacomazzo and L. Rezzolla, "WhiskyMHD: a new numerical code for general relativistic magnetohydrodynamics," *Classical and Quantum Gravity*, vol. 24, pp. S235–S258, June 2007.

[91] B. Giacomazzo, L. Rezzolla, and L. Baiotti, "Accurate evolutions of inspiralling and magnetized neutron stars: equal-mass binaries," *Physical Review D*, vol. 83, p. 044014, Feb. 2011.

[92] B. Giacomazzo and R. Perna, "Formation of stable magnetars from binary neutron star mergers," *The Astrophysical Journal*, vol. 771, p. L26, June 2013.

[93] S. Bernuzzi, A. Nagar, S. Balmelli, T. Dietrich, and M. Ujevic, "Quasiuniversal properties of neutron star mergers," *Physical Review Letters*, vol. 112, p. 201101, May 2014.

[94] L. Rezzolla and K. Takami, "Gravitational-wave signal from binary neutron stars: A systematic analysis of the spectral properties," *Physical Review D*, vol. 93, p. 124051, June 2016.

[95] D. Radice, S. Bernuzzi, and C. D. Ott, "One-armed spiral instability in neutron star mergers and its detectability in gravitational waves," *Physical Review D*, vol. 94, p. 064011, Sept. 2016.

[96] T. Dietrich and T. Hinderer, "Comprehensive comparison of numerical relativity and effective-one-body results to inform improvements in waveform models for binary neutron star systems," *Physical Review D*, vol. 95, p. 124006, June 2017.

[97] D. Radice, "General-relativistic large-eddy simulations of binary neutron star mergers," *The Astrophysical Journal Letters*, vol. 838, p. L2, Mar. 2017.

[98] D. Radice, S. Bernuzzi, W. Del Pozzo, L. F. Roberts, and C. D. Ott, "Probing extreme-density matter with gravitational-wave observations of binary neutron star merger remnants," *The Astrophysical Journal Letters*, vol. 842, p. L10, June 2017.

[99] D. Radice, A. Perego, F. Zappa, and S. Bernuzzi, "GW170817: joint constraint on the neutron star equation of state from multimessenger observations," *The Astrophysical Journal Letters*, vol. 852, p. L29, Jan. 2018.

[100] T. Dietrich, D. Radice, S. Bernuzzi, F. Zappa, A. Perego, B. Brueugmann, S. Vivekanandji Chaurasia, R. Dudi, W. Tichy, and M. Ujevic, "CoRe database of binary neutron star merger waveforms and its application in waveform development," *arXiv e-prints*, June 2018.

[101] K. Takami, L. Rezzolla, and L. Baiotti, "Spectral properties of the post-merger gravitational-wave signal from binary neutron stars," *Physical Review D*, vol. 91, p. 064001, Mar. 2015.

[102] M. Shibata, T. W. Baumgarte, and S. L. Shapiro, "The bar-mode instability in differentially rotating neutron stars: simulations in full general relativity," *The Astrophysical Journal*, vol. 542, pp. 453–463, Oct. 2000.

[103] P. Cerdá-Durán, "Numerical viscosity in hydrodynamics simulations in general relativity," *Classical and Quantum Gravity*, vol. 27, Dec. 2009.

[104] S. Bernuzzi, M. Thierfelder, and B. Brügmann, "Accuracy of numerical relativity waveforms from binary neutron star mergers and their comparison with post-Newtonian waveforms," *Physical Review D*, vol. 85, p. 104030, May 2012.

[105] S. Bernuzzi, A. Nagar, M. Thierfelder, and B. Brügmann, "Tidal effects in binary neutron star coalescence," *Physical Review D*, vol. 86, p. 044030, Aug. 2012.

[106] Y. Sekiguchi, K. Kiuchi, K. Kyutoku, M. Shibata, and K. Taniguchi, "Dynamical mass ejection from the merger of asymmetric binary neutron stars: Radiation-hydrodynamics study in general relativity," Phys. Rev. D, vol. 93, p. 124046, June 2016.

[107] Y. Sekiguchi, K. Kiuchi, K. Kyutoku, and M. Shibata, "Gravitational Waves and Neutrino Emission from the Merger of Binary Neutron Stars," *Physical Review Letters*, vol. 107, p. 051102, July 2011.

[108] A. Perego, S. Rosswog, R. M. Cabezon, O. Korobkin, R. Kappeli, A. Arcones, and M. Liebendorfer, "Neutrino-driven winds from neutron star merger remnants," *Monthly Notices of the Royal Astronomical Society*, vol. 443, pp. 3134–3156, Aug. 2014.

[109] F. Foucart, R. Haas, M. D. Duez, E. O'Connor, C. D. Ott, L. Roberts, L. E. Kidder, J. Lippuner, H. P. Pfeiffer, and M. A. Scheel, "Low mass binary neutron star mergers: Gravitational waves and neutrino emission," *Physical Review D*, vol. 93, no. 4, pp. 1–23, 2016.

[110] D. Radice, F. Galeazzi, J. Lippuner, L. F. Roberts, C. D. Ott, and L. Rezzolla, "Dynamical mass ejection from binary neutron star mergers," *Monthly Notices of the Royal Astronomical Society*, vol. 460, pp. 3255–3271, Aug. 2016.

[111] F. Zappa, S. Bernuzzi, D. Radice, A. Perego, and T. Dietrich, "Gravitational-wave luminosity of binary neutron stars mergers," *Physical Review Letters*, vol. 120, no. 11, p. 111101, 2018.

[112] S. L. Shapiro, "Differential Rotation in Neutron Stars: Magnetic Braking and Viscous Damping," *The Astrophysical Journal*, vol. 544, pp. 397–408, Nov. 2000.

[113] M. D. Duez, Y. T. Liu, S. L. Shapiro, and B. C. Stephens, "General relativistic hydrodynamics with viscosity: Contraction, catastrophic collapse, and disk formation in hypermassive neutron stars," *Physical Review D*, vol. 69, p. 104030, May 2004.

[114] M. Shibata, K. Kiuchi, and Y.-i. Sekiguchi, "General relativistic viscous hydrodynamics of differentially rotating neutron stars," *Physical Review D*, vol. 95, p. 083005, Apr. 2017.

[115] M. D. Duez, Y. T. Liu, S. L. Shapiro, M. Shibata, and B. C. Stephens, "Collapse of Magnetized Hypermassive Neutron Stars in General Relativity," *Physical Review Letters*, vol. 96, p. 031101, Jan. 2006.

[116] M. D. Duez, Y. T. Liu, S. L. Shapiro, M. Shibata, and B. C. Stephens, "Evolution of magnetized, differentially rotating neutron stars: Simulations in full general relativity," *Physical Review D*, vol. 73, pp. 1–25, May 2006.

[117] D. M. Siegel, R. Ciolfi, A. I. Harte, and L. Rezzolla, "Magnetorotational instability in relativistic hypermassive neutron stars," *Physical Review D*, vol. 87, p. 121302, June 2013.

[118] D. M. Siegel, R. Ciolfi, and L. Rezzolla, "Magnetically driven winds from differentially rotating neutron stars and X-ray afterglows of short gamma-ray bursts," *The Astrophysical Journal*, vol. 785, p. L6, Mar. 2014.

[119] K. Kiuchi, K. Kyutoku, and M. Shibata, "Three-dimensional evolution of differentially rotating magnetized neutron stars," *Physical Review D*, vol. 86, p. 064008, Sept. 2012.

[120] K. Kiuchi, K. Kyutoku, Y. Sekiguchi, M. Shibata, and T. Wada, "High resolution numerical relativity simulations for the merger of binary magnetized neutron stars," *Physical Review D*, vol. 90, p. 041502, Aug. 2014.

[121] B. Giacomazzo, J. Zrake, P. C. Duffell, A. I. MacFadyen, and R. Perna, "Producing Magnetar Magnetic Fields in the Merger of Binary Neutron Stars," *The Astrophysical Journal*, vol. 809, p. 39, Aug. 2015.

[122] R. Gamba, M. Breschi, S. Bernuzzi, M. Agathos, and A. Nagar, "Waveform systematics in the gravitational-wave inference of tidal parameters and equation of state from binary neutron-star signals," *Physical Review D*, vol. 103, p. 124015, June 2021.

[123] L. R. Weih, E. R. Most, and L. Rezzolla, "On the stability and maximum mass of differentially rotating relativistic stars," *Monthly Notices of the Royal Astronomical Society: Letters*, vol. 473, no. 1, pp. L126–L130, 2018.

[124] C. Breu and L. Rezzolla, "Maximum mass, moment of inertia and compactness of relativistic stars," *Monthly Notices of the Royal Astronomical Society*, vol. 459, pp. 646–656, June 2016.

[125] A. Bauswein, H.-T. Janka, and R. Oechslin, "Testing approximations of thermal effects in neutron star merger simulations," *Physical Review D*, vol. 82, p. 084043, Oct. 2010.

[126] J. D. Kaplan, C. D. Ott, E. P. O'Connor, K. Kiuchi, L. Roberts, and M. Duez, "The Influence of Thermal Pressure on Equilibrium Models of Hypermassive Neutron Star Merger Remnants," *Astrophysical Journal*, vol. 790, June 2013.

[127] B. Margalit and B. D. Metzger, "Constraining the Maximum Mass of Neutron Stars from Multi-messenger Observations of GW170817," *The Astrophysical Journal*, vol. 850, p. L19, Nov. 2017.

[128] L. Rezzolla, E. R. Most, and L. R. Weih, "Using Gravitational-wave Observations and Quasi-universal Relations to Constrain the Maximum Mass of Neutron Stars," *The Astrophysical Journal*, vol. 852, p. L25, Jan. 2018.

[129] S. Khadkikar, A. R. Raduta, M. Oertel, and A. Sedrakian, "Maximum mass of compact stars from gravitational wave events with finite-temperature equations of state," *Physical Review C*, vol. 103, p. 055811, May 2021.

[130] M. Shibata, E. Zhou, K. Kiuchi, and S. Fujibayashi, "Constraint on the maximum mass of neutron stars using GW170817 event," *Physical Review D*, vol. 100, p. 023015, July 2019.

[131] N. Sarin, P. D. Lasky, and G. Ashton, "Gravitational waves or deconfined quarks: What causes the premature collapse of neutron stars born in short gamma-ray bursts?," *Physical Review D*, vol. 101, p. 063021, Mar. 2020.

[132] M. G. Alford and S. P. Harris, "Beta equilibrium in neutron-star mergers," *Physical Review C*, vol. 98, p. 065806, Dec. 2018.

[133] K. Sumiyoshi, S. Fujibayashi, Y. Sekiguchi, and M. Shibata, "Properties of Neutrino Transfer in a Deformed Remnant of a Neutron Star Merger," *The Astrophysical Journal*, vol. 907, p. 92, Feb. 2021.

[134] S. Bernuzzi, D. Radice, C. D. Ott, L. F. Roberts, P. Mösta, and F. Galeazzi, "How loud are neutron star mergers?," *Physical Review D*, vol. 94, p. 24023, July 2016.

[135] L. Rezzolla, L. Baiotti, B. Giacomazzo, D. Link, and J. A. Font, "Accurate evolutions of unequal-mass neutron-star binaries: properties of the torus and short GRB engines," *Classical and Quantum Gravity*, vol. 27, p. 114105, June 2010.

[136] R. Ciolfi, W. Kastaun, B. Giacomazzo, A. Endrizzi, D. M. Siegel, and R. Perna, "General relativistic magnetohydrodynamic simulations of binary neutron star mergers forming a long-lived neutron star," *Physical Review D*, vol. 95, p. 063016, Mar. 2017.

[137] R. Ciolfi, W. Kastaun, J. V. Kalinani, and B. Giacomazzo, "First 100 ms of a long-lived magnetized neutron star formed in a binary neutron star merger," *Physical Review D*, vol. 100, p. 023005, Apr. 2019.

[138] R. De Pietri, A. Feo, J. A. Font, F. Löffler, M. Pasquali, and N. Stergioulas, "Numerical-relativity simulations of long-lived remnants of binary neutron star mergers," *Physical Review D*, vol. 101, p. 064052, Mar. 2020.

[139] M. Shibata and K. Kiuchi, "Gravitational waves from remnant massive neutron stars of binary neutron star merger: Viscous hydrodynamics effects," *Physical Review D*, vol. 95, p. 123003, June 2017.

[140] M. Shibata, T. Nakamura, and K.-i. Oohara, "Coalescence of Spinning Binary Neutron Stars of Equal Mass: 3D Numerical Simulations," *Progress of Theoretical Physics*, vol. 88, pp. 1079–1095, Dec. 1992.

[141] X. Zhuge, J. M. Centrella, and S. L. McMillan, "Gravitational radiation from coalescing binary neutron stars," *Physical Review D*, vol. 50, no. 10, pp. 6247–6261, 1994.

[142] N. Stergioulas, A. Bauswein, K. Zagkouris, and H.-T. Janka, "Gravitational waves and non-axisymmetric oscillation modes in mergers of compact object binaries," *Monthly Notices of the Royal Astronomical Society*, vol. 418, pp. 427–436, Nov. 2011.

[143] A. Bauswein and N. Stergioulas, "Unified picture of the post-merger dynamics and gravitational wave emission in neutron star mergers," *Physical Review D*, vol. 91, p. 124056, June 2015.

[144] K. Takami, L. Rezzolla, and L. Baiotti, "Constraining the equation of state of neutron stars from binary mergers," *Physical Review Letters*, vol. 113, p. 091104, Aug. 2014.

[145] A. Bauswein and N. Stergioulas, "Spectral classification of gravitational-wave emission and equation of state constraints in binary neutron star mergers," *Journal of Physics G: Nuclear and Particle Physics*, vol. 46, p. 113002, Nov. 2019.

[146] S. Vretinaris, N. Stergioulas, and A. Bauswein, "Empirical relations for gravitational-wave asteroseismology of binary neutron star mergers," *Physical Review D*, vol. 101, p. 084039, Apr. 2020.

[147] A. Bauswein, N. Stergioulas, and H.-T. Janka, "Exploring properties of high-density matter through remnants of neutron-star mergers," *European Physical Journal A*, vol. 52, p. 56, Mar. 2016.

[148] S. Bose, K. Chakravarti, L. Rezzolla, B. S. Sathyaprakash, and K. Takami, "Neutron-star radius from a population of binary neutron star mergers," *Physical Review Letters*, vol. 120, p. 031102, Jan. 2018.

[149] T. Dietrich, M. Ujevic, W. Tichy, S. Bernuzzi, and B. Brügmann, "Gravitational waves and mass ejecta from binary neutron star mergers: Effect of the mass ratio," *Physical Review D*, vol. 95, p. 024029, Jan. 2017.

[150] T. Dietrich, S. Bernuzzi, M. Ujevic, and W. Tichy, "Gravitational waves and mass ejecta from binary neutron star mergers: effect of the stars' rotation," *Physical Review D*, vol. 95, p. 044045, Feb. 2017.

[151] F. Maione, R. De Pietri, A. Feo, and F. Löffler, "Spectral analysis of gravitational waves from binary neutron star merger remnants," *Physical Review D*, vol. 96, p. 063011, Sept. 2017.

[152] M. Breschi, S. Bernuzzi, F. Zappa, M. Agathos, A. Perego, D. Radice, and A. Nagar, "Kilohertz gravitational waves from binary neutron star remnants: Time-domain model and constraints on extreme matter," *Physical Review D*, vol. 100, p. 104029, Nov. 2019.

[153] N. Andersson and K. D. Kokkotas, "Towards gravitational wave asteroseismology," *Monthly Notices of the Royal Astronomical Society*, vol. 299, pp. 1059–1068, Oct. 1998.

[154] A. Bauswein and H.-T. Janka, "Measuring neutron-star properties via gravitational waves from neutron-star mergers," *Physical Review Letters*, vol. 108, p. 011101, Jan. 2012.

[155] A. Bauswein, H.-T. Janka, K. Hebeler, and A. Schwenk, "Equation-of-state dependence of the gravitational-wave signal from the ring-down phase of neutron-star mergers," *Physical Review D*, vol. 86, p. 063001, Sept. 2012.

[156] K. Yagi and N. Yunes, "I-Love-Q: Unexpected Universal Relations for Neutron Stars and Quark Stars," *Science*, vol. 341, pp. 365–368, July 2013.

[157] J. S. Read, L. Baiotti, J. D. E. Creighton, J. L. Friedman, B. Giacomazzo, K. Kyutoku, C. Markakis, L. Rezzolla, M. Shibata, and K. Taniguchi, "Matter effects on binary neutron star waveforms," *Physical Review D*, vol. 88, p. 044042, Aug. 2013.

[158] E. Annala, T. Gorda, A. Kurkela, and A. Vuorinen, "Gravitational-wave constraints on the neutron-star-matter equation of state," *Physical Review Letters*, vol. 120, p. 172703, Apr. 2018.

[159] E. R. Most, L. R. Weih, L. Rezzolla, and J. Schaffner-Bielich, "New constraints on radii and tidal deformabilities of neutron stars from GW170817," *Physical Review Letters*, vol. 120, p. 261103, June 2018.

[160] S. De, D. Finstad, J. M. Lattimer, D. A. Brown, E. Berger, and C. M. Biwer, "Tidal deformabilities and radii of neutron stars from the observation of GW170817," *Physical Review Letters*, vol. 121, p. 091102, Aug. 2018.

[161] B. P. Abbott, R. Abbott, T. D. Abbott, F. Acernese, K. Ackley, C. Adams, T. Adams, P. Addesso, R. X. Adhikari, V. B. Adya, and et al., "Search for Post-merger Gravitational Waves from the Remnant of the Binary Neutron Star Merger GW170817," ApJ, vol. 851, p. L16, Dec. 2017.

[162] B. P. Abbott, R. Abbott, T. D. Abbott, F. Acernese, K. Ackley, C. Adams, T. Adams, P. Addesso, R. X. Adhikari, V. B. Adya, *et al.*, "Search for Gravitational Waves from a Long-lived Remnant of the Binary Neutron Star Merger GW170817," ApJ, vol. 875, p. 160, Apr. 2019.

[163] K. Hotokezaka, K. Kiuchi, K. Kyutoku, T. Muranushi, Y.-i. Sekiguchi, M. Shibata, and K. Taniguchi, "Remnant massive neutron stars of binary neutron star mergers: evolution process and gravitational waveform," *Physical Review D*, vol. 88, p. 044026, Aug. 2013.

[164] S. Bernuzzi, T. Dietrich, and A. Nagar, "Modeling the complete gravitational wave spectrum of neutron star mergers," *Physical Review Letters*, vol. 115, p. 091101, Aug. 2015.

[165] J. A. Clark, A. Bauswein, N. Stergioulas, and D. Shoemaker, "Observing gravitational waves from the post-merger phase of binary neutron star coalescence," *Classical and Quantum Gravity*, vol. 33, p. 085003, Apr. 2016.

[166] R. De Pietri, A. Feo, J. A. Font, F. Löffler, F. Maione, M. Pasquali, and N. Stergioulas, "Convective Excitation of Inertial Modes in Binary Neutron Star Mergers," *Physical Review Letters*, vol. 120, p. 221101, June 2018.

[167] T. Dietrich, S. Bernuzzi, B. Brügmann, M. Ujevic, and W. Tichy, "Numerical relativity simulations of precessing binary neutron star mergers," Phys. Rev. D, vol. 97, p. 064002, Mar. 2018.

[168] L. Baiotti and L. Rezzolla, "Binary neutron star mergers: a review of Einstein's richest laboratory," *Reports on Progress in Physics*, vol. 80, p. 096901, Sept. 2017.

[169] S. Klimenko, G. Vedovato, M. Drago, F. Salemi, V. Tiwari, G. A. Prodi, C. Lazzaro, K. Ackley, S. Tiwari, C. F. Da Silva, and G. Mitselmakher, "Method for detection and reconstruction of gravitational wave transients with networks of advanced detectors," Phys. Rev. D, vol. 93, p. 042004, Feb. 2016.

[170] K. Chatziioannou, J. A. Clark, A. Bauswein, M. Millhouse, T. B. Littenberg, and N. Cornish, "Inferring the post-merger gravitational wave emission from binary neutron star coalescences," *Physical Review D*, vol. 96, p. 124035, Dec. 2017.

[171] LIGO Scientific Collaboration, "Advanced LIGO anticipated sensitivity curves," 2010. https://dcc.ligo.org/LIGO-T0900288/public, ZERO_DET_high_P.txt.

[172] T. Kawamura, B. Giacomazzo, W. Kastaun, R. Ciolfi, A. Endrizzi, L. Baiotti, and R. Perna, "Binary neutron star mergers and short gamma-ray bursts: Effects of magnetic field orientation, equation of state, and mass ratio," Phys. Rev. D, vol. 94, p. 064012, Sept. 2016.

[173] M. G. Alford, L. Bovard, M. Hanauske, L. Rezzolla, and K. Schwenzer, "Viscous Dissipation and Heat Conduction in Binary Neutron-Star Mergers," *Physical Review Letters*, vol. 120, p. 041101, Jan. 2018.

[174] T. Damour and A. Nagar, "Effective one body description of tidal effects in inspiralling compact binaries," Phys. Rev. D, vol. 81, p. 084016, Apr. 2010.

[175] T. A. Apostolatos, "Search templates for gravitational waves from precessing, inspiraling binaries," *Physical Review D*, vol. 52, pp. 605–620, July 1995.

[176] C. Messenger, K. Takami, S. Gossan, L. Rezzolla, and B. S. Sathyaprakash, "Source redshifts from gravitational-wave observations of binary neutron star mergers," *Physical Review X*, vol. 4, p. 041004, Oct. 2014.

[177] A. Bauswein, N.-U. F. Bastian, D. B. Blaschke, K. Chatziioannou, J. A. Clark, T. Fischer, and M. Oertel, "Identifying a first-order phase transition in neutron-star mergers through gravitational waves," *Physical Review Letters*, vol. 122, p. 061102, Feb. 2019.

[178] E. R. Most, L. J. Papenfort, V. Dexheimer, M. Hanauske, S. Schramm, H. Stöcker, and L. Rezzolla, "Signatures of quark-hadron phase transitions in general-relativistic neutron-star mergers," *Physical Review Letters*, vol. 122, p. 061101, Feb. 2019.

[179] T. W. Baumgarte, S. L. Shapiro, and M. Shibata, "On the maximum mass of differentially rotating neutron stars," *The Astrophysical Journal*, vol. 528, pp. L29–L32, Jan. 2000.

[180] T. Nakamura, "Relativistic cosmology. Proceedings.," in *Relativistic cosmology* (M. Sasaki, ed.), p. 155, Universal Academy Press, 1994.

[181] K. C. B. New and J. E. Tohline, "The relative stability against merger of close, compact binaries," *The Astrophysical Journal*, vol. 490, pp. 311–327, Nov. 1997.

[182] F. A. Rasio and S. L. Shapiro, "Coalescing binary neutron stars," *Classical and Quantum Gravity*, vol. 16, pp. R1–R29, June 1999.

[183] M. Shibata, K. Taniguchi, and K. Uryu, "Merger of binary neutron stars with realistic equations of state in full general relativity," *Physical Review D - Particles, Fields, Gravitation and Cosmology*, vol. 71, no. 8, pp. 1–26, 2005.

[184] R. Oechslin and H.-T. Janka, "Gravitational waves from relativistic neutron-star mergers with microphysical equations of state," *Physical Review Letters*, vol. 99, p. 121102, Sept. 2007.

[185] M. Shibata, K. Taniguchi, and K. Uryu, "Merger of binary neutron stars of unequal mass in full general relativity," *Physical Review D*, vol. 68, no. 8, p. 084020, 2003.

[186] K. Hotokezaka, K. Kyutoku, H. Okawa, M. Shibata, and K. Kiuchi, "Binary neutron star mergers: Dependence on the nuclear equation of state," *Physical Review D*, vol. 83, p. 124008, June 2011.

[187] LIGO Scientific Collaboration, "Prospects for observing and localizing gravitational-wave transients with Advanced LIGO, Advanced Virgo and KAGRA," 2016. https://dcc.ligo.org/LIGO-P1200087-v42/public, fig1_adv_sensitivity.txt.

[188] J. S. Speagle, "dynesty: a dynamic nested sampling package for estimating Bayesian posteriors and evidences," *arXiv e-prints*, Apr. 2019.

[189] H. Jeffreys, *Theory of probability*. Oxford, England: Oxford, third ed., 1961.

[190] D. Martynov, H. Miao, H. Yang, F. H. Vivanco, E. Thrane, R. Smith, P. Lasky, W. E. East, R. Adhikari, A. Bauswein, *et al.*, "Exploring the sensitivity of gravitational wave detectors to neutron star physics," *Physical Review D*, vol. 99, p. 102004, May 2019.

[191] N. J. Cornish and T. B. Littenberg, "Bayeswave: Bayesian inference for gravitational wave bursts and instrument glitches," *Classical and Quantum Gravity*, vol. 32, p. 135012, July 2015.

[192] T. B. Littenberg and N. J. Cornish, "Bayesian inference for spectral estimation of gravitational wave detector noise," *Physical Review D*, vol. 91, p. 084034, Apr. 2015.

[193] A. Torres-Rivas, K. Chatziioannou, A. Bauswein, and J. A. Clark, "Observing the postmerger signal of GW170817-like events with improved gravitational-wave detectors," *Physical Review D*, vol. 99, p. 044014, Feb. 2019.

[194] K. W. Tsang, T. Dietrich, and C. Van Den Broeck, "Modeling the postmerger gravitational wave signal and extracting binary properties from future binary neutron star detections," *Physical Review D*, vol. 100, p. 044047, Aug. 2019.

[195] T. Dietrich, S. Khan, R. Dudi, S. J. Kapadia, P. Kumar, A. Nagar, F. Ohme, F. Pannarale, A. Samajdar, S. Bernuzzi, *et al.*, "Matter imprints in waveform models for neutron star binaries: Tidal and self-spin effects," *Physical Review D*, vol. 99, no. 2, p. 24029, 2019.

[196] R. Pordes *et al.*, "The Open Science Grid," *J. Phys. Conf. Ser.*, vol. 78, p. 012057, 2007.

[197] I. Sfiligoi, D. C. Bradley, B. Holzman, P. Mhashilkar, S. Padhi, and F. Wurthwrin, "The pilot way to Grid resources using glideinWMS," *WRI World Congress*, vol. 2, pp. 428–432, 2009.

[198] T. Dietrich and K. Clough, "Cooling binary neutron star remnants via nucleon-nucleon-axion bremsstrahlung," *Physical Review D*, vol. 100, no. 8, p. 83005, 2019.

[199] B. Zhang, "The delay time of gravitational wave — gamma-ray burst associations," *Frontiers of Physics*, vol. 14, p. 64402, Dec. 2019.

[200] R. Ciolfi, "The key role of magnetic fields in binary neutron star mergers," *General Relativity and Gravitation*, vol. 52, p. 59, June 2020.

[201] N. Sarin and P. D. Lasky, "The evolution of binary neutron star post-merger remnants: a review," *General Relativity and Gravitation*, vol. 53, p. 59, June 2021.

[202] F. Douchin and P. Haensel, "A unified equation of state of dense matter and neutron star structure," *Astronomy & Astrophysics*, vol. 380, pp. 151–167, Nov. 2001.

[203] J. M. Lattimer and F. Douglas Swesty, "A generalized equation of state for hot, dense matter," *Nuclear Physics, Section A*, vol. 535, no. 2, pp. 331–376, 1991.

[204] B. P. Abbott, R. Abbott, T. D. Abbott, S. Abraham, F. Acernese, K. Ackley, C. Adams, V. B. Adya, C. Affeldt, M. Agathos, *et al.*, "Prospects for observing and localizing gravitational-wave transients with Advanced LIGO, Advanced Virgo and KAGRA," *Living Reviews in Relativity*, vol. 23, p. 3, Dec. 2020.

[205] LIGO Scientific Collaboration, "Unofficial sensitivity curves (ASD) for aLIGO, Kagra, Virgo, Voyager, Cosmic Explorer, and Einstein Telescope," 2020. https://dcc.ligo.org/LIGO-T1500293.

[206] S. Hild, S. Chelkowski, and A. Freise, "Pushing towards the ET sensitivity using 'conventional' technology," *arXiv*, Oct. 2008.

[207] S. Hild, M. Abernathy, F. Acernese, P. Amaro-Seoane, N. Andersson, K. Arun, F. Barone, B. Barr, M. Barsuglia, M. Beker, *et al.*, "Sensitivity studies for third-generation gravitational wave observatories," *Classical and Quantum Gravity*, vol. 28, p. 094013, May 2011.

[208] LIGO Scientific Collaboration, "Unofficial sensitivity curves (ASD) for aLIGO, Kagra, Virgo, Voyager, Cosmic Explorer, and Einstein Telescope," 2020. http://www.et-gw.eu/index.php/etsensitivities.

[209] B. P. Abbott, R. Abbott, T. D. Abbott, M. R. Abernathy, K. Ackley, C. Adams, P. Addesso, R. X. Adhikari, V. B. Adya, C. Affeldt, *et al.*, "Exploring the sensitivity of next generation gravitational wave detectors," *Classical and Quantum Gravity*, vol. 34, p. 44001, Feb. 2017.

[210] R. X. Adhikari, S. Ballmer, B. Barish, L. Barsotti, G. Billingsley, D. A. Brown, Y. Chen, D. Coyne, R. Eisenstein, M. Evans, *et al.*, "Cosmic Explorer: The U.S. Contribution to Gravitational-Wave Astronomy beyond LIGO," *Bulletin of the American Astronomical Society*, vol. 51, no. 7, 2019. https://baas.aas.org/pub/2020n7i035.

[211] T. Zhang, J. Smetana, Y. Chen, J. Bentley, D. Martynov, H. Miao, W. E. East, and H. Yang, "Toward observing neutron star collapse with gravitational wave detectors," *Physical Review D*, vol. 103, p. 044063, Feb. 2021.

[212] A. Bauswein, N. Stergioulas, and H.-T. Janka, "Revealing the high-density equation of state through binary neutron star mergers," *Physical Review D*, vol. 90, p. 023002, July 2014.

[213] E. Thrane, S. Kandhasamy, C. D. Ott, W. G. Anderson, N. L. Christensen, M. W. Coughlin, S. Dorsher, S. Giampanis, V. Mandic, A. Mytidis, T. Prestegard, P. Raffai, and B. Whiting, "Long gravitational-wave transients and associated detection strategies for a network of terrestrial interferometers," *Physical Review D*, vol. 83, p. 083004, Apr. 2011.

[214] A. J. Viterbi, "Error Bounds for Convolutional Codes and an Asymptotically Optimum Decoding Algorithm," *IEEE Transactions on Information Theory*, vol. 13, no. 2, pp. 260–269, 1967.

[215] S. Suvorova, L. Sun, A. Melatos, W. Moran, and R. J. Evans, "Hidden Markov model tracking of continuous gravitational waves from a neutron star with wandering spin," *Physical Review D*, vol. 93, p. 123009, June 2016.

[216] A. Miller, P. Astone, S. D'Antonio, S. Frasca, G. Intini, I. La Rosa, P. Leaci, S. Mastrogiovanni, F. Muciaccia, C. Palomba, O. J. Piccinni, A. Singhal, and B. F. Whiting, "Method to search for long duration gravitational wave transients from isolated neutron stars using the generalized frequency-Hough transform," *Physical Review D*, vol. 98, p. 102004, Nov. 2018.

[217] M. Oliver, D. Keitel, and A. M. Sintes, "Adaptive transient Hough method for long-duration gravitational wave transients," *Physical Review D*, vol. 99, p. 104067, May 2019.

[218] R. J. E. Smith, G. Ashton, A. Vajpeyi, and C. Talbot, "Massively parallel Bayesian inference for transient gravitational-wave astronomy," *Monthly Notices of the Royal Astronomical Society*, vol. 498, pp. 4492–4502, Sept. 2020.